Petroleum Science 23 (2026) 1105–1137

Contents lists available at ScienceDirect

Petroleum Science

journal homepage: www.keaipublishing.com/en/journals/petroleum-science

Original Paper

Sedimentary heterogeneity-constrained differential diagenesis in fluvial tight sandstones: Implications for reservoir quality heterogeneity in sandbody architectural elements

Pan-Ke Sun [a,b], Shi-Yi Jiang [c,d,*], Rui-Feng Yan [e], Li Liu [a,b], Gang Tian [a,b], Zeng Sheng [a,b], Bin Li [f], Rui-Feng Zhou [g], Si-Cheng Zhu [a,b], Lin Zhang [h]

[a] College of Geosciences, China University of Petroleum (Beijing), Beijing, 102249, China
[b] State Key laboratory of Petroleum Resources and Engineering, China University of Petroleum (Beijing), Beijing, 102249, China
[c] Institute of Unconventional Oil & Gas, Northeast Petroleum University, Daqing, 163318, Heilongjiang, China
[d] State Key Laboratory of Continental Shale Oil, Northeast Petroleum University, Daqing, 163318, Heilongjiang, China
[e] No.3 Gas Production Plant, CNPC Changqing Oilfield Company, Zhongning, 755100, Ningxia, China
[f] No.5 Oil Production Plant, CNPC Changqing Oilfield Company, Yulin, 718699, Shaanxi, China
[g] SINOPEC International Petroleum Exploration and Production Corporation, Beijing, 102249, China
[h] CNPC Western Drilling Engineering Co., Ltd., Wushenqi, 017300, Inner Mongolia, China

ARTICLE INFO

Article history:
Received 23 May 2025
Received in revised form
25 September 2025
Accepted 2 December 2025
Available online 8 December 2025

Edited by Xi Zhang and Jie Hao

Keywords:
Fluvial tight sandstone
Reservoir quality
Sedimentary heterogeneity
Diagenetic heterogeneity
Ordos Basin

ABSTRACT

Fluvial tight sandstones, as unconventional reservoirs, feature complex sedimentary, diagenetic, and reservoir quality heterogeneities that fundamentally control their exploration and development. This study focuses on typical fluvial tight sandstones of the Shanxi Formation in northern Sulige Gas Field (Ordos Basin), using core samples, field sections, logging data, and analytical tests to investigate the coupling relationships among sedimentary, diagenetic, and reservoir quality heterogeneities. Results demonstrate that: the target layer in the study area develops six lithofacies, three braided river sandbody architectural elements, two meandering river sandbody architectural elements, and five diagenetic facies. Different architectural elements and their internal lithofacies exhibit differences and coupling relationships in the strengths of sedimentary heterogeneity and diagenetic heterogeneity. Specifically: strong compaction diagenetic facies primarily occurs in siltstone lithofacies of sand-dominated, weakly sedimentary heterogeneous architectural elements; strong dissolution + microfracture development diagenetic facies is mainly distributed in coarser-grained sandstones of sand-dominated architectural elements with low sedimentary heterogeneity; clay mineral intercrystalline pore-dominated diagenetic facies is primarily located near interbeds within all architectural elements; strong carbonate cementation diagenetic facies predominates in thick mudstones at the top/bottom of architectural elements, and at contacts with pure mudstone interbeds; strong clay mineral cementation diagenetic facies concentrates in medium-heterogeneity architectural elements near pure mudstone interbeds and at contacts with silty mudstone interbeds. Sedimentary and diagenetic heterogeneities jointly control reservoir quality distribution in all architectural elements (excluding basal conglomerates): porosity and permeability decrease in positive rhythm as lithofacies grain size fines, while irreducible water saturation increases in inverse rhythm. The findings of this study can provide a robust basis for the exploration and development deployment of fluvial tight sandstone reservoirs.

1. Introduction

Fluvial tight sandstones are a very important type of unconventional oil and gas reservoir. Currently, in China, the Shanxi Formation in the northern Ordos Basin, in the United States, the Mesaverde and Lance formations of the Pinedale Anticline in the

* Corresponding author.
E-mail address: shiyi.jiang21zn@nepu.edu.cn (S.-Y. Jiang).
Peer review under the responsibility of China University of Petroleum (Beijing).

https://doi.org/10.1016/j.petsci.2025.12.003

Greater Green River Basin of Wyoming, in Libya, the Nubian Formation in the southeastern part of the Sirte Basin, and Australia, the Willespie Formation of the Perth Basin, etc. In these basins with huge reserves of unconventional oil and gas resources, the main oil and gas producing layers are all of fluvial facies sedimentation (Kadkhodaie-Ilkhchi et al., 2019; Leila et al., 2024; Marghani et al., 2023; Sahoo et al., 2016).

The degree of reservoir heterogeneity plays a fundamental role in the subsurface exploration and development of oil and gas resources (Ahmadi et al., 2025). Fluvial tight sandstone reservoirs are among the reservoirs with the most complex heterogeneity. The heterogeneity of sediment structure (grain size, sorting, and rounding), sedimentary structures (bedding), and sandbody architecture (lithofacies and their combinations) in these reservoirs determines the heterogeneity of the original reservoir quality (original porosity) (El-Gendy et al., 2022; Ocheli et al., 2025). Additionally, as the material basis for diagenesis, the heterogeneity of the original sediments also gives rise to the heterogeneity of diagenesis within fluvial sandbodies. This, in turn, leads to the heterogeneity of reservoir evolution of the lithofacies within the sandbodies, and ultimately results in the heterogeneity of reservoir quality (physical properties and fluid mobility) within the sandbodies (Antonellini et al., 2025). The heterogeneities of these sedimentation and diagenesis determine the differences in the reservoir quality within the sandbodies and the enrichment of oil and gas, severely restricting the actual development and exploitation effects of oil and gas fields. Exploring the differential diagenetic patterns under the constraints of sedimentary heterogeneities of fluvial tight sandstones is of great significance for understanding the reservoir quality heterogeneities of sandbody architectural elements, and thus for guiding the actual development of oil and gas fields.

Current research on high-quality fluvial tight sandstone reservoirs primarily focuses on single-factor controls (e.g., sedimentation, diagenesis) (Busch et al., 2024; Fallah-Bagtash et al., 2025; Shi et al., 2024) or sandstone-mudstone spatial relationships (Shang et al., 2019; Xie et al., 2024). While this provides basic insights into reservoir heterogeneity, critical gaps remain: insufficient exploration of sedimentary-diagenetic coupling at the sandbody architecture scale, lack of systematic research on the control over reservoir quality, and unclear heterogeneous patterns across different architectural elements.

To address these gaps, this study, based on the summarized understanding of how single factors (sedimentation, diagenesis) and sandstone-mudstone spatial relationships control high-quality reservoirs, proposes the hypothesis that sedimentary and diagenetic heterogeneity—incorporating both single factors and sandstone-mudstone spatial relationships—exerts a more significant control on high-quality reservoirs.

Furthermore, targeting the Shanxi Formation in the northern Ordos Basin, this study focuses on two key aspects: characterizing the sandstone-mudstone spatial relationships of fluvial tight sandstone reservoirs using sedimentary and diagenetic heterogeneity, and exploring the coupling relationships, genetic patterns, and distribution patterns of sedimentary-diagenetic-reservoir quality heterogeneity. The results demonstrate that, for fluvial tight sandstone reservoirs, sedimentary heterogeneity clearly constrains diagenetic heterogeneity; moreover, reservoir quality heterogeneity within sandbody architectural elements and the distribution of high-quality reservoirs are significantly regulated by the influence of sedimentary heterogeneity on diagenetic heterogeneity. Ultimately, this study yields a deeper and more systematic understanding of the coupling relationships among sedimentary-diagenetic-reservoir quality heterogeneity, as well as the genetic mechanisms and patterns of high-quality fluvial tight sandstone reservoirs.

2. Regional geological background

2.1. The tectonic location of the study area

The Ordos Basin is a typical Paleozoic cratonic basin located in central China, which is rich in oil and gas resources (Jiang et al., 2023). The Ordos Basin is composed of six hierarchical tectonic units (Qin et al., 2024): the Yimeng Uplift, Yishan Slope, Tianhuan Depression, Western Thrust Belt, Jinxi Fault-Fold Belt, and Weibei Uplift. The study area is located on the transitional zone between the Yimeng Uplift and the Yishan Slope in the northern part of the Ordos Basin (Fig. 1).

2.2. Stratigraphic and sedimentary evolution processes

The Shanxi Formation is the main gas-bearing horizon in the study area, and it is a typical coal measure stratum of fluvial facies sedimentation (Jiang et al., 2024; Li et al., 2019). According to the characteristics of sequence stratigraphy, the Shan 1 Member (P_1s_1) of the Shanxi Formation is further divided into three layers, namely Shan 11 ($P_1s_1^1$), Shan 12 ($P_1s_1^2$), and Shan 13 ($P_1s_1^3$). The Shan 2 Member (P_1s_2) is further divided into three layers, Shan 21 ($P_1s_2^1$), Shan 22 ($P_1s_2^2$), and Shan 23 ($P_1s_2^3$). Five layers, namely Shan 11, Shan 12, Shan 13, Shan 21, and Shan 22, are of meandering river sedimentation, and Shan 23 is of braided river sedimentation (Fig. 2).

3. Data and methods

3.1. Data situation

This study compiled core data and imaging data of the Shanxi Formation from 63 cored wells in the northern Sulige Gas Field, with part directly provided by CNPC Western Drilling Engineering Co., Ltd. and the remainder derived from experiments on collected core samples. The dataset encompasses core photos, logging curves, field outcrop photos, porosity (Φ), permeability (K), irreducible water saturation measured by nuclear magnetic resonance (S_{nbw}), grain size analysis (P_{25}/P_{75}), pore structure analysis, clastic compositions, X-ray diffraction (XRD) results, comprehensive casting thin sections (CTS), and scanning electron microscopy (SEM) images, with details shown in Table 1.

3.2. Methods for characterizing sedimentary heterogeneity

Lithofacies is the basic unit for characterizing the composition of sedimentary materials and sedimentary structures under different hydrodynamic conditions (Colombera and Mountney, 2019; Miall, 1985). Therefore, the internal sedimentary heterogeneity of a single sandbody architectural element is reflected in the differences of lithofacies and their combinations. In this study, two parameters, “lithofacies density” and “lithofacies frequency”, were established for a single sandbody to characterize the internal sedimentary heterogeneity of sandbody architectural elements.

3.2.1. Lithofacies density

The “lithofacies density (D_L)” is defined as the ratio of the thickness of a single lithofacies (T_L) to the thickness of the architectural element (T_{LC}). Here, the thickness of the architectural element refers to the total vertical thickness of the architectural elements within the sandbody architectural element, and the

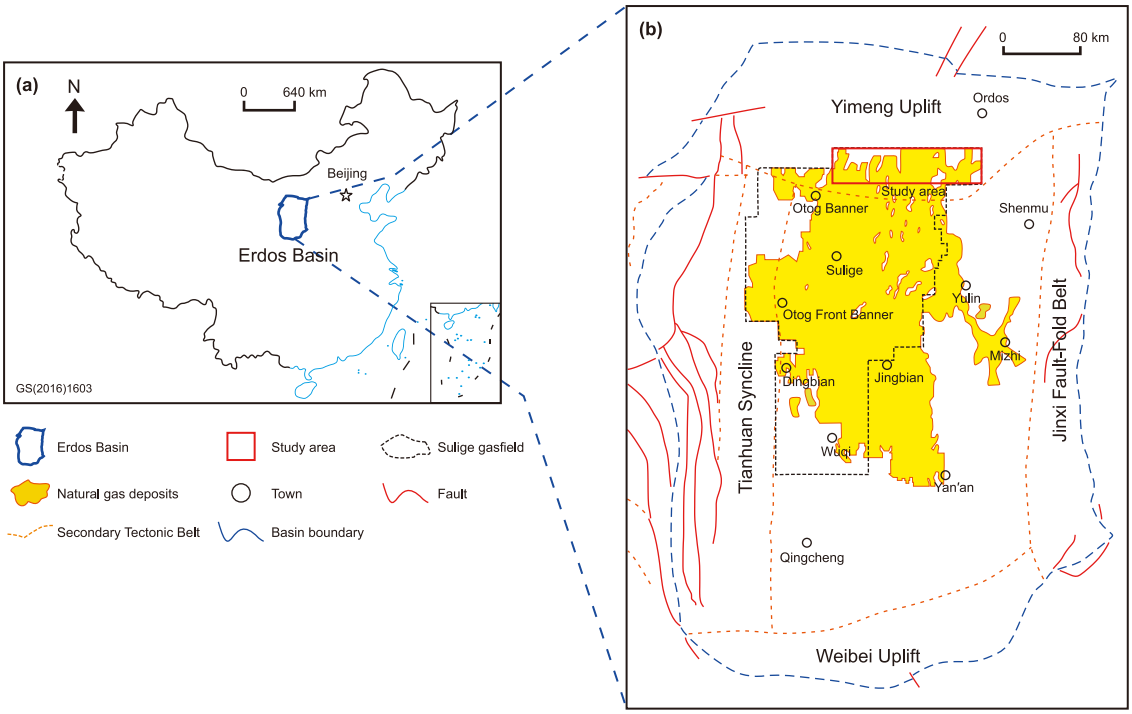

Fig. 1. Location of the study area (modified from Jiang et al., 2024). **(a)** Location of the Erdos Basin. **(b)** Location of the study area in the Erdos Basin.

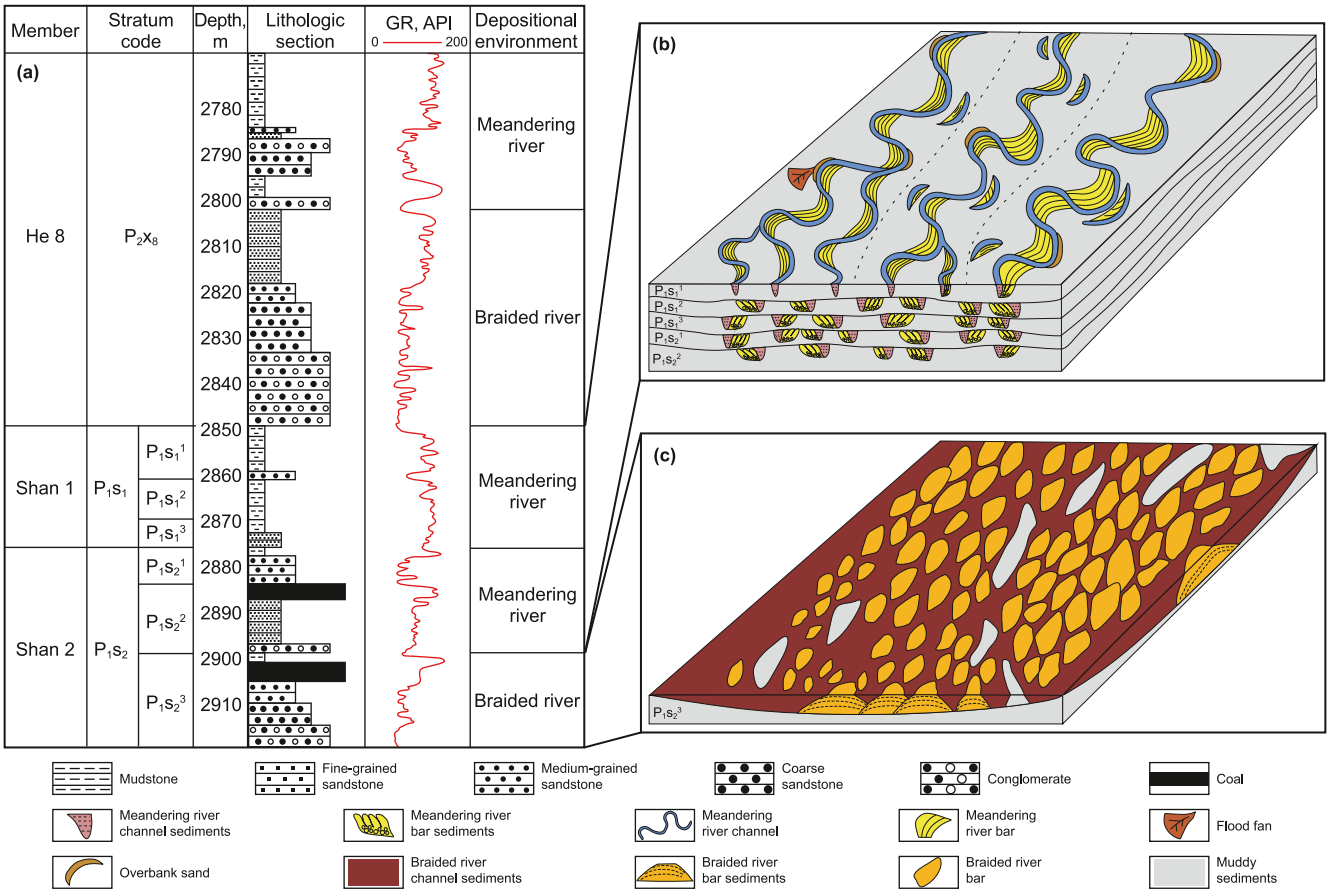

Fig. 2. The stratum, sedimentary patterns, and evolution of the study area (modified from Jiang et al., 2024). **(a)** The lithologic sedimentary sequence and sedimentary environment of He 8, Shan 1, and Shan 2 in the study area. **(b)** The sedimentary evolution patterns of the meandering river from $P_1s_2^2$ to $P_1s_1^1$. **(c)** The braided river sedimentary pattern of $P_1s_2^3$.

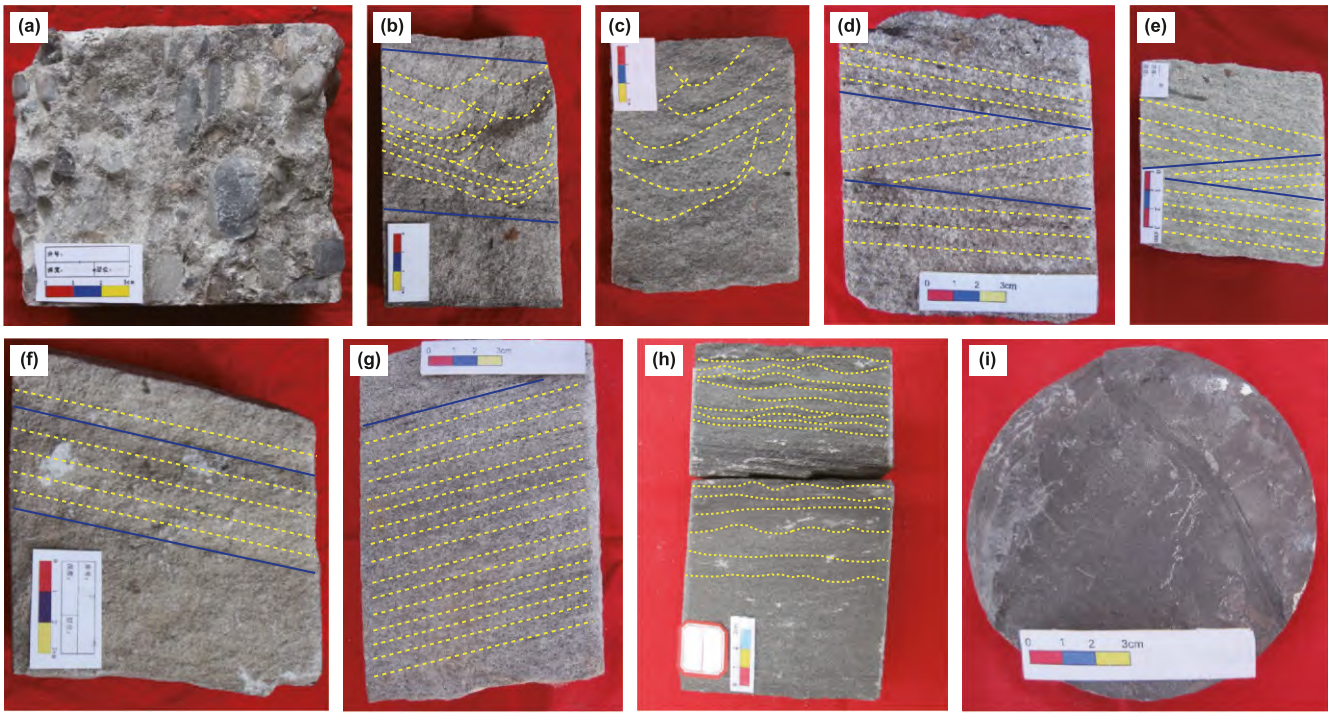

Fig. 3. Some photos of the core. The yellow lines in **(b)** and **(c)** mark the trough cross-bedding. The yellow lines in **(d)** and **(e)** mark the plate cross-bedding. The yellow lines in **(f)** and **(g)** mark the parallel bedding. The yellow line in **(h)** marks the wavy bedding.

Table 1
Types and quantities of data collected in this study.

Data	Number
Porosity (Φ)	1590
Permeability (K)	1544
Nuclear magnetic resonance (S_{nbw})	637
Grain size analysis (P_{25}/P_{75})	138
Pore structure analysis	138
Clastic compositions	138
X-ray diffraction (XRD)	112
Comprehensive casting thin sections (CTS)	282
Scanning electron microscopy (SEM)	316

thickness of a single lithofacies refers to the individual thickness of a certain lithofacies within this architectural element. The calculation formula is as follows:

$$D_L = \frac{T_L}{T_{LC}} \tag{1}$$

The total lithofacies density (D_{TL}) of a certain lithofacies in the architectural element is the ratio of the total thickness (T_{TL}) of a certain lithofacies to T_{LC}, and the formula is as follows:

$$D_{TL} = \frac{T_{TL}}{T_{LC}} \tag{2}$$

3.2.2. Lithofacies frequency

The "lithofacies frequency (LF)" is defined as the ratio of the number of a certain lithofacies (N_{TL}) in the sandbody architectural element to the total number of lithofacies (N_{LC}) in the architectural element. The calculation formula is as follows:

$$LF = \frac{N_{TL}}{N_{LC}} \tag{3}$$

3.3. Methods for characterizing the diagenetic strength

3.3.1. Original porosity

According to the data provided by the grain size analysis, this study adopted the initial porosity (Φ_o) equation established by Scherer (Eq. (5)) (Beard and Weyl, 1973; Scherer, 1987). The Trask sorting coefficient (S_0) was calculated according to the widely used formula by Folk and Ward (Eq. (4)) (Folk and Ward, 1957).

$$S_0 = \frac{P_{25}}{P_{75}} \tag{4}$$

$$\Phi_o = 20.91 + \frac{22.9}{S_0} \tag{5}$$

Among them, P_{25} and P_{75} are respectively the particle sizes (mm) corresponding to 25% and 75% of the cumulative probability curve of the grain size; "20.91″ and "22.9″ are the intercept and coefficient of the regression formula Eq. (5) obtained by (Scherer, 1987) through analyzing the research data of (Beard and Weyl, 1973), which are widely used in the calculation of original porosity of sandstone reservoirs.

3.3.2. Diagenetic strength

Calculating the increase and decrease of reservoir porosity caused by diagenesis can quantitatively characterize the diagenetic strength (Wendao et al., 2019). According to the types and effects of diagenesis, it can be divided into porosity reduction due to compaction, porosity reduction due to cementation (including porosity reduction due to carbonate cementation and porosity reduction due to clay mineral cementation), porosity increase due to dissolved pores caused by dissolution, porosity increase due to microfractures caused by fracturing, and porosity increase due to intercrystalline pores of clay minerals. Based on the diagenetic

background of the Shanxi Formation in the study area, Table 2 lists the formulas for calculating the diagenetic strength (Wang et al., 2023).

V_g is the grain volume; V_t is the apparent molar volume of present-day rock; V_{cc} is the volume of carbonate cement; V_{cmc} is the volume of clay mineral cement; V_{dp} is the volume of dissolved pores at present; V_{mf} is the volume of microfractures at present; V_{icp} is the volume of intercrystalline pores of clay minerals at present.

4. Results

4.1. Lithofacies

According to the results of core description, classification is carried out based on grain size and main sedimentary structures, and modifications are made following the lithofacies classification by scholars such as Miall (1985) and Colombera (Colombera and Mountney, 2019). Table 3 summarizes the petrology, sedimentary structures (bedding), sedimentary textures (sorting and rounding) and genetic interpretations of various lithofacies.

4.2. Sandbody architectural elements

4.2.1. Braided river sandbody architectural elements

Based on the sediment grain size, sedimentary structures, geometric shapes, paleocurrent directions, sediment occurrence locations, as well as the lateral and vertical arrangements of lithofacies, three sandbody architectural elements in the sandstone of the braided river sedimentary reservoir in the study area have been determined. Fig. 4 shows the characteristics of the architectural elements of the core or head (BBt1), flanks (BBt2), and tail (BBt3) of the channel bars deposited by the braided river flow in five periods, which is the most complete in the study area. By dissecting the field outcrops of the braided river channel bar sandbodies in the Shanxi Formation of the study area (Fig. 4(d)), it can be known that the water flows of the I–III periods are mainly characterized by vertical aggradation (Fig. 4(b)). The thickness of the deposited sandstone gradually decreases, and the interlayers of silty mudstone begin to develop in the III period (Fig. 4(b)). The water flows of the IV–V periods are mainly characterized by lateral aggradation (Fig. 4(b)) and downstream aggradation (Fig. 4(c)). The thickness of the deposited sandstone gradually decreases, and the interlayers of silty mudstone gradually thicken (Fig. 4(b) and (c)). Table 4 shows the cyclic, sedimentary and lithofacies characteristics of different architectural elements and their genesis.

4.2.2. Meandering river sandbody architectural elements

According to the sediment grain size, sedimentary structures, geometric shapes, paleocurrent directions, the occurrence locations of sediments, as well as the lateral and vertical arrangements of lithofacies, two architectural elements of sandbodies in the sandstone reservoirs of meandering river deposits in the study area have been determined. Fig. 5 illustrates the characteristics of the architectural elements of the point bar (MB) and the final-stage river channel (MFCH) under the sedimentation of meandering river water flow in five periods, which is the most complete in the study area. The thickness of the laterally aggraded sandstone deposits in the I to V periods gradually decreases, and the interlayers of pure mudstone gradually thicken. Table 5 shows the cyclic, sedimentary and lithofacies characteristics of different architectural elements and their genesis.

4.3. Diagenesis

4.3.1. Compaction

Compaction is caused by the static pressure of the rock, which leads to the re-arrangement of mineral particles and changes in their contact geometry, and it is the main cause of the loss of primary inter-particle pores (He et al., 2002). In the study area, the sandstones of the Shanxi Formation are generally strongly compacted. Differences in structural maturity and compositional maturity result in different compaction characteristics of the sandstones in the Shanxi Formation. Sandstone samples with poor sorting, low roundness, and a high content of rock fragments usually show linear contacts or dense accumulations (Fig. 6(a)). Ductile particles, such as mica, volcanic materials, and argillaceous fragments, are deformed under the effect of compaction (Fig. 6(b)),

Table 2
Types, parameters, and calculation formulas of diagenetic intensity.

Diagenesis	Parameter	Equation	Equation number
Compaction	Intergranular volume (Φ_{IGV})	$\Phi_{IGV} = 1 - \frac{V_g}{V_t}$	(6)
	Porosity reduced due to compaction (Φ_{CR})	$\Phi_{CR} = (\Phi_O - \Phi_{IGV}) \times \frac{(1-\Phi_O)}{(1-\Phi_{IGV})}$	(7)
Carbonate minerals cementation	Carbonate mineral cement content (Φ_{CC})	$\Phi_{CC} = \frac{V_{cc}}{V_t}$	(8)
	Porosity reduction due to cementation of carbonate minerals (Φ_{CCR})	$\Phi_{CCR} = (\Phi_O - \Phi_{CR}) \times \frac{\Phi_{CC}}{\Phi_{IGV}}$	(9)
Clay minerals cementation	Clay mineral cement content (Φ_{CMC})	$\Phi_{CMC} = \frac{V_{cmc}}{V_t}$	(10)
	Porosity reduction due to cementation of clay minerals (Φ_{CMCR})	$\Phi_{CMCR} = (\Phi_O - \Phi_{CR}) \times \frac{\Phi_{CMC}}{\Phi_{IGV}}$	(11)
Dissolution	Dissolution pores content (Φ_{DP})	$\Phi_{DP} = \frac{V_{dp} + V_{cc} + V_{cmc}}{V_t}$	(12)
	Porosity increases due to dissolution (Φ_{DPI})	$\Phi_{DPI} = \Phi_{DP} \times (1 - \Phi_{CR})$	(13)
Fracturing	Microfracture content (Φ_{MF})	$\Phi_{MF} = \frac{V_{mf}}{V_t}$	(14)
	Porosity increased by microfractures due to fracturing (Φ_{MFI})	$\Phi_{MFI} = \Phi_{MF} \times (1 - \Phi_{CR})$	(15)
Intercrystalline pores of clay minerals	Intercrystalline pores content (Φ_{ICP})	$\Phi_{ICP} = \frac{V_{icp}}{V_t}$	(16)
	Porosity increases due to intercrystalline pores of clay minerals (Φ_{ICPI})	$\Phi_{ICPI} = \Phi_{ICP} \times (1 - \Phi_{CR})$	(17)

Table 3
Lithofacies types and their lithology, sedimentary texture, sedimentary structure and geological genetic interpretation of Shanxi Formation in the study area.

Lithofacies/code	Lithology	Bedding	Sorting	Roundness	Genetic interpretation
Massive bedding conglomerate/Gm	Gray–white conglomerate (Fig. 3(a))	Massive bedding (Fig. 3(a))	Poor	Angular and Subangular	Products of rapid deposition and high-energy hydrodynamic conditions with poor sorting in fluvial beds
Trough cross–bedding sandstone /Stc	Grayish–white coarse sandstone (Fig. 3(b)) and Grayish–white medium sandstone (Fig. 3(c))	Trough cross-bedding (Fig. 3(b), Fig. 3(c))	Medium or better	Subangular and subrounded	Products of a depositional environment under high-energy hydrodynamic conditions with frequent flow direction changes
Plate cross–bedding sandstone/Spc	Grayish–white coarse sandstone (Fig. 3(d)) and Grayish–white medium sandstone (Fig. 3(e))	Plate cross-bedding (Fig. 3(d), Fig. 3(e))	Medium or better	Subangular and Subrounded	Products of sediment lateral accretion or progradation under high-energy hydrodynamic conditions
Parallel bedding sandstone/ Sp	Grayish–white medium sandstone (Fig. 3(f)) and Grayish–white fine sandstone (Fig. 3(g))	Parallel bedding (Fig. 3(f), Fig. 3(g))	Medium or poor	Subangular and Subrounded	Products of a depositional environment under gradational hydrodynamic conditions with stable and persistent sedimentation
Ripple bedding sandstone/ Sr	Grayish–black siltstone (Fig. 3(h)) and Gray fine sandstone	Ripple bedding (Fig. 3(h))	Well	Well-rounded	Products of a depositional environment under low-energy hydrodynamic conditions with low-intensity flow regime and limited sediment supply
Massive bedding mudstone/Mm	Grayish–black mudstone and Grayish–black silty mudstone (Fig. 3(i))	Massive bedding (Fig. 3(i))			Products of a depositional environment under low-energy hydrodynamic conditions and prone to fluvial erosion

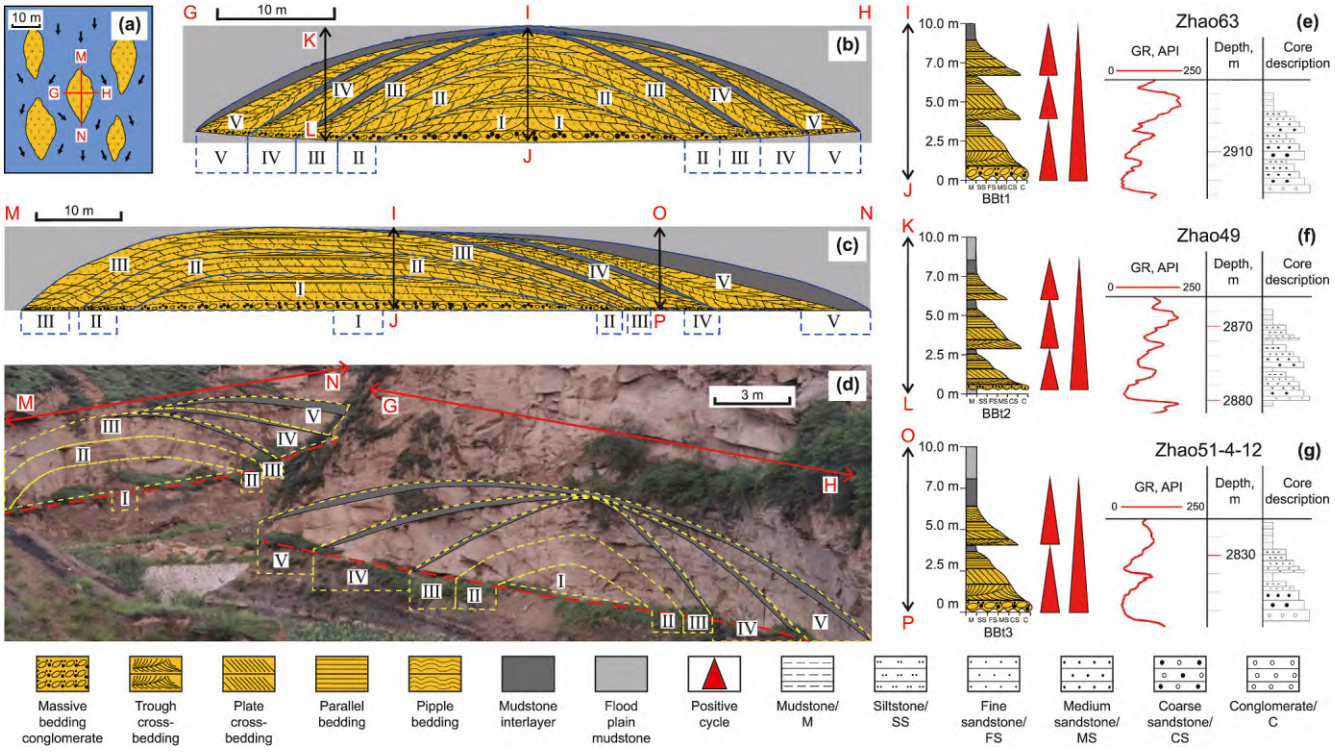

Fig. 4. Plan and cross-sectional views of braided river channel sandbody architecture. **(a)** Planar schematic diagram of braided river deposition. **(b)** Cross-source bar profile. **(c)** Along-source bar profiled. **(d)** Outcrop photograph. **(e)** BBt1. **(f)** BBt2. **(g)** BBt3.

and concave-convex contacts often occur between ductile particles and rigid particles. In sandstones with good sorting, high roundness, and a high content of rigid particles (such as quartz), point contacts frequently appear between the rigid particles (Fig. 6(c)), and a small number of microfractures also manifest (Li et al., 2020).

4.3.2. *Fracturing*

The fracturing is generally caused by tectonic movements (Qin et al., 2022), and it mainly occurs in sandstone samples with large clasts and a high content of rigid particles (such as quartz). These large-sized rigid clastic particles are usually well-developed with microfractures (Fig. 6(c)).

Table 4
Cyclic, sedimentary and lithofacies characteristics of different architectural elements in braided river sandbodies and their genesis.

Type	Characteristics			Genetic analysis
	Cyclic	Sedimentary	Lithofacies	
Type-1 braided river bar/BBt1	A single long-term positive cycle with three short-term positive cycles; sandstone thickness decreases systematically from base to top of short-term cycles.	Characterized by vertical aggradation and stacking of multi-phase braided-river sediments; vertical lithofacies stacking of three-phase flow sediments at braided bar core/head (Fig. 4(b), (c), I–J; Fig. 4(e))	Trough/plate cross-bedded facies proportion decreases upward, parallel/ripple–bedded facies increases; no silty mudstone interlayers. Massive-bedded conglomerate restricted to lower short–term cycle; massive-bedded mudstone forms at upper cycle top.	Reflects weakening hydrodynamics (sediment fining, flow stabilizing); each cycle records declining energy (thinning trough/plate, thickening parallel/ripple-bedded facies). No silty mudstone interlayers due to dominant vertical aggradation at bar core/head–strong deposition hydrodynamics fully eroded pre-existing mudstone, preventing preservation.
Type-2 braided river bar/BBt2	A single long-period positive cycle with three short-period cycles. Sandstone thickness decreases progressively from middle to bottom to top cycles.	Characterized by lateral aggradation and superposition of multi-period braided-river sediments; vertical lithofacies stacking of three-phase flow sediments on braided bar flanks (Fig. 4(f); Fig. 4(b), K–L).	Trough/plate cross-bedded facies proportion decreases upward; parallel/ripple-bedded facies and silty mudstone increase. Massive conglomerate restricted to lower cycle; thin floodplain mudstone at base.	Reflects weakening hydrodynamics (strong→weak), with sediment coarsening upward and flow stabilizing. Silty mudstone thickening reflects reduced erosive capacity. Basal thin mudstone is residual from incomplete floodplain erosion.
Type-3 braided river bar/BBt3	A single long-period positive cycle containing two short–period positive cycles; lower short–period cycle has thicker sandstone than upper.	Characterized by downstream aggradation and superposition of multi-period braided-river sediments; vertical lithofacies stacking of two-phase flow sediments at braided bar tail (Fig. 4(c), O–P; Fig. 4(g)).	Lithofacies thickness proportion variation analogous to BBt2; massive-bedded conglomerate in lower short–period cycle is thicker.	Reflects weakening hydrodynamics (culminating in static water), with sediment fining upward and flow direction stabilizing. Lower cycle reflects strong-to-weak energy decline; upper cycle transitions to static water. Top thick mudstone is floodplain deposit.

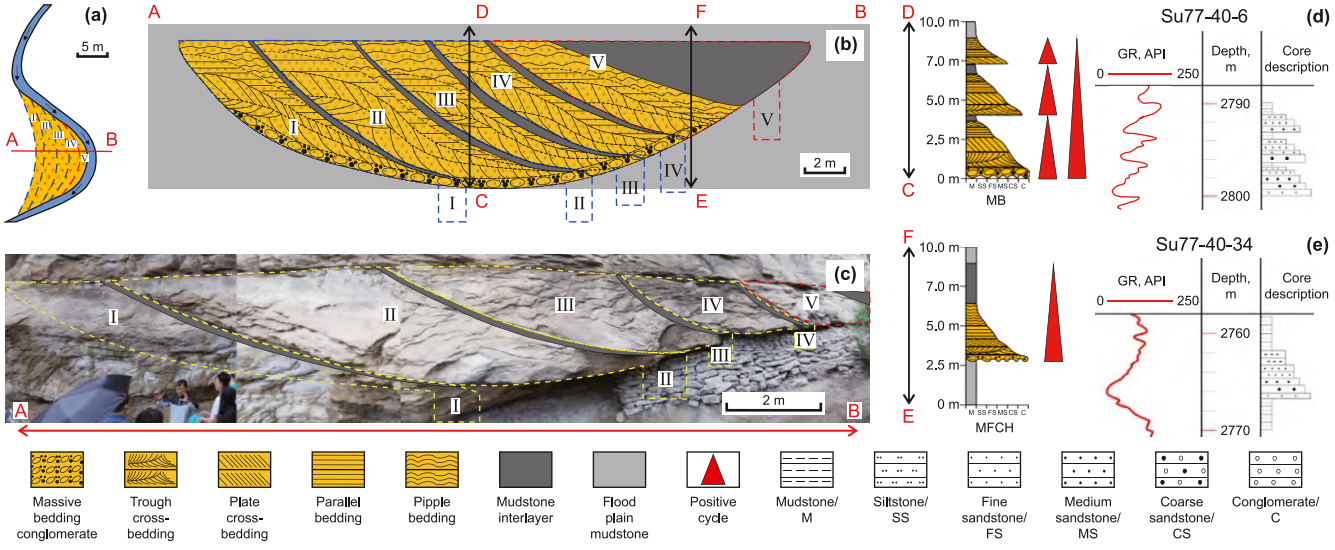

Fig. 5. Plan and cross-sectional views of meandering river sedimentary sandbody architecture. **(a)** Planar schematic diagram of meandering river deposition. **(b)** Cross-source profile of meandering river sedimentary sandbody architecture. **(c)** Outcrop photograph. **(d)** MB. **(e)** MFCH.

4.3.3. Cementation

The sandstones of the Shanxi Formation are developed with carbonate cementation and clay mineral cementation, with clay mineral cementation being the dominant type.

The carbonate cements include calcite and dolomite, with calcite being the main component. Calcite is usually present in the dissolved pores (Fig. 7(a)). Carbonate cementation is one of the causes of pore loss (Janssen et al., 2023).

The clay mineral cements include kaolinite, illite, and mixed illite/smectite, with kaolinite and illite being the dominant ones. Kaolinite appears in the forms of “vermicular” and “booklet-shaped” (Fig. 7(b) and (c)). Illite appears in sheet-like and fibrous forms (Fig. 7(d) and (e)), and the mixed illite/smectite appears in a

Table 5
Cyclic, sedimentary and lithofacies characteristics of different architectural elements in meandering river sandbodies and their genesis.

Type	Characteristics			Genetic analysis
	Cyclic	Sedimentary	Lithofacies	
Point bar/MB	A single long-period positive cycle incorporating three short-period positive cycles; sandstone thickness in short-period cycles decreases progressively from bottom to top.	Characterized by lateral aggradation and superposition of multi-phase meandering river sediments; vertical lithofacies stacking of three-phase flow sediments in meandering river point bar (Fig. 5(b), D–C; Fig. 5(d)).	Trough/plate cross-bedded sandstone facies proportion decreases upward, while parallel/ripple-bedded sandstone facies and pure mudstone proportions increase. Massive-bedded conglomerate is exclusively developed in the lower short-period cycle.	Reflects gradual weakening of initial strong hydrodynamics (grain size fining, flow stabilizing from variable to unidirectional). Each cycle records strong-to-weak transition (thinning trough/plate, thickening parallel/ripple-bedded facies and pure mudstone). Pure mudstone interlayers thicken due to reduced erosive capacity, preserving more pre-existing mudstone—indicating changing depositional environments.
Final-stage river channel/MFCH	A single positive cycle.	Formed by lateral aggradation of sediments from meandering river final-stage channel; vertical lithofacies stacking relationship of final-stage channel (Fig. 5(b), F–E; Fig. 5(e)).	Thin-layered massive bedding conglomerate developed at MFCH bottom. Trough/plate cross-bedding sandstone facies proportion small in middle and lower parts; parallel/ripple bedding sandstone facies proportion relatively large in middle and upper parts; thick mudstone proportion largest at top/bottom.	Reflects relatively weak hydrodynamic force gradually weakening to static water environment (grain size fining, flow direction transitioning from frequent changes to single and stable). Bottom thick mudstone represents floodplain deposition; middle sandstone reflects hydrodynamic force changing from strong to weak (flow stabilizing) and weak environment deposition; top thick mudstone represents final-stage channel static water sediments (hydrodynamic force weakening to static water deposition stage).

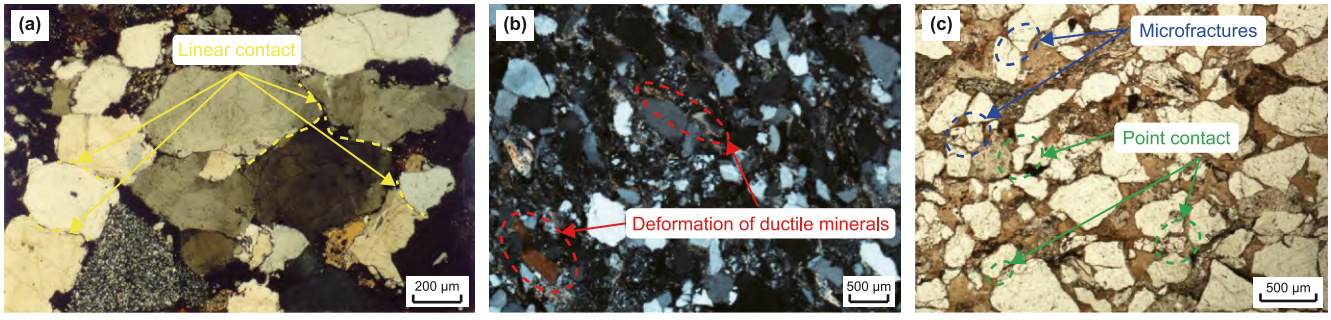

Fig. 6. The optical microscope photograph of the compaction. **(a)** Linear contact or dense accumulation of minerals. **(b)** Deformation of ductile minerals and concave-convex contact. **(c)** Point contact and microfractures.

"honeycomb-shaped" form (Fig. 7(f)). Most of them are present in primary pores and dissolved pores. The "vermicular" cementation of kaolinite, the sheet-like cementation of illite, and the fibrous cementation of illite are one of the main causes of pore loss, while the "booklet-shaped" kaolinite and the "honeycomb-shaped" mixed illite/smectite are one of the main causes for the formation of intercrystalline pores (Haile et al., 2015; Jiu et al., 2021).

4.3.4. Dissolution

The dissolution is manifested in two forms: intergranular dissolution and intragranular dissolution. The dissolution is the cause of the development of dissolved pores, which improves the physical properties of the reservoir (Zhu et al., 2024). The Shanxi Formation in the study area is coal measure strata, and the sandstone in it undergoes strong dissolution. After the dissolution of the particles, three forms are presented. Some intergranular spaces are filled with cements after dissolution (Fig. 8(a)). Some intergranular and intragranular areas form pores after dissolution (Fig. 8(b) and (c)). For some other particles, they are completely dissolved, and moldic pores are formed, leaving only the contours of the granules (Fig. 8(d)).

4.3.5. Metasomatism

Metasomatism is a process in which one mineral is replaced by another (Rubinstein et al., 2013). Metasomatism in the sandstones of the Shanxi Formation in the study area is relatively rare,

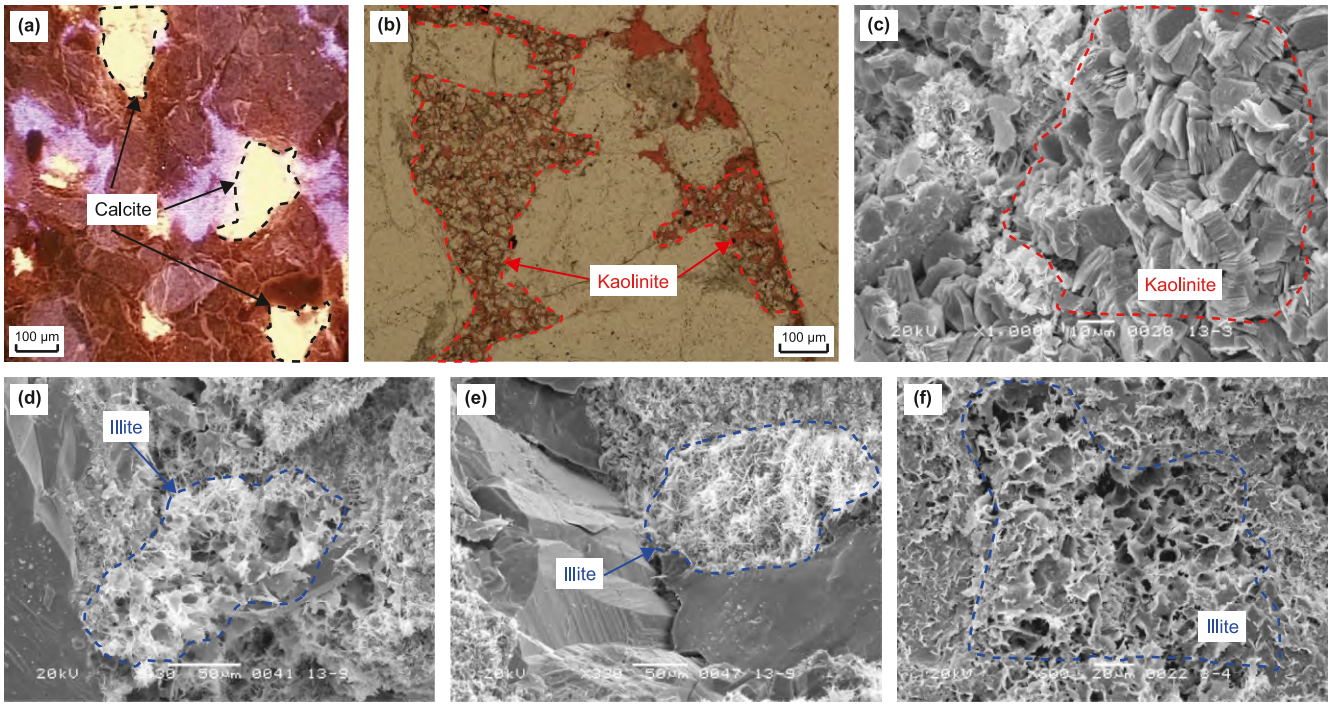

Fig. 7. Cathodoluminescence, optical microscope and scanning electron microscope photographs of the cementation process. **(a)** Cathodoluminescence of calcite. **(b)** Vermicular kaolinite fills the pores. **(c)** Booklet-shaped kaolinite. **(d)** Sheet-like illite. **(e)** Fibrous illite. **(f)** Honeycomb-shaped illite.

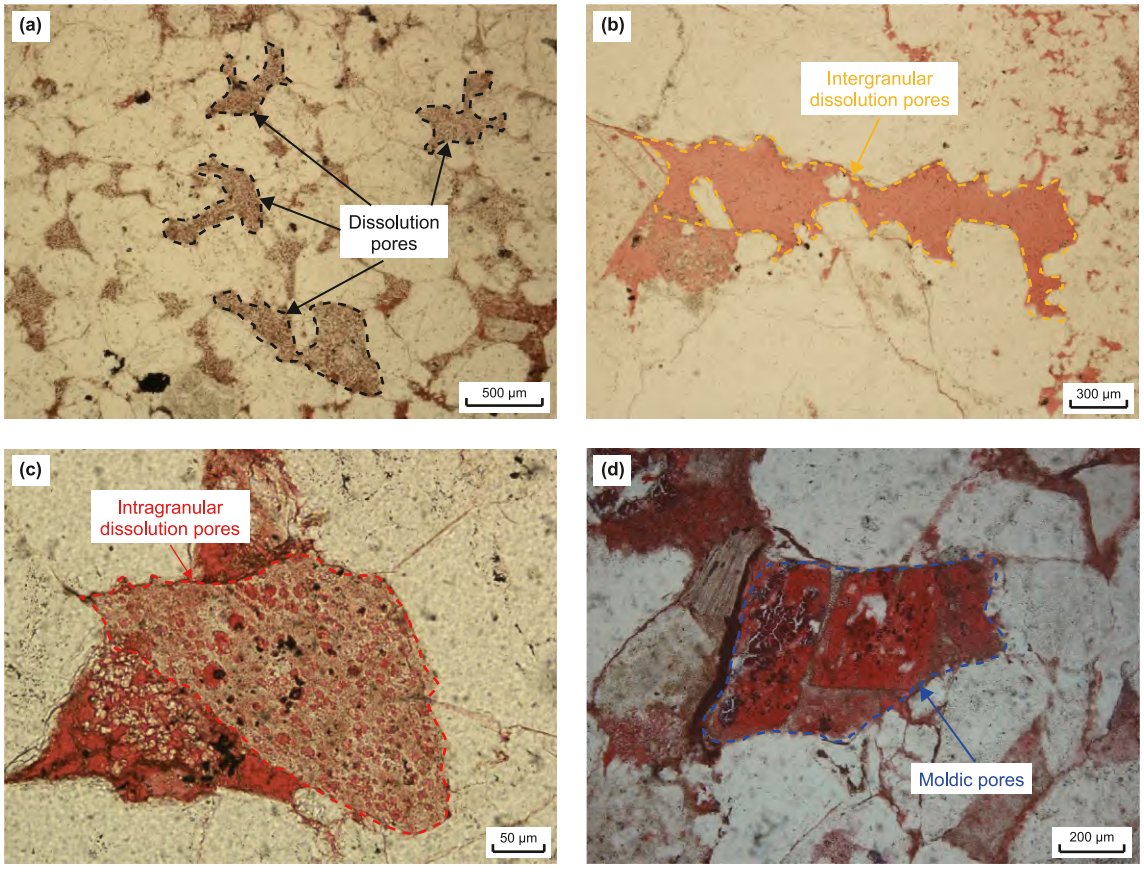

Fig. 8. Dissolution pores under the optical microscope photograph. **(a)** Dissolution pores filled with clay minerals. **(b)** Dissolution pores that have not been filled with any minerals. **(c)** Intragranular dissolution pores of feldspar. **(d)** Moldic pores.

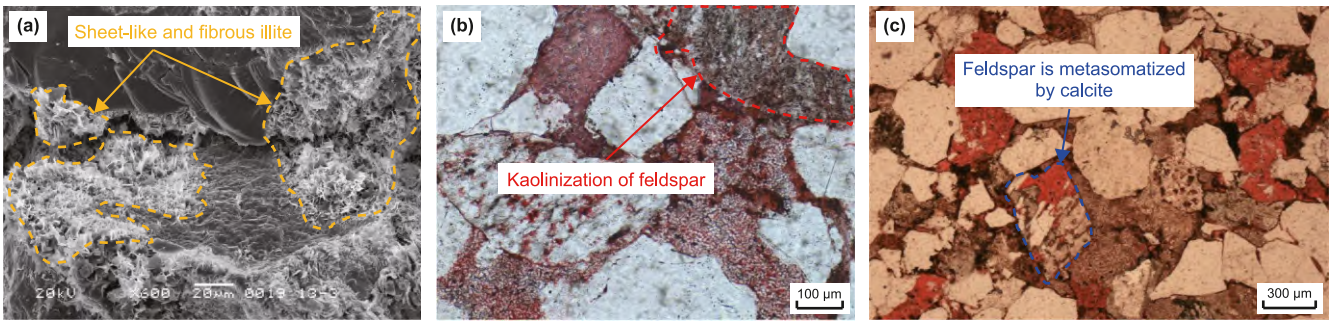

Fig. 9. Scanning electron microscope and optical microscope photographs of the metasomatism. **(a)** Quartz is metasomatized to form sheet-like illite that adheres to its surface. **(b)** Feldspar is metasomatized by kaolinite and the kaolinite adheres to its surface. **(c)** Part of the feldspar is metasomatized by calcite.

including the replacement of quartz by illite (Fig. 9(a)), the replacement of feldspar by kaolinite (Fig. 9(b)), and the replacement of feldspar by calcite (Fig. 9(c)).

4.4. Diagenetic sequence

The vitrinite reflectance (R_o) values of the Upper Paleozoic strata in the study area range from 0.5% to 2.0% (Su et al., 2021). According to the classification standard of diagenetic stages of clastic rocks in China (SY/T 5477–2003), the Shanxi Formation in the study area is currently mainly in the middle diagenetic stage B. The diagenetic evolution of the Shanxi Formation is divided into the following four stages (Fig. 10) (Su et al., 2021; Yang et al., 2012).

The early diagenesis Stage A (R_o < 0.35%, 0–65 °C, 300–250 Ma ago): the rocks were weakly to semi-consolidated, and the primary pores were developed. During the early syngenetic stage, the leaching of acidic atmospheric water led to the hydrolysis of volcanic ash materials, providing a large amount of Fe^{2+}, Fe^{3+}, and Al^{3+} (Burger et al., 2002; Hagar et al., 2022). In this stage, the alkaline environment created by groundwater led to the formation of chlorite films, and also resulted in the formation of early calcite and siderite cementation (Li et al., 2021). The compaction strongly damaged the pore space, and the initial porosity decreased rapidly. At the same time, the fracturing made large brittle particles prone to the formation of microfractures, and ductile particles deformed.

The early diagenesis Stage B (0.35% < R_o < 0.5%, 65–85 °C, 250–220 Ma ago): the rock transitioned from semi-solid to consolidated, in a manner influenced by the compaction and cementation. The reservoir is mainly composed of primary pores, with a small number of secondary pores. Acidic substances such as humic acid and fulvic acid discharged from the coal seam cause the dissolution of feldspar and volcanic materials (Patrick et al., 1984), providing conditions for the formation of authigenic kaolinite and altered kaolinite.

The middle diagenesis Stage A (0.5% < R_o < 1.3%, 85–140 °C, 220–110 Ma ago): the organic matter begins to mature, releasing a large amount of organic acids (Zhu et al., 2015). In a strongly acidic environment, feldspar, rock fragments, early-stage calcite, siderite, and chlorite films are dissolved, forming a large number of dissolved pores. Clay minerals such as kaolinite and illite begin to form. At the end of this stage, late-stage carbonate cementation appears.

The middle diagenesis Stage B (1.3% < R_o < 2.0%, 140–175 °C, 110 Ma ago to the present day): the organic matter is highly mature, and a large amount of organic acids are no longer produced, and the dissolution stops (Sun et al., 2021; Zhang et al., 2022). The environment gradually transitions to an alkaline state, and late-stage carbonate cementation appears to fill the pore space, leading to further densification of the reservoir (Shao et al., 2019). Kaolinite and mixed illite/smectite are transformed into illite. Microfractures occur in brittle particles.

4.5. Heterogeneity of lithofacies reservoir spaces within architectural elements

4.5.1. Heterogeneity of the contents of different types of pores

By statistically analyzing the relative contents of different types of pores in lithofacies under the constraint of architectural elements (202 data points), the following rules can be summarized: residual intergranular pores in BBt3 and MFCH are more developed, followed by BBt2, while BBt1 and MB are relatively less developed; dissolution pores in BBt1 are relatively more developed, followed by BBt2, BBt3, and MB, with MFCH being relatively less developed; Intercrystalline pores in MB are relatively more developed, followed by BBt2, BBt3, and MFCH, with BBt1 being relatively less developed; Microfractures in BBt1 are relatively more developed, followed by BBt2, BBt3, and MB, with MFCH being poorly developed (Fig. 11(a)).

By further comparing the relative contents of various types of pores in lithofacies within architectural elements (Fig. 11(b)–(f)), it is found that there are similarities in the patterns of pore contents of various lithofacies within different architectural elements. In terms of the content of residual intergranular pores, the order from high to low is: Sr > Gm (or Sp) > Stc > Spc. In terms of the content of dissolution pores, the order from high to low is: Stc (or Gm, Spc) > Sp > Sr. In terms of the content of intercrystalline pores, the order from high to low is: Sp (or Spc) > Stc > Gm > Sr. In terms of the content of microfractures, the order from high to low is: Stc > Spc > Sp > Gm > Sr.

4.5.2. Heterogeneity of the contents of different types of throats

By statistically analyzing the relative contents of different types of throats in lithofacies under the constraint of architectural elements (202 data points), the following rules can be summarized: the neck-shaped throats in BBt1 are the most developed, followed by BBt2, BBt3, and MB, while MFCH is less developed; the sheet-like/curved sheet-like throats in BBt1 and BBt2 are the most developed, followed by BBt3 and MB, while MFCH is less developed; the bundled tubular throats in BBt3 and MFCH are the most developed, followed by MB, while BBt1 and BBt2 are less developed (Fig. 12(a)).

By further comparing the relative contents of different types of throats in lithofacies within architectural elements (Fig. 12(b)–(f)), it is found that there are similarities in the patterns of throat contents of various lithofacies within different architectural elements. The relative contents of neck-shaped throats are ranked as follows: Stc > Spc > Gm > Sp > Sr. The relative contents of sheet-like/curved sheet-like throats are ranked as follows:

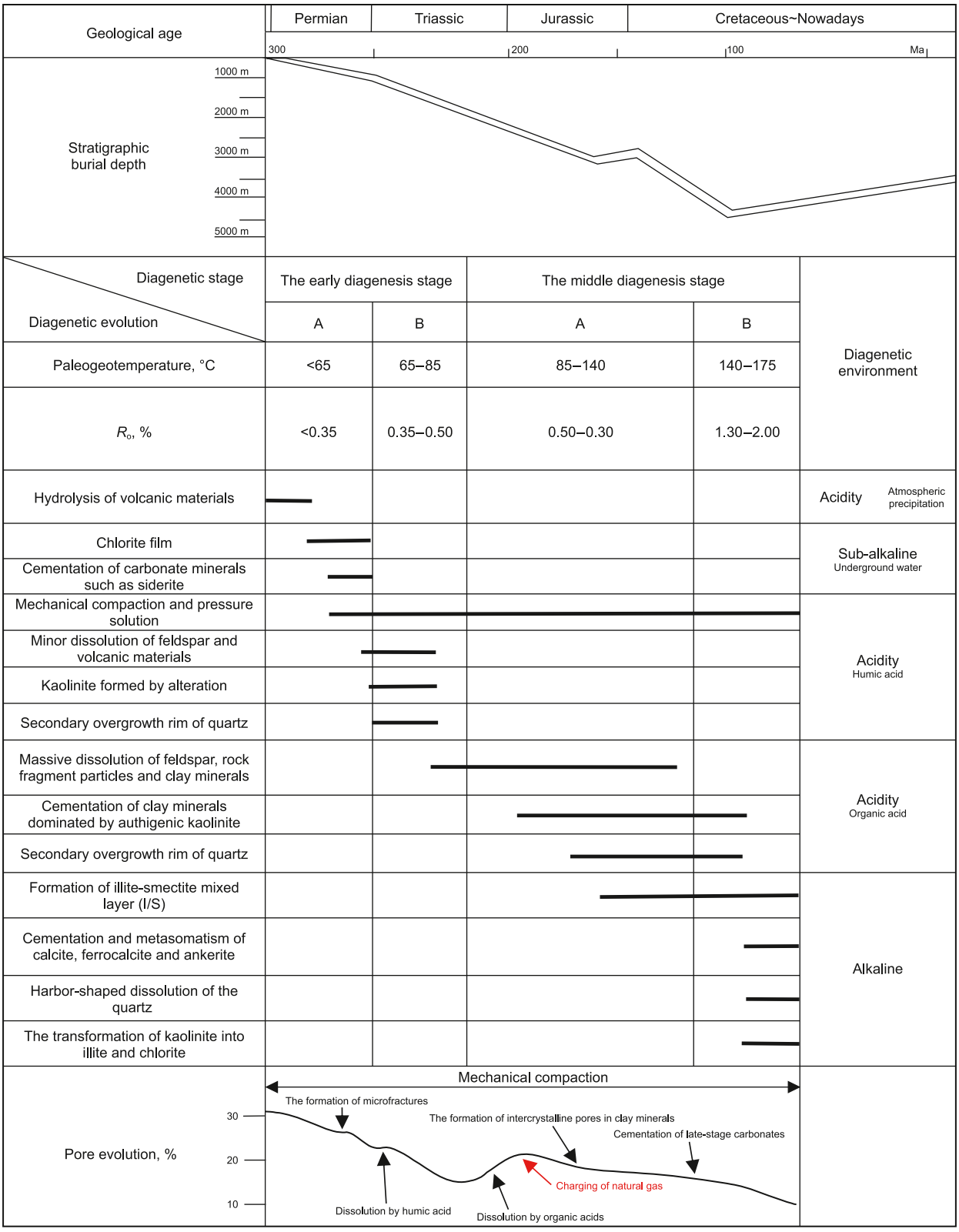

Fig. 10. The diagenetic evolution sequence of the Shanxi Formation in the study area.

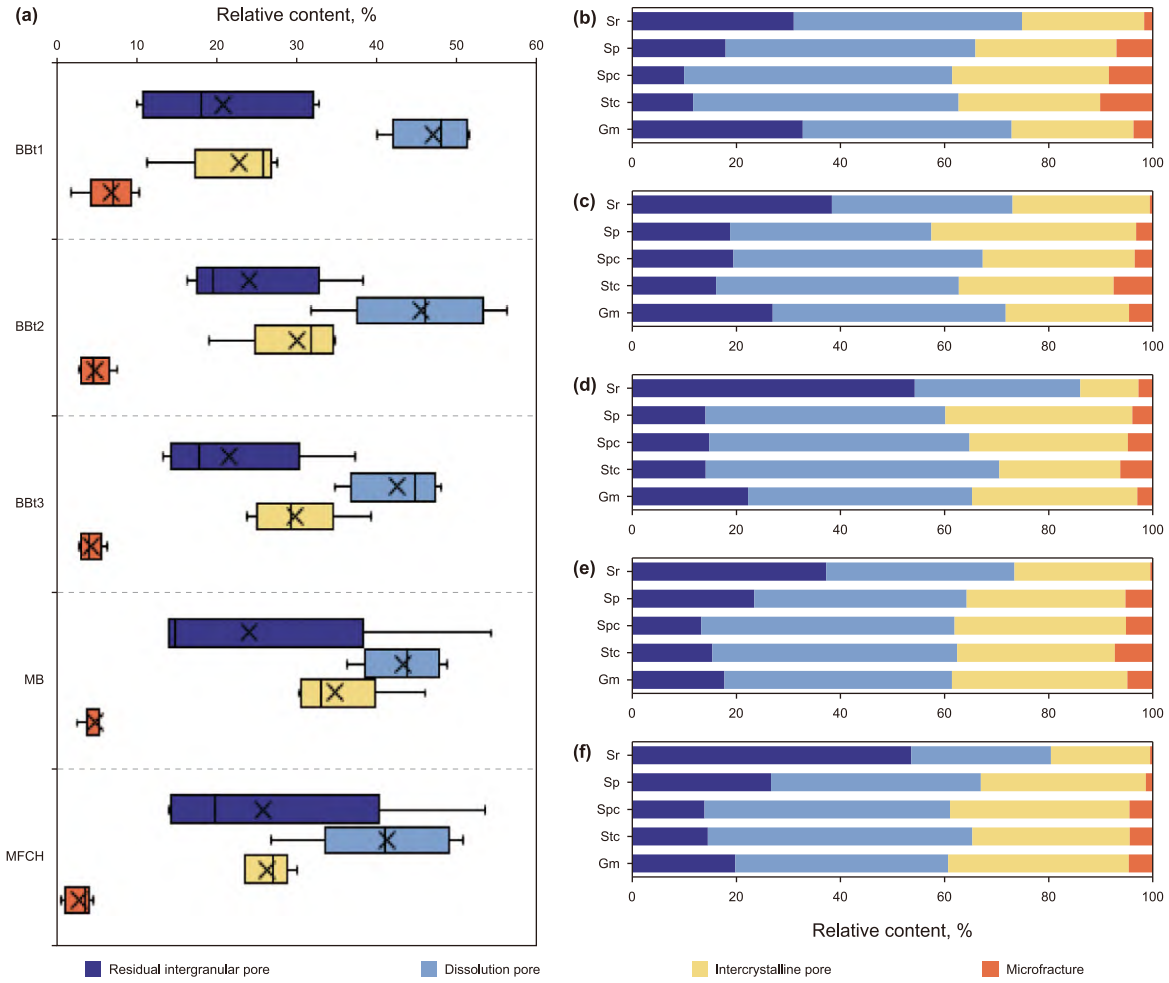

Fig. 11. Pore content variations in different pore types among lithofacies and architectural elements. **(a)** Distribution of various pore contents in different architectural elements. **(b)** Pore type content variations in lithofacies of BBt1. **(c)** Pore type content variations in lithofacies of BBt2. **(d)** Pore type content variations in lithofacies of BBt3. **(e)** Pore type content variations in lithofacies of MB. **(f)** Pore type content variations in lithofacies of MFCH.

Sr > Gm > Sp > Stc > Spc. The relative contents of bundled tubular throats are ranked as follows: Sp > Sr > Gm > Spc > Stc.

4.6. Heterogeneity of the reservoir quality of lithofacies within architectural elements

4.6.1. Heterogeneity of reservoir physical properties

By statistically analyzing the core porosity data (Por_Core) of the reservoirs of various architectural elements, it can be known that the overall porosity ranking of various architectural elements is: BBt1 > BBt2 > MB > BBt3 > MFCH (Fig. 13). By further statistically analyzing the porosity data of various lithofacies, the porosity patterns of lithofacies within each architectural element are as follows: With the increase of porosity, the proportion of samples of Stc and Spc gradually increases, while the proportions of Gm, Sp, and Sr gradually decrease. This indicates that: Stc and Spc are mainly characterized by high porosity; Sr is mainly characterized by low porosity; Both high and low porosities are developed in Gm and Sp, among which higher porosities are slightly more in Gm, and lower porosities are slightly more in Sp.

By statistically analyzing the air permeability (Perm_Core) of the reservoir cores of various architectural elements, it can be known that the overall permeability ranking of various architectural elements is: BBt1 > BBt2 > MB > BBt3 > MFCH (Fig. 14), among which the permeability of BBt2 is slightly better than that of MB, and the permeability of BBt3 is slightly better than that of MFCH. By further statistically analyzing the permeability data of various lithofacies, it can be seen that the variation pattern of permeability is similar to that of porosity. That is, among the samples of each lithofacies within the architectural elements, with the increase of permeability, the proportion of samples of Stc and Spc gradually increases, while the proportions of Gm, Sp, and Sr gradually decrease. This indicates that: Stc and Spc are mainly characterized by high permeability; Sr is mainly characterized by low permeability; Gm is mainly characterized by medium-high permeability; Sp is mainly characterized by medium-low permeability.

4.6.2. Heterogeneity of reservoir fluid mobility

By statistically analyzing the irreducible water saturation (Swi_Core) of the reservoir cores of various architectural elements, it can be known that the overall irreducible water saturation ranking of various architectural elements is: MFCH > BBt3 > MB > BBt2 > BBt1 (Fig. 15), which indicates that the overall fluid mobility of BBt1 is the best, and the overall fluid mobility of MFCH is the worst. By further statistically analyzing the irreducible water saturation data of various lithofacies, it can be seen that among the samples of each lithofacies within the architectural elements, with the increase of irreducible water saturation, the proportions of samples of Stc, Spc, and Gm gradually

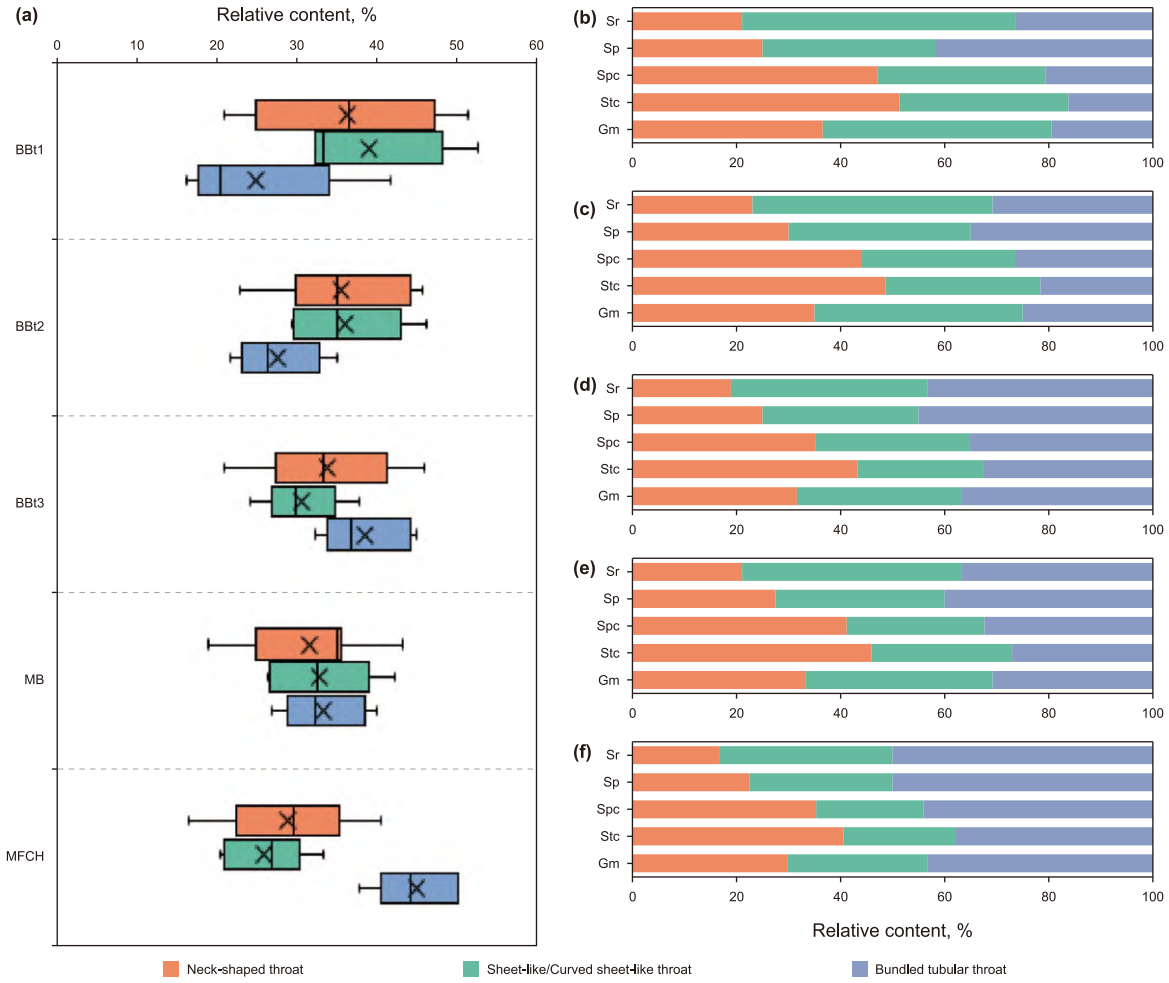

Fig. 12. Throat content variations in different throat types among lithofacies and architectural elements. **(a)** Distribution of various throat contents in different architectural elements. **(b)** Throat type content variations in lithofacies of BBt1. **(c)** Throat type content variations in lithofacies of BBt2. **(d)** Throat type content variations in lithofacies of BBt3. **(e)** Throat type content variations in lithofacies of MB. **(f)** Throat type content variations in lithofacies of MFCH.

decrease, the proportion of Sr gradually increases, and the proportion of Sp first increases and then decreases. This indicates that: Stc and Spc are mainly characterized by good fluid mobility; Gm is mainly characterized by relatively good fluid mobility; Sp is mainly characterized by poor fluid mobility; Sr is mainly characterized by poor fluid mobility.

4.7. Sedimentary and diagenetic heterogeneity of architectural elements

4.7.1. Sedimentary heterogeneity of architectural elements

Based on the formulas (Eq. (2) and Eq. (3)) for quantitatively characterizing the sedimentary heterogeneity of architectural elements, the total lithofacies density (D_{TL}) and lithofacies frequency (LF) of different architectural elements in the braided river facies and meandering river facies reservoirs were statistically analyzed, and the following characteristics were summarized:

Type-1 braided river bar (BBt1): judging from the D_{TL} and LF (Table 6), Stc is the most developed in BBt1, and the overall sedimentation is mainly coarse-grained sandstone. The D_{TL} and LF of Mm are low, indicating that the mudstone interlayers are not well developed within this architectural element. The LF of Sp, Spc, and Stc are high, indicating that there are usually sedimentary cycle characteristics of multi-stage coarse-medium grained sandstone within this architectural element.

Type-2 braided river bar (BBt2): judging from the D_{TL} and LF (Table 6), Sp and Spc are the most developed in BBt2, and the overall sedimentation is mainly medium-fine grained sandstone. The LF of Mm and Sr are moderate, indicating that the silty mudstone interlayers are relatively well developed within this architectural element. The LF of Mm, Sr, Sp, and Spc are high, indicating that there are usually sedimentary cycle characteristics of multi-stage medium-coarse grained sandstone-mudstone within this architectural element.

Type-3 braided river bar (BBt3): judging from the D_{TL} and LF (Table 6), Mm is the most developed in BBt3, and the overall sedimentation is mainly medium-fine grained sandstone. The D_{TL} and LF of Mm are high, indicating that the silty mudstone interlayers are well developed and have a large thickness within this architectural element. Except for Gm, the LF of the other lithofacies are high, indicating that there are usually sedimentary cycle characteristics of multi-stage medium-grained sandstone-mudstone within this architectural element.

Meandering river bar (MB): judging from the D_{TL} and LF (Table 7), Sp and Spc are the most developed in MB, and the overall sedimentation is mainly medium-fine grained sandstone. The LF of Mm and Sr are moderate, indicating that the pure mudstone interlayers are relatively well developed within this architectural element. The LF of Sp and Spc are high, indicating that there are usually sedimentary cycle characteristics of multi-stage medium-

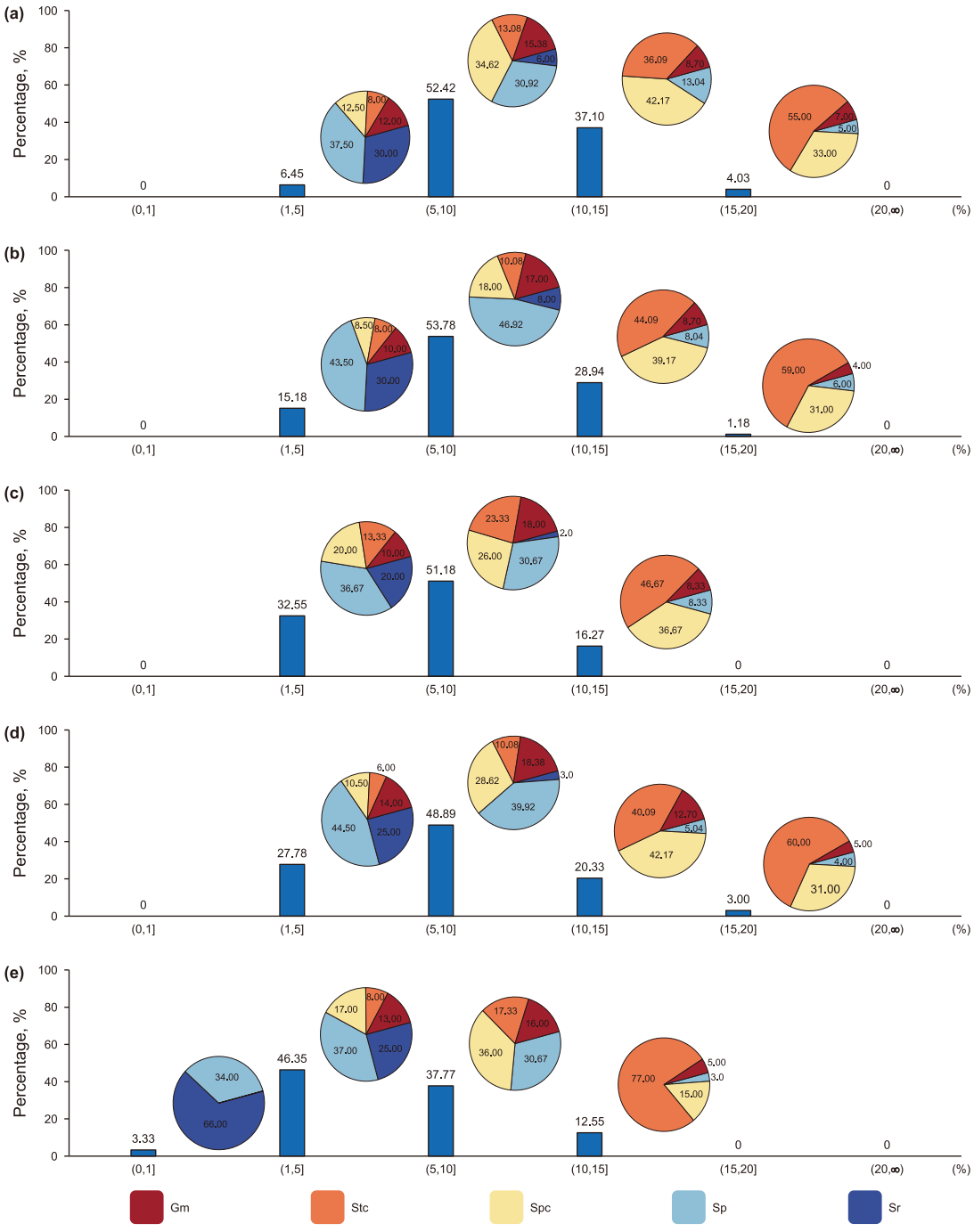

Fig. 13. Porosity distribution of architectural elements and lithofacies proportions within different porosity intervals. **(a)** Porosity distribution of BBt1 and lithofacies proportions within porosity intervals. **(b)** Porosity distribution of BBt2 and lithofacies proportions within porosity intervals. **(c)** Porosity distribution of BBt3 and lithofacies proportions within porosity intervals. **(d)** Porosity distribution of MB and lithofacies proportions within porosity intervals. **(e)** Porosity distribution of MFCH and lithofacies proportions within porosity intervals.

coarse grained sandstone-mudstone within this architectural element.

Meandering river final—stage channel (MFCH): judging from the D_{TL} and LF (Table 7), Mm is the most developed in MFCH, and the overall sedimentation is mainly fine-grained sandstone-mudstone. The D_{TL} of Mm is large and the LF is low, indicating that thick mudstone is well developed within this architectural element. Except for Sp, the LF of the other lithofacies are low, indicating that multi-stage sedimentary cycles are less developed within this architectural element.

In conclusion, this study further calculated the total lithofacies density and lithofacies frequency of sandstone and conglomerate lithofacies (including Gm, Stc, Spc, and Sp), siltstone lithofacies (Sr), and mudstone lithofacies (Mm) within architectural elements, and based on these values, established grade criteria for evaluating the degree of heterogeneity (Table 8). Specifically, in the braided river facies reservoir: BBt1 exhibits weak sedimentary heterogeneity dominated by sand; BBt2 shows moderate sedimentary heterogeneity; and BBt3 presents strong sedimentary heterogeneity. In the meandering river facies reservoir: MB

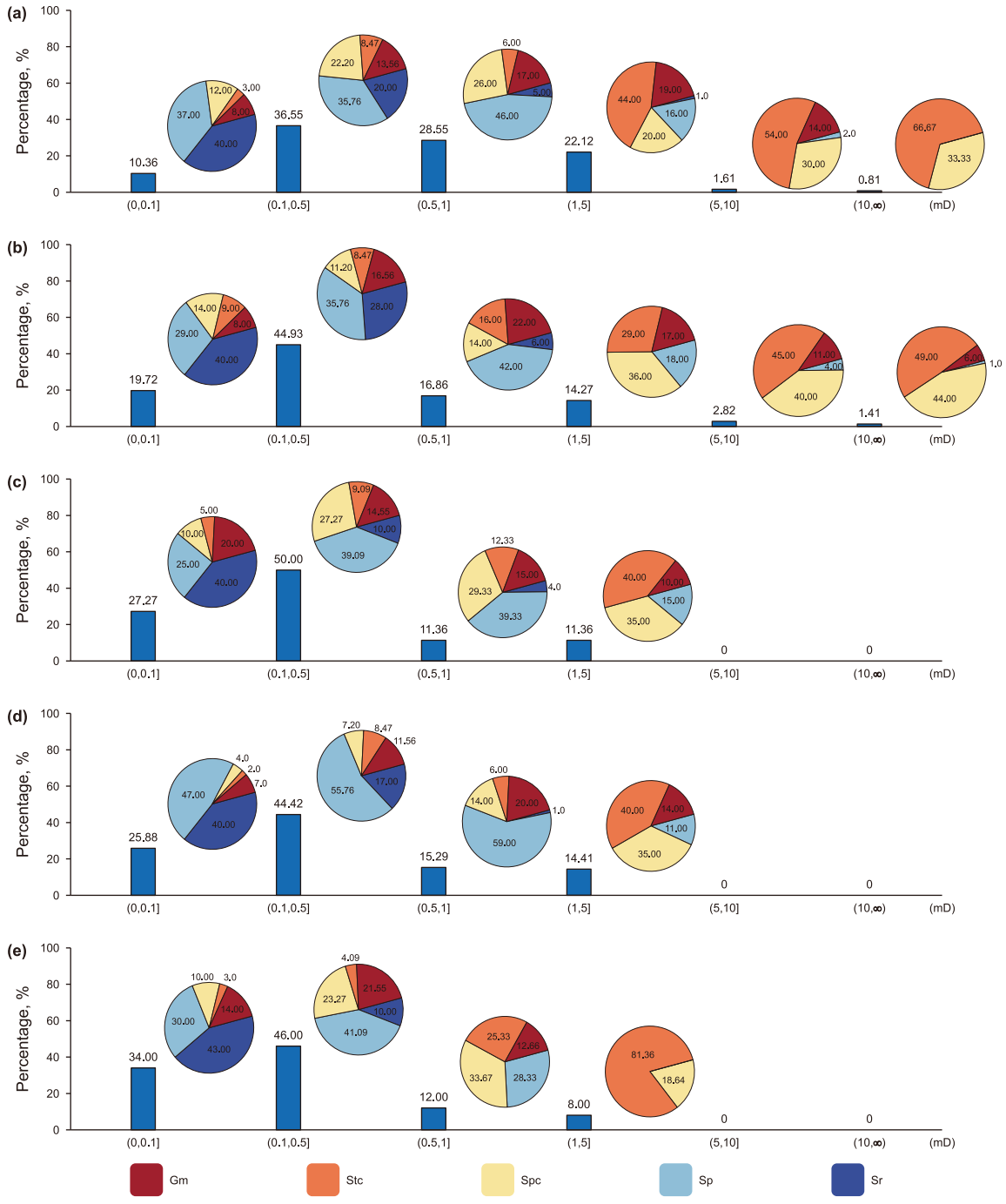

Fig. 14. Permeability distribution of architectural elements and lithofacies proportions within different permeability intervals. **(a)** Permeability distribution of BBt1 and lithofacies proportions within permeability intervals. **(b)** Permeability distribution of BBt2 and lithofacies proportions within permeability intervals. **(c)** Permeability distribution of BBt3 and lithofacies proportions within permeability intervals. **(d)** Permeability distribution of MB and lithofacies proportions within permeability intervals. **(e)** Permeability distribution of MFCH and lithofacies proportions within permeability intervals.

displays moderate sedimentary heterogeneity; while MFCH demonstrates weak sedimentary heterogeneity dominated by mud.

4.7.2. Diagenetic heterogeneity of architectural elements

Based on the formulas for quantitatively characterizing the diagenetic strength, and according to the vertical superposition sequences of lithofacies of different architectural elements in the braided river facies and meandering river facies reservoirs, the strengths of various diagenetic processes of lithofacies at different positions were statistically analyzed, and the following characteristics were summarized:

BBt1: BBt1 develops multiple short-period cycles (Fig. 16(a)), and the initial porosities of various lithofacies within it have small differences, ranging from 31% to 33%, among which the initial porosities of Gm, Stc, and Spc are slightly higher (Fig. 16(b)). In terms of compaction, the compaction strength of Sr in each short-period cycle is high, and the compaction strength of Sr in the middle and lower short-period cycles is higher than that in the upper part. The development strength of microfractures caused by

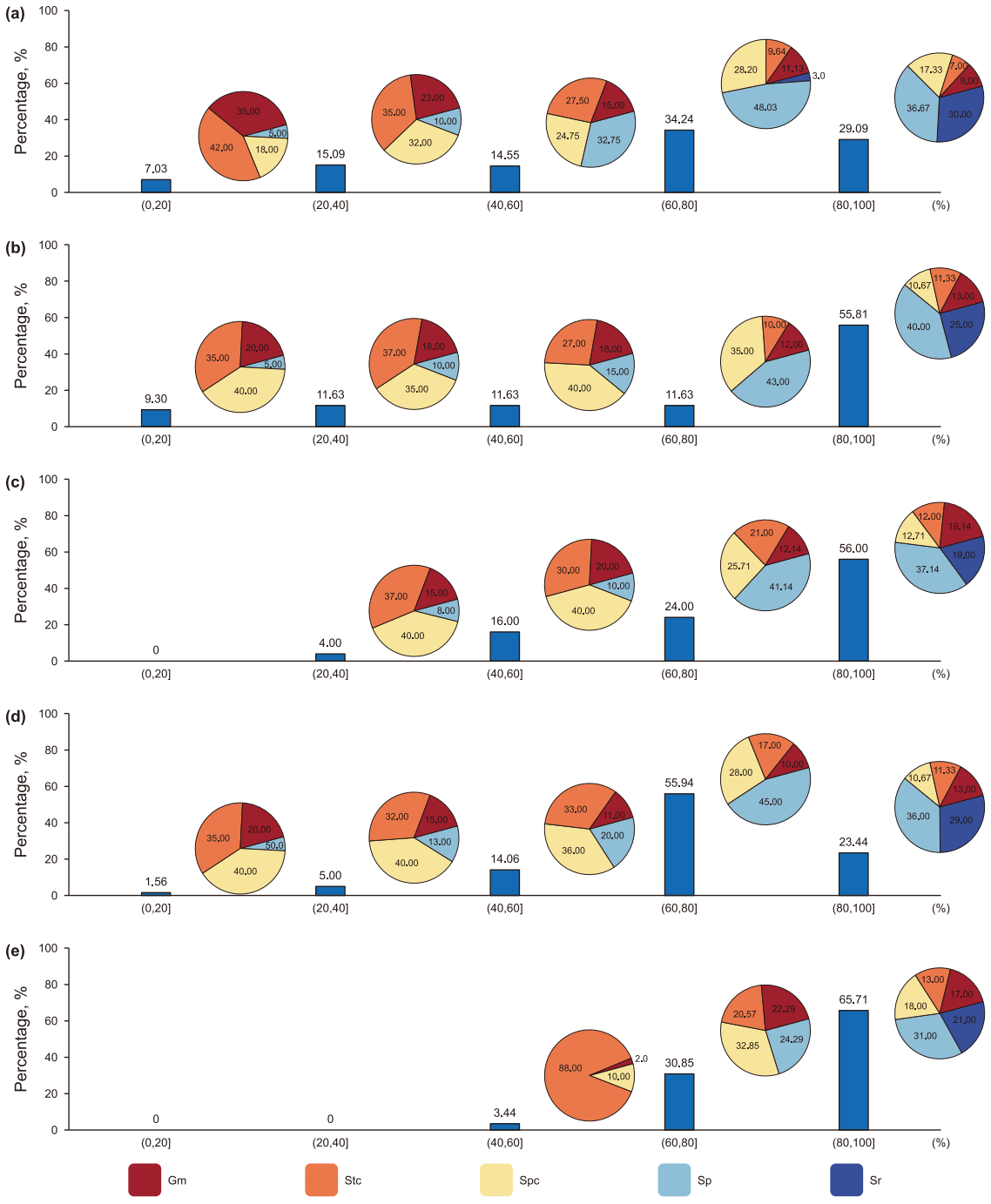

Fig. 15. Irreducible water saturation distribution of architectural elements and lithofacies proportions within different irreducible water saturation intervals. **(a)** Irreducible water saturation distribution of BBt1 and lithofacies proportions within irreducible water saturation intervals. **(b)** Irreducible water saturation distribution of BBt2 and lithofacies proportions within irreducible water saturation intervals. **(c)** Irreducible water saturation distribution of BBt3 and lithofacies proportions within irreducible water saturation intervals. **(d)** Irreducible water saturation distribution of MB and lithofacies proportions within irreducible water saturation intervals. **(e)** Irreducible water saturation distribution of MFCH and lithofacies proportions within irreducible water saturation intervals.

fracturing is the greatest in Stc and Spc in each short-period cycle, and weakens as the grain size of the lithofacies decreases (Fig. 16(b)). The dissolution shows that the dissolution strength of Stc and Spc in each short-period cycle is significantly greater than that of Sp and Sr, and weakens as the grain size of the lithofacies decreases. The cementation strength of clay minerals shows that the cementation strength of various lithofacies in the upper short-period cycle is higher than that in the middle and lower parts, among which Sp and Sr are the highest; the cementation strength of Gm at the bottom is slightly higher than that of other lithofacies in the lower and middle short-period cycles (Fig. 16(b)). The development strength of intercrystalline pores of clay minerals shows that Spc and Stc are relatively high in each short period (Fig. 16(b)), among which the development strength of Spc and Stc in the upper part is relatively the highest, and the development strength of intercrystalline pores of clay minerals in various lithofacies of the upper short-period cycle is significantly higher than that of other short-period cycles. The cementation strength of

Table 6
Distribution of range values and mean values of sedimentary heterogeneity characterization parameters of lithofacies in different architectural elements of braided river facies reservoirs.

Architecture element	Lithofacies	D_{TL}		LF	
		Range, %	Mean, %	Range, %	Mean, %
BBt1	Mm[a]	3.10~13.45	8.90	2.39~8.33	4.25
	Sr[b]	8.52~16.86	10.72	6.25~12.50	15.45
	Sp[c]	7.58~34.24	19.67	10.00~33.33	22.82
	Spc[d]	9.92~42.42	27.01	11.11~41.67	25.06
	Stc[e]	16.14~47.90	32.48	14.29~33.33	24.36
	Gm[f]	5.15~15.00	9.21	6.25~16.67	9.09
BBt2	Mm	7.20~25.70	16.36	8.33~31.58	15.03
	Sr	3.16~12.00	8.06	8.16~29.25	13.25
	Sp	9.20~41.13	22.28	10.10~38.33	23.25
	Spc	13.45~38.85	21.46	10.53~36.55	19.58
	Stc	5.88~30.85	17.53	11.53~23.08	13.24
	Gm	4.23~12.02	6.57	5.26~15.38	7.64
BBt3	Mm	26.44~32.09	30.48	14.29~28.57	19.48
	Sr	3.17~15.46	8.53	11.11~23.66	17.89
	Sp	8.46~34.85	24.62	14.29~27.67	18.42
	Spc	6.16~32.24	19.61	11.11~33.33	19.66
	Stc	7.22~23.06	15.94	11.11~28.25	17.61
	Gm	5.56~12.62	6.84	3.33~14.29	6.93

[a] Mm refers to massive bedding mudstone; [b] Sr refers to ripple bedding sandstone; [c] Sp refers to parallel bedding sandstone; [d] Spc refers to plate cross-bedding sandstone; [e] Stc refers to trough cross-bedding sandstone; [f] Gm refers to massive bedding conglomerate.

Table 7
Distribution of range values and mean values of sedimentary heterogeneity characterization parameters of lithofacies in different architectural elements of meandering river facies reservoirs.

Architecture element	Lithofacies	D_{TL}		LF	
		Range, %	Mean, %	Range, %	Mean, %
MB	Mm[a]	9.23~22.44	16.33	11.11~20.00	18.47
	Sr[b]	2.43~13.86	6.55	9.09~33.33	13.09
	Sp[c]	14.57~31.65	23.68	15.38~40.00	27.45
	Spc[d]	14.71~42.51	25.37	12.50~37.33	22.57
	Stc[e]	8.32~26.14	14.26	8.33~28.57	11.50
	Gm[f]	4.76~21.57	8.84	5.88~14.29	8.92
MFCH	Mm	36.33~43.33	39.33	9.32~12.19	10.27
	Sr	17.56~33.00	22.70	7.48~10.03	8.29
	Sp	12.67~39.22	28.56	11.36~17.83	12.54
	Spc	4.33~14.71	9.78	8.00~16.00	11.70
	Stc	5.66~10.02	7.78	4.12~13.25	8.70
	Gm	0.00~9.00	3.00	0.00~8.33	4.33

[a] Mm refers to massive bedding mudstone; [b] Sr refers to ripple bedding sandstone; [c] Sp refers to parallel bedding sandstone; [d] Spc refers to plate cross-bedding sandstone; [e] Stc refers to trough cross-bedding sandstone; [f] Gm refers to massive bedding conglomerate.

Table 8
Grade criteria for the degree of heterogeneity of architectural elements.

Grade	Sandstone and conglomerate (Gm, Stc, Spc, Sp)		Siltstone (Sr)		Mudstone (Mm)	
	D_{TL}, %	LF, %	D_{TL}, %	LF, %	D_{TL}, %	LF, %
Strong	< 65	< 65	< 10	> 20	< 25	> 20
Moderate	65–75	65–75	10–15	15–20	10–15	15–20
Weak	> 75	> 75	> 15	< 15	< 10 or > 35	< 15

carbonate minerals is more controlled by the position of lithofacies, has a small correlation with the lithofacies type, and shows the characteristics of high at the top and bottom and weak in the center (Fig. 16(b)).

BBt2: Similar to BBt1, BBt2 also develops multiple short-period cycles (Fig. 17(a)). However, silty mudstone interlayers are present within BBt2, which is a significant difference between the two. The initial porosities of various lithofacies within BBt2 have small differences, ranging from 30% to 33%, among which the initial porosities of Gm, Stc and Spc are slightly higher (Fig. 17(b)). The heterogeneity characteristics of the compaction strength are consistent with those of BBt1, with Sr having the highest strength. The heterogeneity characteristics of the development strength of microfractures and the dissolution strength are also consistent with those of BBt1. The strength of different lithofacies in each short-period cycle weakens as the grain size decreases, but the overall values of BBt2 are slightly lower. The cementation strength of clay minerals in BBt2 is generally stronger than that in BBt1. And as the thickness of the silty mudstone interlayers increases from bottom to top, each short-period cycle shows an increasing trend. In addition, the cementation strength of clay minerals in each lithofacies weakens as the distance from the silty mudstone interlayers increases (Fig. 17(b)). The development strength of intercrystalline pores of clay minerals in each short-period cycle is

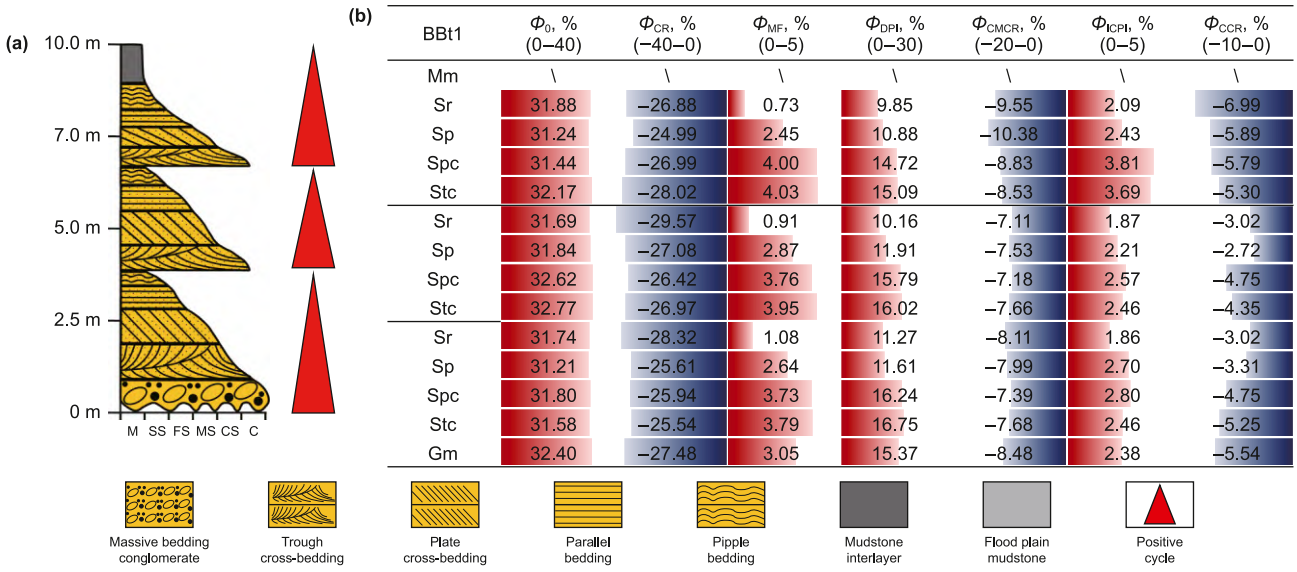

BBt1	Φ_0, % (0–40)	Φ_{CR}, % (−40–0)	Φ_{MF}, % (0–5)	Φ_{DPI}, % (0–30)	Φ_{CMCR}, % (−20–0)	Φ_{ICPI}, % (0–5)	Φ_{CCR}, % (−10–0)
Mm	\	\	\	\	\	\	\
Sr	31.88	−26.88	0.73	9.85	−9.55	2.09	−6.99
Sp	31.24	−24.99	2.45	10.88	−10.38	2.43	−5.89
Spc	31.44	−26.99	4.00	14.72	−8.83	3.81	−5.79
Stc	32.17	−28.02	4.03	15.09	−8.53	3.69	−5.30
Sr	31.69	−29.57	0.91	10.16	−7.11	1.87	−3.02
Sp	31.84	−27.08	2.87	11.91	−7.53	2.21	−2.72
Spc	32.62	−26.42	3.76	15.79	−7.18	2.57	−4.75
Stc	32.77	−26.97	3.95	16.02	−7.66	2.46	−4.35
Sr	31.74	−28.32	1.08	11.27	−8.11	1.86	−3.02
Sp	31.21	−25.61	2.64	11.61	−7.99	2.70	−3.31
Spc	31.80	−25.94	3.73	16.24	−7.39	2.80	−4.75
Stc	31.58	−25.54	3.79	16.75	−7.68	2.46	−5.25
Gm	32.40	−27.48	3.05	15.37	−8.48	2.38	−5.54

Fig. 16. The diagenetic heterogeneity of BBt1. **(a)** The vertical stacking sequence of lithofacies of BBt1. **(b)** Statistics of the intensity of diagenesis under the constraint of the sedimentary sequence of BBt1.

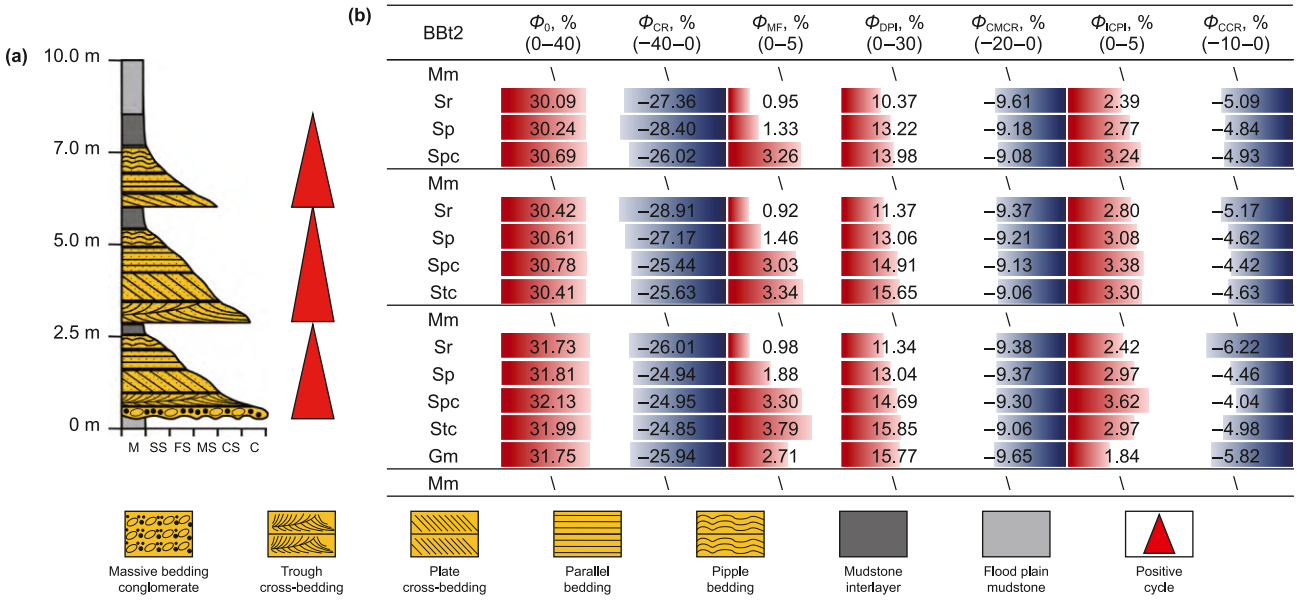

BBt2	Φ_0, % (0–40)	Φ_{CR}, % (−40–0)	Φ_{MF}, % (0–5)	Φ_{DPI}, % (0–30)	Φ_{CMCR}, % (−20–0)	Φ_{ICPI}, % (0–5)	Φ_{CCR}, % (−10–0)
Mm	\	\	\	\	\	\	\
Sr	30.09	−27.36	0.95	10.37	−9.61	2.39	−5.09
Sp	30.24	−28.40	1.33	13.22	−9.18	2.77	−4.84
Spc	30.69	−26.02	3.26	13.98	−9.08	3.24	−4.93
Mm	\	\	\	\	\	\	\
Sr	30.42	−28.91	0.92	11.37	−9.37	2.80	−5.17
Sp	30.61	−27.17	1.46	13.06	−9.21	3.08	−4.62
Spc	30.78	−25.44	3.03	14.91	−9.13	3.38	−4.42
Stc	30.41	−25.63	3.34	15.65	−9.06	3.30	−4.63
Mm	\	\	\	\	\	\	\
Sr	31.73	−26.01	0.98	11.34	−9.38	2.42	−6.22
Sp	31.81	−24.94	1.88	13.04	−9.37	2.97	−4.46
Spc	32.13	−24.95	3.30	14.69	−9.30	3.62	−4.04
Stc	31.99	−24.85	3.79	15.85	−9.06	2.97	−4.98
Gm	31.75	−25.94	2.71	15.77	−9.65	1.84	−5.82
Mm	\	\	\	\	\	\	\

Fig. 17. The diagenetic heterogeneity of BBt2. **(a)** The vertical stacking sequence of lithofacies of BBt2. **(b)** Statistics of the intensity of diagenesis under the constraint of the sedimentary sequence of BBt2.

consistent with that in BBt1, but the development strength of lithofacies close to or in contact with the silty mudstone interlayers increases significantly, and is overall higher than that in BBt1 (Fig. 17(b)). The cementation strength of carbonate minerals is more controlled by the position of lithofacies and has a small relationship with the lithofacies type, with the cementation strengths of Sr at the topmost and Gm at the bottommost being the highest (Fig. 17(b)).

BBt3: BBt3 is similar to BBt2, with multiple short-period cycles developed and silty mudstone interlayers contained (Fig. 18(a)), but the thickness of the mudstone at the top is greater. The initial porosities of various lithofacies within BBt3 have small differences, ranging from 29% to 33%, among which the initial porosities of Stc, Spc, and Sp are slightly higher (Fig. 18(b)). The compaction strengths of Sp and Sr within each short-period cycle are relatively high. Overall, the development strength of microfractures caused by fracturing in BBt3 is lower than that in BBt1 and BBt2, but the development strength of microfractures in Stc is relatively high. In terms of the dissolution strength, the dissolution strength of lithofacies within each short-period cycle in BBt3 is close to that in BBt2, but lower than that in BBt1, and the variation trend is consistent with that in BBt1 and BBt2 (Fig. 18(b)). The cementation strength of clay minerals shows that the upper short-period cycle is higher than the lower one, and the cementation strength of lithofacies in contact with the internal silty mudstone interlayers increases significantly. Generally, the cementation strength of clay minerals in BBt3 is higher than that in BBt1 and BBt2, among which the cementation strengths of Spc and Sp are particularly high (Fig. 18(b)). The development strength of intercrystalline pores of clay minerals shows that the development strength of Spc

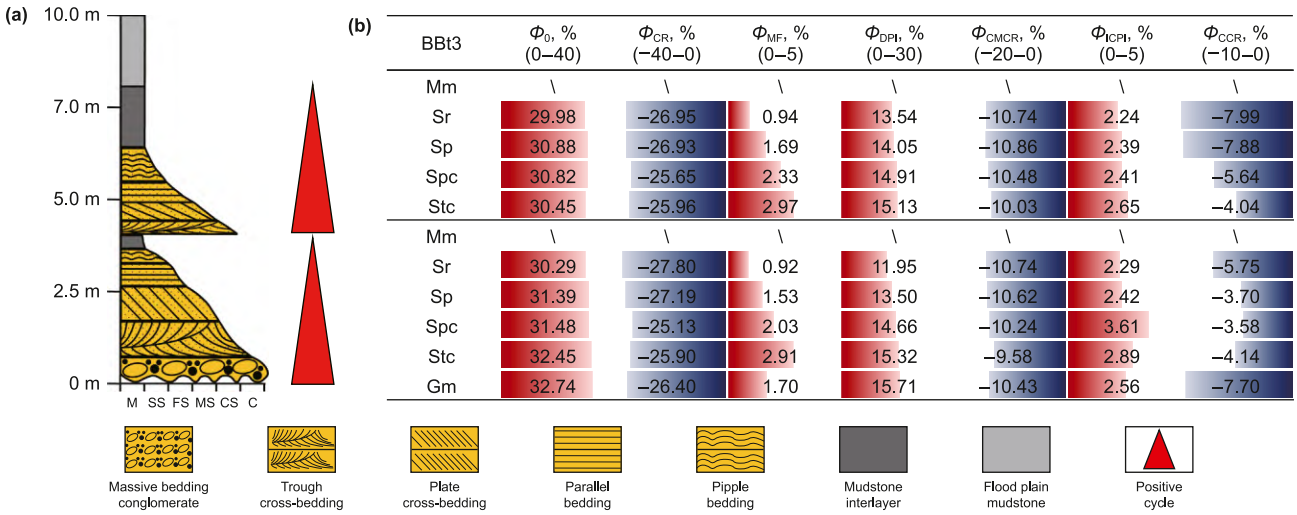

BBt3	Φ_0, % (0–40)	Φ_{CR}, % (−40–0)	Φ_{MF}, % (0–5)	Φ_{DPI}, % (0–30)	Φ_{CMCR}, % (−20–0)	Φ_{ICPI}, % (0–5)	Φ_{CCR}, % (−10–0)
Mm	\	\	\	\	\	\	\
Sr	29.98	−26.95	0.94	13.54	−10.74	2.24	−7.99
Sp	30.88	−26.93	1.69	14.05	−10.86	2.39	−7.88
Spc	30.82	−25.65	2.33	14.91	−10.48	2.41	−5.64
Stc	30.45	−25.96	2.97	15.13	−10.03	2.65	−4.04
Mm	\	\	\	\	\	\	\
Sr	30.29	−27.80	0.92	11.95	−10.74	2.29	−5.75
Sp	31.39	−27.19	1.53	13.50	−10.62	2.42	−3.70
Spc	31.48	−25.13	2.03	14.66	−10.24	3.61	−3.58
Stc	32.45	−25.90	2.91	15.32	−9.58	2.89	−4.14
Gm	32.74	−26.40	1.70	15.71	−10.43	2.56	−7.70

Fig. 18. The diagenetic heterogeneity of BBt3. **(a)** The vertical stacking sequence of lithofacies of BBt3. **(b)** Statistics of the intensity of diagenesis under the constraint of the sedimentary sequence of BBt3.

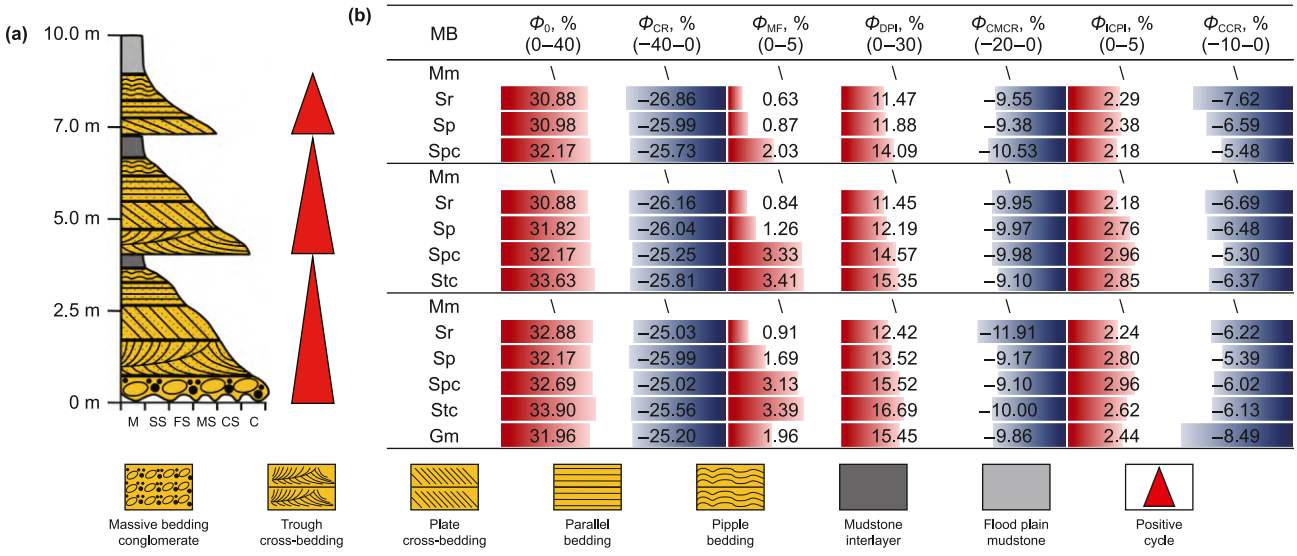

MB	Φ_0, % (0–40)	Φ_{CR}, % (−40–0)	Φ_{MF}, % (0–5)	Φ_{DPI}, % (0–30)	Φ_{CMCR}, % (−20–0)	Φ_{ICPI}, % (0–5)	Φ_{CCR}, % (−10–0)
Mm	\	\	\	\	\	\	\
Sr	30.88	−26.86	0.63	11.47	−9.55	2.29	−7.62
Sp	30.98	−25.99	0.87	11.88	−9.38	2.38	−6.59
Spc	32.17	−25.73	2.03	14.09	−10.53	2.18	−5.48
Mm	\	\	\	\	\	\	\
Sr	30.88	−26.16	0.84	11.45	−9.95	2.18	−6.69
Sp	31.82	−26.04	1.26	12.19	−9.97	2.76	−6.48
Spc	32.17	−25.25	3.33	14.57	−9.98	2.96	−5.30
Stc	33.63	−25.81	3.41	15.35	−9.10	2.85	−6.37
Mm	\	\	\	\	\	\	\
Sr	32.88	−25.03	0.91	12.42	−11.91	2.24	−6.22
Sp	32.17	−25.99	1.69	13.52	−9.17	2.80	−5.39
Spc	32.69	−25.02	3.13	15.52	−9.10	2.96	−6.02
Stc	33.90	−25.56	3.39	16.69	−10.00	2.62	−6.13
Gm	31.96	−25.20	1.96	15.45	−9.86	2.44	−8.49

Fig. 19. The diagenetic heterogeneity of MB. **(a)** The vertical stacking sequence of lithofacies of MB. **(b)** Statistics of the intensity of diagenesis under the constraint of the sedimentary sequence of MB.

in each short period is higher than that of other lithofacies, and the development strength of lithofacies in contact with the silty mudstone interlayers increases significantly (Fig. 18(b)). The development strength of intercrystalline pores of clay minerals in BBt3 is overall weaker than that in BBt2. The cementation strength of carbonates is controlled by the relatively thick mudstone layer at the top, showing that except for Sr at the top and Gm at the bottom, the cementation strength of Sp in the upper part is also very high.

MB: Multiple short-period cycles and pure mudstone interlayers are developed in MB (Fig. 19(a)). The initial porosities of various lithofacies within MB have small differences, ranging from 30% to 34%, and the overall initial porosities of each short-period cycle decrease gradually from bottom to top (Fig. 19(b)). The compaction strengths of various lithofacies are similar, ranging from 25% to 29%, and the compaction strength of Sr within each short-period cycle is slightly higher. The development of microfractures in MB as a whole is better than that in BBt3, but worse than that in BBt1 and BBt2. The development strengths of microfractures in Stc and Spc in each short-period cycle are the highest, and gradually weaken as the grain size decreases (except for Gm). In terms of the dissolution strength, MB as a whole is close to BBt2, but lower than BBt1. The dissolution strengths of Stc and Spc in each short-period cycle are the highest, and the dissolution strength of lithofacies within each short-period cycle also weakens as the grain size decreases (except for Gm). In terms of the cementation strength of clay minerals, MB as a whole is slightly higher than BBt1 and BBt2, but lower than BBt3, and the cementation strength of lithofacies in contact with or close to the pure mudstone interlayers inside is relatively high (Fig. 19(b)). In terms of the intercrystalline pores of clay minerals, the development strengths of the middle and lower short-period cycles are higher than those of the upper part, and the development strength of Stc in each short-period cycle is higher than that of other lithofacies

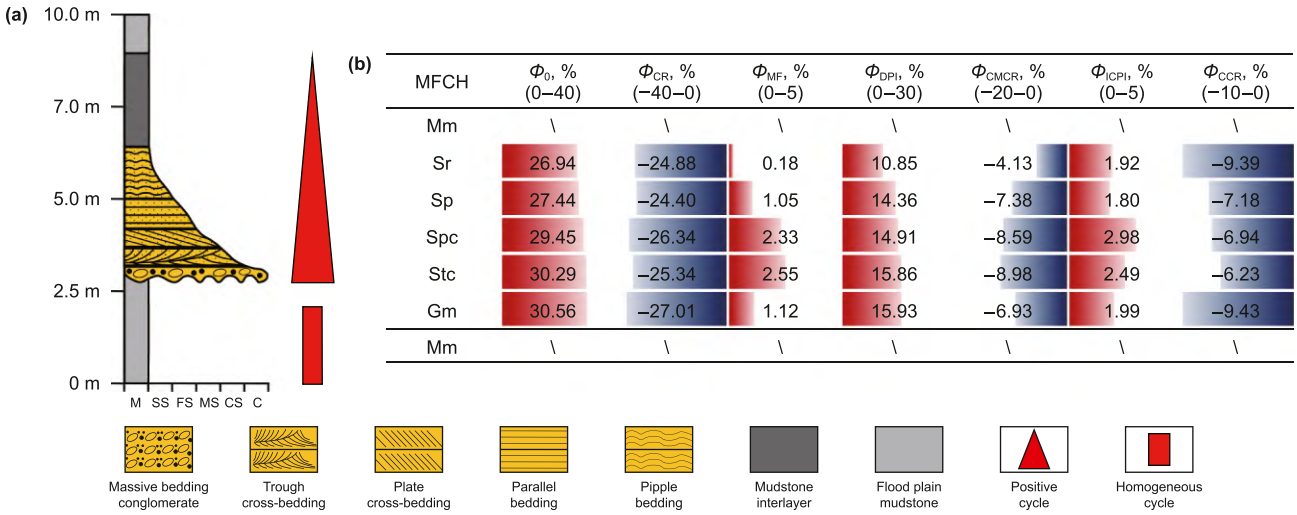

MFCH	Φ_0, % (0–40)	Φ_{CR}, % (−40–0)	Φ_{MF}, % (0–5)	Φ_{DPI}, % (0–30)	Φ_{CMCR}, % (−20–0)	Φ_{ICPI}, % (0–5)	Φ_{CCR}, % (−10–0)
Mm	\	\	\	\	\	\	\
Sr	26.94	−24.88	0.18	10.85	−4.13	1.92	−9.39
Sp	27.44	−24.40	1.05	14.36	−7.38	1.80	−7.18
Spc	29.45	−26.34	2.33	14.91	−8.59	2.98	−6.94
Stc	30.29	−25.34	2.55	15.86	−8.98	2.49	−6.23
Gm	30.56	−27.01	1.12	15.93	−6.93	1.99	−9.43
Mm	\	\	\	\	\	\	\

Fig. 20. The diagenetic heterogeneity of MFCH. **(a)** The vertical stacking sequence of lithofacies of MFCH. **(b)** Statistics of the intensity of diagenesis under the constraint of the sedimentary sequence of MFCH.

(Fig. 19(b)). The cementation strength of carbonates is controlled by both the position of lithofacies and the thickness of the pure mudstone interlayers, presenting the following characteristics: the cementation strengths of Sr at the top and Gm at the bottom are the highest; the cementation strength of carbonate lithofacies within each short-period cycle decreases as the distance from the pure mudstone interlayers increases (Fig. 19(b)); from bottom to top, as the thickness of the pure mudstone interlayers increases, the cementation strength of carbonate lithofacies within each short-period cycle increases significantly.

MFCH: Different from other architectural elements, thick mudstone is usually developed at the top and bottom of MFCH, and multi-stage cycles are not developed (Fig. 20(a)). Affected by the weak hydrodynamic force, the argillaceous content of the lithofacies within MFCH is relatively high, and the overall initial porosity is low. The overall dissolution strength and its variation pattern of MFCH are similar to those of other architectural elements. The overall development strength of microfractures, the cementation strength of clay minerals and the development strength of intercrystalline pores of clay minerals are all low, while the cementation strength of carbonates is high (Fig. 20(b)). Similar to other architectural elements, Stc and Spc in MCHF have higher dissolution strength, development strength of microfractures and development strength of intercrystalline pores of clay minerals compared with other lithofacies (Fig. 20(b)). The lithofacies in contact with or close to the thick mudstone at the top/bottom of MFCH have significantly higher cementation strength of carbonate minerals (Fig. 20(b)), showing that the carbonate cementation strengths of Sr at the top and Gm at the bottom are relatively the highest.

5. Discussion

5.1. Lithofacies and their genetic patterns

According to the analysis results of the diagenetic heterogeneity of each architectural element in the Shanxi Formation of the study area in Section 4.8.2, and with reference to previous studies, this study, based on the diagenetic evolution sequence, the current reservoir characteristics, the relative magnitudes of various diagenetic strengths (Figs. 16–20), and the effects on the reservoir, has further established the following five diagenetic facies: strong compaction diagenetic facies (DFc), strong dissolution + microfracture development diagenetic facies (DFdm), clay mineral intercrystalline pore-dominated diagenetic facies (DFcmip), strong carbonate cementation diagenetic facies (DFcc), and strong clay mineral cementation diagenetic facies (DFcmc). Meanwhile, the genetic patterns of various diagenetic facies have been discussed and summarized. The threshold values for classifying the diagenetic intensity of these five diagenetic facies are presented in Table 9.

5.1.1. Strong compaction diagenetic facies (DFc)

According to the statistical analysis in Section 4.8.2, the strong compaction diagenetic facies is mainly distributed in Sr in the middle/lower part of BBt1.

Characteristics: The strong compaction diagenetic facies show weak dissolution, underdeveloped microfractures and intercrystalline pores (Figs. 11 and 16(b)), well-developed sheet/curved sheet narrow throats and is very complex (Fig. 12), and has the

Table 9
Threshold values for classifying diagenetic intensity of different diagenetic facies.

Diagenetic facies	DFc	DFdm		DFcmip	DFcc	DFcmc
Classification basis	Φ_{CR}[a]	Φ_{DPI}[b]	Φ_{MFI}[c]	Φ_{ICPI}[d]	Φ_{CCR}[e]	Φ_{CMCR}[f]
Threshold values	< −28.32%	> 15.82%	> 3.31%	> 2.82%	< −5.50%	< −9.15%

[a] Φ_{CR} refers to porosity reduced due to compaction.
[b] Φ_{DPI} refers to porosity increases due to dissolution.
[c] Φ_{MFI} refers to porosity increased by microfractures due to fracturing.
[d] Φ_{ICPI} refers to porosity increases due to intercrystalline pores of clay minerals.
[e] Φ_{CCR} refers to porosity reduction due to cementation of carbonate minerals.
[f] Φ_{CMCR} refers to porosity reduction due to cementation of clay minerals.

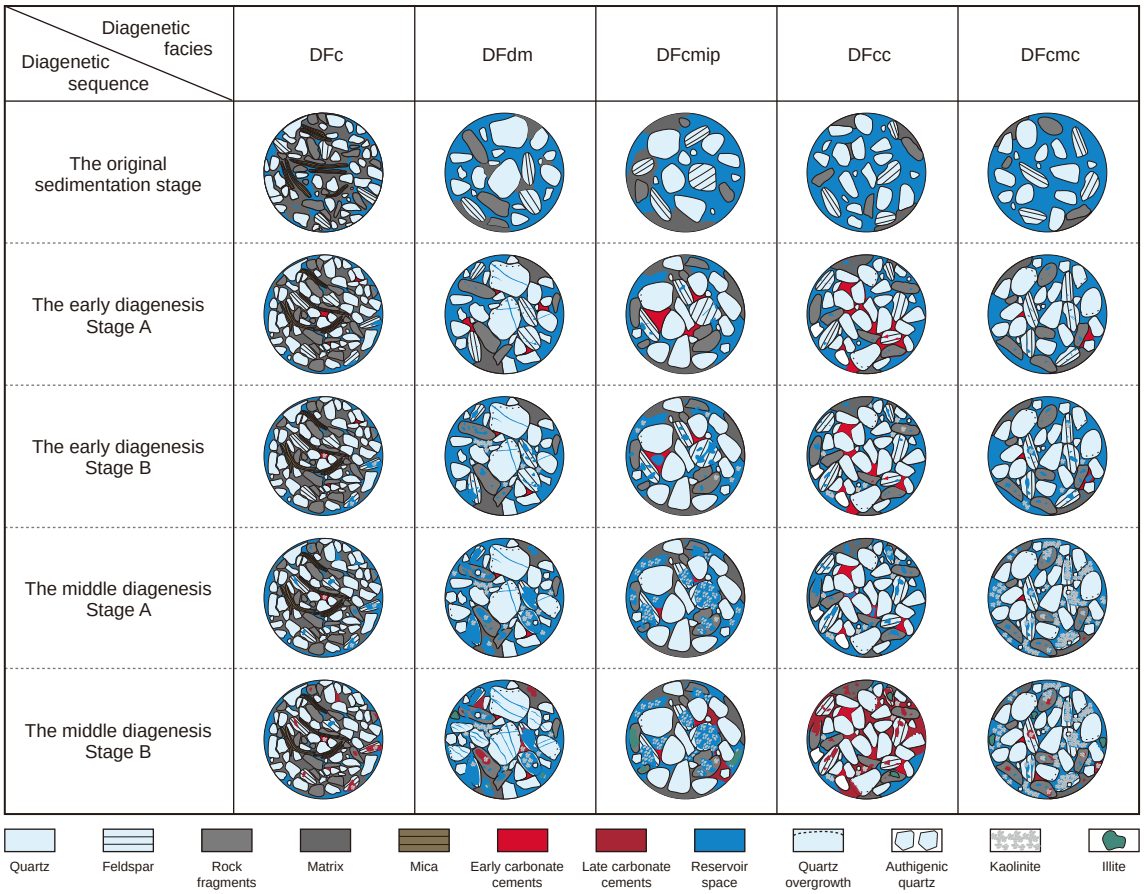

Fig. 21. Diagenetic evolution patterns of different diagenetic facies.

reservoir characteristics of low porosity, low permeability and low fluid mobility (Figs. 13 and 14).

Genetic explanation (Fig. 21): during the original sedimentary period, the content of plastic minerals and argillaceous matrix within this lithofacies is high, the grain size is small, the sorting and rounding are good, and the primary intergranular pores are relatively well-developed. In the early diagenetic stage A, the high content of argillaceous matrix weakens the dissolution of acidic meteoric water and the scouring of alkaline groundwater, resulting in only a small number of dissolved pores and early carbonate cements developed in the reservoir. Without the support of carbonate cements, strong compaction causes the deformation of plastic minerals and argillaceous matrix, which closely fills the spaces between detrital grains, thus causing a large number of primary intergranular pores to be destroyed. In the early diagenetic stage B, the acidic substances such as humic acid and fulvic acid discharged from the coal seam promote the further development of dissolved pores within the lithofacies. However, affected by the high content of argillaceous matrix, the development of dissolved pores is limited, and the cementation of clay minerals gradually begins to form. In the mesodiagenetic stage A, the injection of organic acids further increases the dissolved pores, and the early carbonate cements between some grains are dissolved. In the mesodiagenetic stage B, the organic acids are exhausted, the diagenetic environment turns alkaline, and the late carbonate cements fill the remaining intergranular pores and dissolved pores.

5.1.2. Strong dissolution + microfracture development diagenetic facies (DFdm)

According to the statistical analysis in Section 4.8.2, the strong dissolution + microfracture development diagenetic facies is mainly distributed in Stc and Spc of each architectural element.

Characteristics: The strong dissolution + microfracture development diagenetic facies shows well-developed dissolved pores (Stc and Spc in Figs. 11 and 16(b)–20(b)), well-developed microfractures (Stc and Spc in Figs. 11 and 16(b)–20(b)), well-developed neck-shaped wide throats (Fig. 12), and reservoir characteristics of high porosity, high permeability, and high fluid mobility (Figs. 13 and 14).

Genetic explanation (Fig. 21, taking Stc with coarse sandstone as an example): during the original sedimentary period, the content of rigid minerals within this lithofacies is high, the content of plastic minerals and argillaceous matrix is low, the grain size is large, the sorting and rounding are good, and the primary intergranular pores are very well-developed. In the early diagenetic stage A, under the action of the dissolution of acidic meteoric water and the scouring of alkaline groundwater, a small number of dissolved pores, secondary quartz overgrowths and early carbonate cements are developed in the reservoir. Under intense compaction, primary pores are severely destroyed, detrital grains are in point contact with each other, and microfractures are formed. In the early diagenetic stage B, acidic substances such as humic acid and fulvic acid discharged from the coal seam cause feldspar to further develop dissolved pores along the

microfractures. Meanwhile, the dissolved pores in the rock fragments also increase, part of the early carbonate cements are dissolved, and authigenic kaolinite begins to develop between the grains. In the mesodiagenetic stage A, the injection of organic acids further promotes the formation of dissolved pores, which further expand in feldspar along the microfractures (Hagar et al., 2020; Qin et al., 2022; Zhang et al., 2019). Natural gas injection displaces most of the ion-rich diagenetic fluid. The ions in the remaining diagenetic fluid combine with each other, and authigenic kaolinite and authigenic quartz are formed and fill the remaining intergranular pores and dissolved pores. In the mesodiagenetic stage B, kaolinite content did not increase further, attributed to the displacement of ion-rich diagenetic fluids by natural gas injection. During the late phase of this stage, the consumption of organic acids shifted the diagenetic environment toward alkalinity, triggering "embayed" dissolution of quartz. Concurrently, late-stage carbonate minerals cemented the remaining intergranular and dissolved pores. Additionally, kaolinite gradually transformed into illite with increasing burial depth (Sun et al., 2022).

5.1.3. Clay mineral intercrystalline pore-dominated diagenetic facies (DFcmip)

According to the statistical analysis in Section 4.8.2, the clay mineral intercrystalline pore—dominated diagenetic facies is mainly distributed in Spc and Sp of each architectural element.

Characteristics: The clay mineral intercrystalline pore-dominated diagenetic facies is composed of dissolved pores and intercrystalline pores (Spc and Sp in Figs. 11 and 16(b)–20(b)), and narrow bundled tubular throats are well-developed (Fig. 12), presenting the reservoir characteristics of high porosity, relatively low permeability, and relatively low fluid mobility (Figs. 13 and 14).

Genetic explanation (Fig. 21, taking Spc with medium—grained sandstone as an example): during the original sedimentary period, the content of rigid minerals within this lithofacies is relatively high, the content of plastic minerals and argillaceous matrix is relatively low, the grain size is relatively large, the sorting and rounding are poor, and the primary intergranular pores are relatively well-developed. In the early diagenetic stage A, affected by the dissolution of acidic meteoric water and the scouring of alkaline groundwater, a small number of dissolved pores, secondary quartz overgrowths, and early carbonate cements are developed in the reservoir (Bello et al., 2024). Under strong compaction, the detrital grains are in point contact and point line contact. The argillaceous matrix and early carbonate cements fill some of the pores, a large number of primary intergranular pores are destroyed, and microfractures are rarely developed or not developed at all. In the early diagenetic stage B, acidic substances such as humic acid and fulvic acid discharged from the coal seam cause the microfractures in feldspar to further develop dissolved pores. At the same time, rock fragments and early carbonate cements are further dissolved, authigenic kaolinite develops between the grains, and some rock fragments undergo kaolinite alteration. In the mesodiagenetic stage A, organic acid injection further promoted dissolved pore formation—these expanded along feldspar microfractures—while enhancing dissolution of early carbonate cements. Concurrently, natural gas displaced large volumes of ion-rich diagenetic fluid into the reservoir; ion recombination triggered massive authigenic kaolinite precipitation in residual intergranular and dissolved pores. Abundant, adequately sized pores enabled well-developed kaolinite crystal forms, generating numerous intercrystalline pores (Jiu et al., 2021; Yu et al., 2023). In the mesodiagenetic stage B, as the organic acids are consumed, the diagenetic environment transforms to an alkaline one, and "embayed" dissolution of quartz occurs. Late-stage carbonate cement gradually fills the remaining intergranular pores and dissolved pores. In addition, with the continuous increase of the burial depth, kaolinite transforms into illite, and authigenic illite is formed.

5.1.4. Strong carbonate cementation diagenetic facies (DFcc)

According to the statistical analysis in Section 4.8.2, the strong carbonate cementation diagenetic facies is mainly distributed in Sr at the top and Sp of each architectural element, Gm at the bottom, or Sr in contact with the pure mudstone interlayer.

Characteristics: The strong carbonate cementation diagenetic facies shows underdeveloped dissolved pores and remaining intergranular pores (Sr at the top and Sp of each architectural element, Gm at the bottom, or Sr in contact with the pure mudstone interlayer in Figs. 11 and 16(b)–20(b)) and is largely cemented by carbonate minerals (Sr at the top and Sp of each architectural element, Gm at the bottom, or Sr in contact with the pure mudstone interlayer in Fig. 16(b)–20(b)), with well-developed narrow neck-shaped, sheet/curved sheet throats (Fig. 12), and reservoir characteristics of relatively low porosity, low permeability, and relatively low fluid mobility (Figs. 13 and 14).

Genetic explanation (Fig. 21, taking Sp as an example): during the original sedimentary period, the content of rigid minerals within this lithofacies is relatively low, the content of plastic minerals is small, the content of argillaceous matrix is relatively high, the grain size is relatively small, the sorting and rounding are poor, and the primary intergranular pores are relatively well-developed. In the early diagenetic stage A, acidic meteoric water dissolution led to the development of a small number of dissolved pores and secondary quartz overgrowths in the reservoir. Meanwhile, alkaline groundwater scouring—coupled with CO_3^{2-} supply from compacted mudstone surrounding rock—promoted extensive early carbonate cementation, which filled most primary intergranular pores (Leila et al., 2019). Strong compaction further resulted in detrital grains forming point and point-line contact, destroying abundant primary intergranular pores with minimal microfracture development. In the early diagenetic stage B, acidic substances such as humic acid and fulvic acid discharged from the coal seam cause feldspar and rock fragments to further develop dissolved pores, and also dissolve a small amount of early carbonate cements. At this stage, authigenic kaolinite develops in the remaining intergranular pores, and some rock fragments undergo kaolinite alteration. In the mesodiagenetic stage A, the injection of organic acids further promotes the development of dissolved pores in feldspar and rock fragments, and also further dissolves the early carbonate cements. However, due to the high content of argillaceous matrix in the lithofacies hindering the injection of acidic substances, the dissolution is relatively weak. In the mesodiagenetic stage B, as the organic acids are exhausted, the diagenetic environment transforms to an alkaline one, and "embayed" dissolution occurs in some quartz (Alameen et al., 2024). With the increase of burial depth, the mudstone surrounding rock continuously provides a large amount of CO_3^{2-}, resulting in a large amount of late-stage carbonate minerals cementing the remaining intergranular pores and dissolved pores. At the same time, kaolinite transforms into illite, and authigenic illite is formed.

5.1.5. Strong clay mineral cementation diagenetic facies (DFcmc)

According to the statistical analysis in Section 4.8.2, the strong clay mineral cementation diagenetic facies is mainly distributed in Sp and Sr of the architectural elements with silty mudstone interlayers (Figs. 16–18).

Characteristics: The strong clay mineral cementation diagenetic facies shows the development of remaining intergranular pores and dissolved pores (Sp and Sr in Figs. 11 and 16(b)–18(b)). Most of the pore space is filled with adsorptive clay minerals, narrow bundled tubular throats are well-developed, and it exhibits reservoir characteristics of relatively low porosity, low permeability, and low fluid mobility (Figs. 13 and 14). These diagenetic characteristics are similar to those of the basement sandstones in the Cachiri Group of the Cesar Sub-basin (Colombia) (Ortiz-Orduz et al., 2021).

Genetic explanation (taking Sp as an example in Fig. 21): During the original sedimentary period, the content of rigid minerals within this lithofacies is relatively high, the content of plastic minerals is low, the content of argillaceous matrix is relatively high, the grain size is small, the sorting and rounding are poor, and the remaining intergranular pores are relatively well-developed. In the early diagenetic stage A, under the dissolution of acidic meteoric water and the scouring of alkaline groundwater, a small number of dissolved pores, secondary quartz overgrowths, and early carbonate cements are developed in the reservoir. Strong compaction and the development of argillaceous matrix cause the detrital grains to be in point contact and point-line contact, a large number of primary intergranular pores are destroyed, and microfractures are hardly developed. In the early diagenetic stage B, acidic substances such as humic acid and fulvic acid discharged from the coal seam cause the microfractures in feldspar to further develop into dissolved pores, and also cause the rock fragments to further develop dissolved pores. Some early carbonate cements are dissolved, and authigenic kaolinite develops in the remaining intergranular pores and dissolved pores. In the mesodiagenetic stage A, organic acid injection increased dissolved pores and further dissolved early carbonate cements. Blocked by interlayers, large volumes of natural gas-displaced diagenetic fluid entered this lithofacies; its rich ions combined to form authigenic kaolinite, which precipitated in residual intergranular and dissolved pores. However, insufficiently abundant and sized pores resulted in poorly developed kaolinite crystal forms, precluding extensive intercrystalline pore formation (Meng et al., 2023). In the mesodiagenetic stage B, kaolinite further develops and transforms into illite as the burial depth increases. In addition, as the diagenetic environment transitions to an alkaline one, “embayed” dissolution of quartz occurs, and late-stage carbonate minerals cement the remaining intergranular pores and dissolved pores.

5.2. Heterogeneous diagenetic patterns of sandbody architectural elements and their genesis

By analyzing the diagenetic heterogeneity characteristics of the architectural elements in Section 4.8.2 and the genetic patterns of the diagenetic facies in Section 5.1, it can be seen that the diagenetic strengths of the same lithofacies vary in different architectural elements and at different positions within them. That is, the same lithofacies may exhibit different diagenetic facies within the sandbody architecture (Heidsiek et al., 2020; Moraes, 1991). Such heterogeneous diagenetic phenomena are common in fluvial tight sandstone reservoirs; for instance, similar diagenetic heterogeneity is also observed in the Juwayl Member of the Wajid Sandstone in southwest Saudi Arabia (Mahgoub and Abdullatif, 2020). Therefore, based on the diagenetic facies and their genetic mechanisms, heterogeneous diagenetic patterns of sandbody architecture in braided and meandering river facies reservoirs were established, and their genetic origins were analyzed.

5.2.1. Heterogeneous diagenetic patterns and genesis of architectural elements of braided river sandbody

Per Section 4.2, braided river sandbodies exhibit distinct architectural elements with varying sedimentary and diagenetic heterogeneity (Figs. 4–5, Table 6, and Figs. 16–18). These elements differ both perpendicular and parallel to the provenance direction, leading to spatially heterogeneous diagenetic patterns within the sandbody architecture (Figs. 22–23).

a. Heterogeneous diagenetic pattern of the profile perpendicular to the provenance

The profile perpendicular to the provenance of the braided river sedimentary sandbody (Fig. 4(b)) contains two types of architectural elements, namely BBt1 and BBt2. There are certain similarities and differences in the genesis and distribution patterns of the diagenetic facies of the lithofacies within them.

The heterogeneous diagenetic pattern of BBt1 (Fig. 22(c)) is as follows: The Gm at the bottom is in contact with the mudstone. Under the weakly alkaline environment in the late stage of mesodiagenesis B, a large amount of CO_3^{2-} migrating from the adjacent mudstone (floodplain mud in the previous sedimentary period) combines with Ca^{2+}, Fe^{2+}, and Mg^{2+} in the diagenetic fluid to form a large amount of carbonate cement, which, together with clay minerals, fills the dissolved pores, ultimately presenting the strong carbonate cementation diagenetic facies (DFcc). The Sr at the top belongs to the DFcc. Its genesis is also attributed to the substantial amount of CO_3^{2-} supplied by the adjacent mudstone (the overlying mudstone), which results in the formation of a large quantity of carbonate cement. The Stc and Spc in the lower, middle and upper parts are all of the strong dissolution + microfracture development diagenetic facies (DFdm), and their genesis is as follows: In the early diagenetic stage A, strong compaction causes the grains of the lithofacies with low argillaceous content, relatively large detrital grain size and relatively good sorting/rounding to be mainly in point contact, making the detrital grains more prone to cracking. Especially for Stc, the original arrangement of its minerals is relatively chaotic, and there are relatively more point contacts, resulting in more developed microfractures. In the mesodiagenetic stage B, the development of microfractures in Stc and Spc provides favorable channels for the injection of organic acids, leading to the massive dissolution of feldspar, early chlorite and volcanic materials, and the appearance of more dissolved pores. Since there are no internal silty interlayers around these lithofacies, the ion-rich diagenetic fluid is fully displaced, making it difficult for clay minerals to form in-situ precipitation. And in the late stage of diagenesis, the microfractures generated by fracturing will be further developed in the absence of support between the grains. In addition, Stc and Spc are relatively far from the top and bottom mudstones. After the CO_3^{2-} discharged from the mudstones is consumed by Gm and Sr, only a small part of it enters Stc and Spc, resulting in relatively weak carbonate cementation in these two. The Sp in the lower, middle and upper parts are all of the clay mineral intercrystalline pore-dominated diagenetic facies (DFcmip). Its genesis is as follows: In the early stage of the mesodiagenetic stage B, the injection of organic acids dissolves feldspar, early chlorite and volcanic materials, forming a certain number of dissolved pores, which provides favorable conditions for the precipitation of clay minerals formed by the Al^{3+} and K^{+} rich in the diagenetic fluid. However, different from Stc and Spc, the original sedimentary hydrodynamic force of Sp is relatively weak, and the sorting/rounding of detrital grains is relatively good. The strong compaction in the early diagenetic stage A fails to lead to the massive development of microfractures. Thus, after the injection of natural gas, the fluidity of the internal diagenetic fluid is

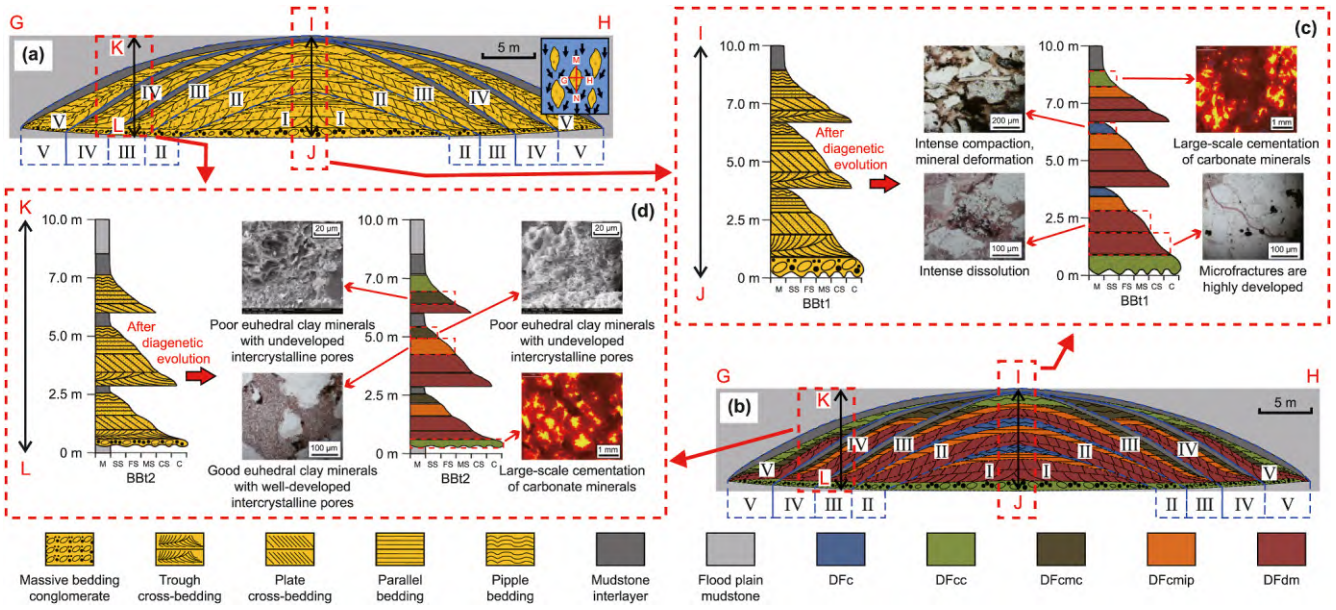

Fig. 22. Heterogeneous diagenetic pattern of the architectural elements in the provenance - cutting direction section of braided river sand bodies. **(a)** Provenance - cutting section of braided river sand bodies. **(b)** Distribution of diagenetic facies in the provenance - cutting section of braided river sand bodies. **(c)** BBt1 diagenetic pattern. **(d)** BBt2 diagenetic pattern.

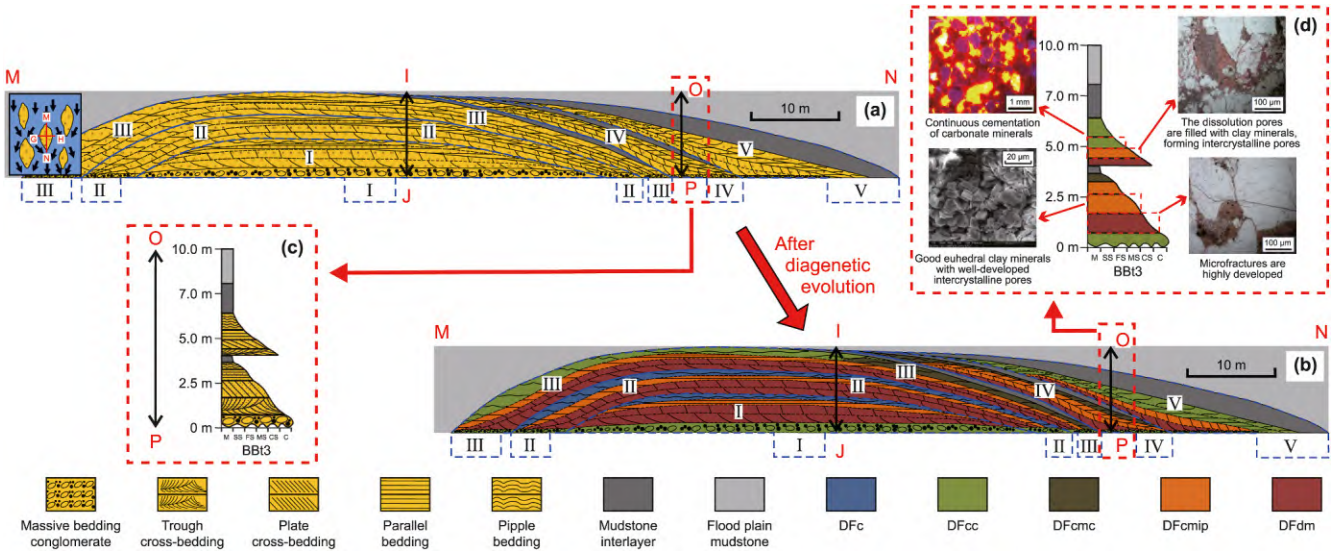

Fig. 23. Heterogeneous diagenetic pattern of the architectural elements in the provenance - parallel direction section of braided river sand bodies. **(a)** Provenance - parallel section of braided river sand bodies. **(b)** Distribution of diagenetic facies in the provenance - parallel section of braided river sand bodies. **(c)** BBt3 diagenetic pattern.

relatively poor, resulting in the in-situ precipitation of clay minerals in the early stage of the mesodiagenetic stage B. The development of intercrystalline pores of clay minerals in Sp benefits from the weak sedimentary structural heterogeneity of sandstone-dominated BBt1, which provides channels for organic acids to enter relatively easily, leading to the formation of a large number of large dissolved pores, providing sufficient space for the crystallization and growth of clay minerals. As a result, clay minerals exhibit good crystal forms and form intercrystalline pores, which also provides favorable conditions for the occurrence of natural gas. The Sr in the lower and middle parts are of the strong compaction diagenetic facies (DFc). According to the analysis of the top Sr, the compaction is strong and the content of argillaceous matrix is high, which causes the argillaceous matrix to fill the remaining intergranular pores, making the injection of organic acids relatively difficult, resulting in fewer developed dissolved pores, limited injection of natural gas, and a low content of clay minerals (Fig. 16(b)) (Henares et al., 2016). Different from the top Sr, the Sr in the lower and middle parts are relatively far from the mudstone, and the content of CO_3^{2-} provided by the mudstone is relatively low, so there is less carbonate cement.

The heterogeneous diagenetic pattern of BBt2 (Fig. 22(d)) has similarities with that of BBt1, which are reflected in the fact that the genesis of the top/bottom Gm and Sr being of DFcc is similar to that of BBt1 (Fig. 22(c) and (d)); the genesis of the lower and middle Stc and Spc, and the upper Spc being of DFdm is similar to that of BBt1 (Fig. 22(c) and (d)); and the genesis of the middle and lower Sp being of DFcmip is similar to that of BBt1 (Fig. 22(c) and (d)). However, the presence of silty mudstone interlayers within BBt2 makes the lithofacies in contact with and

close to these interlayers exhibit diagenetic facies distribution characteristics different from those of BBt1. The upper Sp in BBt2 shows the strong clay mineral cementation diagenetic facies (DFcmc), rather than DFcmip (Fig. 22(c) and (d)); the middle and lower Sr in BBt2 show DFcmc, rather than DFc (Fig. 22(c) and (d)). These differences are mainly caused by the shielding effect of the silty mudstone interlayers. The diagenetic fluid displaced by natural gas injection in Gm, Stc and Spc enriches in the lithofacies close to and in contact with the silty mudstone interlayers, forming a large amount of clay mineral precipitation. Therefore, for the middle and lower Sp with strong dissolution, due to the weak shielding effect of the silty mudstone interlayers on the injection of organic acids, the dissolved pores provide sufficient space for a large amount of enriched clay minerals to form good crystal forms, thus developing intercrystalline pores and being of DFcmip. For the upper Sp, blocked by the middle/lower silty mudstone interlayers, the entry of organic acids is hindered, resulting in weak dissolution. As a result, large-sized dissolved pores are underdeveloped, and a large amount of diagenetic fluid ions displaced by natural gas within it develop into clay minerals with poor crystal forms and without the formation of intercrystalline pores, ultimately becoming DFcmc. Similarly, the genesis of the lower and middle Sr developing into DFcmc is the same as that of the upper Sp. That is, the shielding of the nearby silty mudstone interlayers leads to a large amount of in-situ precipitation and crystallization of diagenetic ions, developing into clay minerals with poor crystal forms and without the formation of intercrystalline pores (Morad et al., 2010).

b. Heterogeneous diagenetic pattern of the profile along the provenance

The architectural pattern of the braided river sedimentary sandbody along the provenance profile (Fig. 4(c)) includes two types of architectural element patterns, namely BBt1 and BBt3. Among them, the heterogeneous diagenetic pattern of BBt1 along the provenance and its genesis are consistent with those along the direction perpendicular to the provenance. The heterogeneous diagenetic pattern of BBt3 (Fig. 23(c)) is as follows: The genesis of the lower and middle Stc being of DFdm is consistent with that of BBt2 and BBt1 (Figs. 22(c)–(d) and 23(d)). Except that the top/bottom Gm and Sr are of DFcc, the upper Sp of BBt3 is also of DFcc (Figs. 22(c)–(d) and 23(d)). Its genesis is that the thickness of the top mudstone (floodplain mud) is large, which can provide more CO_3^{2-}. The carbonate cement formed in Sr cannot completely consume CO_3^{2-}, resulting in the Sp close to the thick mudstone also being of DFcc. Moreover, the dissolution of the top Sr and the upper Sp is weak, and the microfractures are underdeveloped, and the intercrystalline pores of clay minerals are poorly developed (Fig. 18(b)). The upper and lower Spc are of DFcmip, rather than DFdm. Its genesis is that the sedimentary hydrodynamic force of Spc in BBt3 is weaker than that in BBt1 and BBt2, resulting in a relatively high argillaceous content, poor sorting and rounding, so the development of microfractures caused by fracturing is relatively few (Fig. 18(b)). The ions in a large amount of diagenetic fluid laterally shielded by the silty mudstone interlayer precipitate and crystallize in the large-sized dissolved pores inside the upper and lower Spc, forming intercrystalline pores. In particular, the diagenetic characteristics of lithofacies under the shielding effect of intra-sandbody silty mudstone interlayers are similar to those of the sandy braided fluvial sedimentary reservoirs in the Lower Solling Formation of the Reinhardswald Basin (Weber and Ricken, 2005).

5.2.2. Heterogeneous diagenetic patterns and genesis of architectural elements of meandering river sandbody

Per Section 4.2, meandering river sandbodies develop distinct architectural elements across spatial positions, with varying sedimentary and diagenetic heterogeneity (Fig. 6, Table 7, Figs. 19 and 20). Unlike braided rivers, meandering river sandbody architectures show similar lithofacies distributions in profiles both perpendicular and parallel to the provenance (Fig. 5(b)). Moreover, under the control of sedimentary and diagenetic heterogeneity, their internal architecture exhibits heterogeneous diagenetic patterns along these directions (Fig. 24), encompassing two architectural elements: MB and MFCH.

The heterogeneous diagenetic pattern of MB and its genesis have similarities with those of BBt2, which are reflected in the following aspects: the genesis of the top/bottom Gm and Sr being of DFcc (Figs. 22 and 24(c)); the genesis of the lower and middle Stc and the lower Spc being of DFdm (Figs. 22 and 24(c)); and the genesis of the middle and lower Sp being of DFcmip (Figs. 22 and 24(c)). In addition, the internal pure mudstone interlayer not only has a shielding effect on the diagenetic fluid, but also has a carbonate cementation effect on the lithofacies in contact with and close to it. This leads to different diagenetic facies in the lithofacies in contact with and close to the pure mudstone interlayer compared with BBt2, specifically as follows: The Sr in the middle of MB is of DFcc, rather than DFcmc (Fig. 22(d) and 24(c)). The genesis is that the pure mudstone interlayer in the middle transports CO_3^{2-} to Sr, resulting in strong early carbonate cementation. At the same time, the high content of argillaceous matrix in the middle Sr itself and the shielding of the pure mudstone interlayer below make the injection of organic acids difficult, the dissolution intensity is relatively weak, and the development of dissolved pores is relatively weak. As a result, the diagenetic fluid displaced by the injection of natural gas is difficult to enter, and the clay mineral cementation is also relatively weak (Fig. 19(b)), ultimately developing into DFcc. The Sp in the middle of MB is of DFcmc, rather than DFcmip (Fig. 22d and 24(c)). The genesis is that the large amount of carbonate cementation developed in the middle Sr in the early stage makes the diagenetic fluid displaced by the injection of natural gas unable to enrich in Sr, and it can only enrich in Spc and Sp. Among them, since Sp is closer to the pure mudstone interlayer, the content of early carbonate cements is also higher (Fig. 19(b)), and its relatively high argillaceous content, poor sorting and rounding lead to the underdevelopment of large-sized dissolved pores and microfractures under the limited dissolution of organic acids (Fig. 19(b)). The clay minerals that are abundantly enriched and precipitated cannot form intercrystalline pores, ultimately developing into DFcmc. The Spc in the middle of MB is of DFcmip, rather than DFdm (Fig. 22(d) and 24(c)). The genesis is that, different from Sp, Spc is farther from the pure mudstone, and the content of early carbonate cements is relatively low (Fig. 19(b)). Its organic acid dissolution is more sufficient, and relatively more large-sized dissolved pores and microfractures are developed. A large amount of clay minerals that are enriched and precipitated can form intercrystalline pores, so it develops into DFcmip. The genesis of the upper Stc being of DFcmip, rather than DFdm, is consistent with that of the middle Stc. The genesis of the upper Sp being of DFcmc is consistent with that of the upper Sp of BBt2.

The difference between MFCH and other architectural elements lies in its weaker sedimentary hydrodynamic environment, with its top and bottom wrapped by thick mudstone. The thick mudstone at the top and bottom transports a large amount of CO_3^{2-} to the top Sr, the thin-layer Gm at the bottom, and the lower Stc,

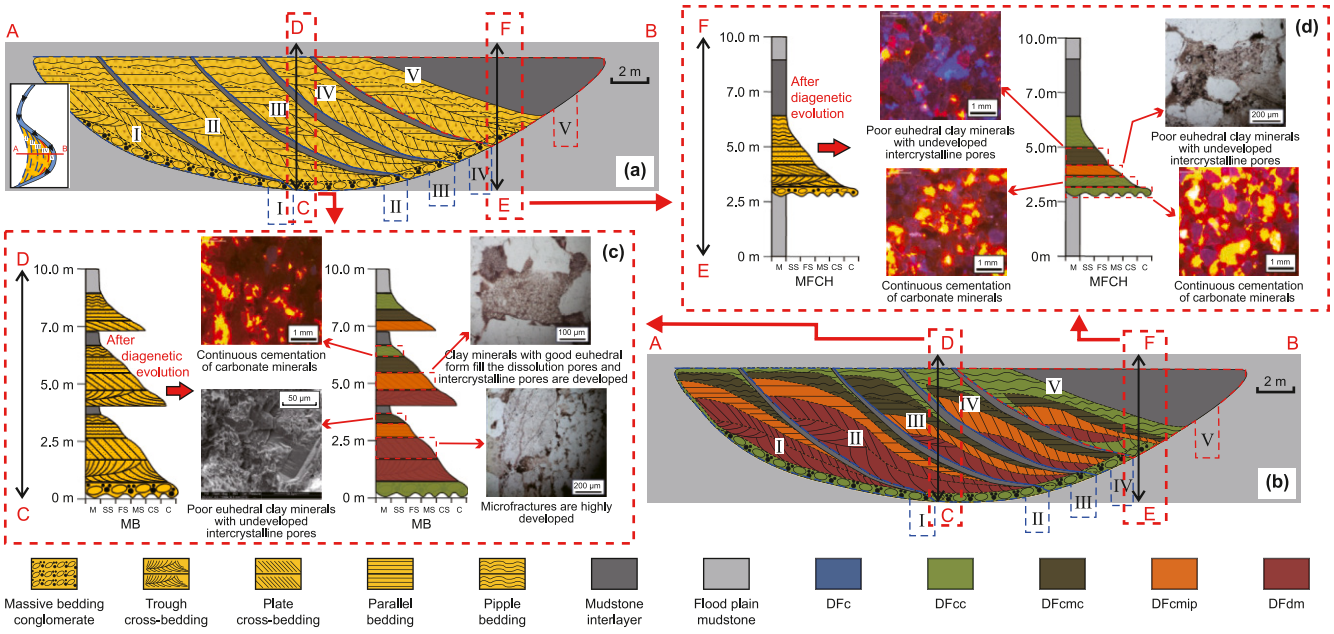

Fig. 24. Heterogeneous diagenetic pattern of the architectural elements in the provenance - cutting direction section of meandering river sand bodies. **(a)** Provenance - cutting section of meandering river sand bodies. **(b)** Distribution of diagenetic facies in the provenance - cutting section of meandering river sand bodies. **(c)** MB diagenetic pattern. **(d)** MFCH diagenetic pattern.

resulting in strong carbonate mineral cementation in these lithofacies and the development of DFcc (Fig. 24(b), (d)). Referring to the heterogeneous diagenetic pattern and its genesis of BBt1, the top Sr, the thin-layer Gm at the bottom, and the lower Stc are all of DFcc (Figs. 23(c) and 24(d)). The reasons for Spc being of DFcmip and Sp being of DFcmc are consistent with those of Spc and Sp in the middle of MB. It should be noted that for the meandering river sedimentary sandbody dominated by lateral accretion, due to the control of the internal pure mudstone interlayer, it shows different changes in the heterogeneous diagenetic pattern compared with the sedimentary sandbody in the braided river channel dominated by vertical accretion. For the meandering river sedimentary sandbody, with the progress of sedimentary stages, the internal pure mudstone interlayer gradually thickens, and the intensity of transporting CO_3^{2-} to the adjacent lithofacies gradually increases, leading to the following changes: Sr gradually changes from mostly DFcmc and a small part of DFcc to a small part of DFcmc and mostly DFcc, and finally completely changes to DFcc (Fig. 24(b)); Sp gradually changes from DFcmip to DFcmc, and then partly changes to DFcc (Fig. 24(b)); Spc gradually changes from strong DFdm to DFcmip, and finally changes to DFcmc (Fig. 24(b)); the Stc of MB is always of DFdm (Fig. 24(b)), but a small part of Stc in MFCH changes to DFcc (Fig. 24(b)).

5.3. The control of sedimentary and diagenetic heterogeneity on reservoir quality

Based on the discussion of the genesis and patterns of diagenetic facies and heterogeneous diagenetically of the sandstone reservoirs in the Shanxi Formation of the study area, combined with the reservoir spaces, reservoir qualities, sedimentary and diagenetic heterogeneities of the architectural elements of the target layer sandstone reservoirs, this section further discusses the control of diagenesis and sedimentation on reservoir quality, and establishes the distribution pattern of reservoir quality heterogeneities of the architectural elements.

5.3.1. The control of diagenesis on reservoir quality

According to the correlation between the diagenetic intensity and the reservoir quality parameters shown in Fig. 25, as well as the effect of diagenesis on the reservoir quality, diagenesis can be classified into constructive and destructive types, which are specifically as follows.

a. Constructive Diagenesis

According to the positive correlation between diagenetic intensity, reservoir physical properties and fluid mobility, dissolved pores formed by dissolution (Φ_{DPI}), microfractures formed by fracturing (Φ_{MFI}) and intercrystalline pores of clay mineral cement (Φ_{ICPI}) are classified as constructive diagenesis. Φ_{DPI} is positively correlated with both Por_Core and Perm_Core (Fig. 25(a), (d)), and negatively correlated with Swi_Core (Fig. 25(g)). This indicates that the development of dissolved pores by dissolution is beneficial for improving the physical properties and fluid mobility of the reservoir. Φ_{MFI} is positively correlated with both Por_Core and Perm_Core (Fig. 25(b), (e)), and negatively correlated with Swi_Core (the heatmap in Fig. 25). Φ_{MFI} has an exponential correlation with Perm_Core, and the correlation coefficient is greater than 0.6. This shows that the development of microfractures formed by fracturing is beneficial for improving the physical properties and fluid mobility of the reservoir, and it makes a particularly significant contribution to the increase in permeability. Φ_{ICPI} is positively correlated with both Por_Core and Swi_Core, and has an unclear correlation with Perm_Core (the heatmap in Fig. 25). Φ_{ICPI} has an exponential correlation with Por_Core (Fig. 25(c)), indicating that the development of intercrystalline pores of clay mineral cement makes a particularly significant contribution to the increase in porosity. Φ_{ICPI} has a positive correlation first and then a negative correlation with Perm_Core (Fig. 25(f)). This indicates that the development of a certain content of intercrystalline pores of clay mineral cement contributes to the increase in permeability, but excessive development will divide the large pore throats (Figs. 7(b)

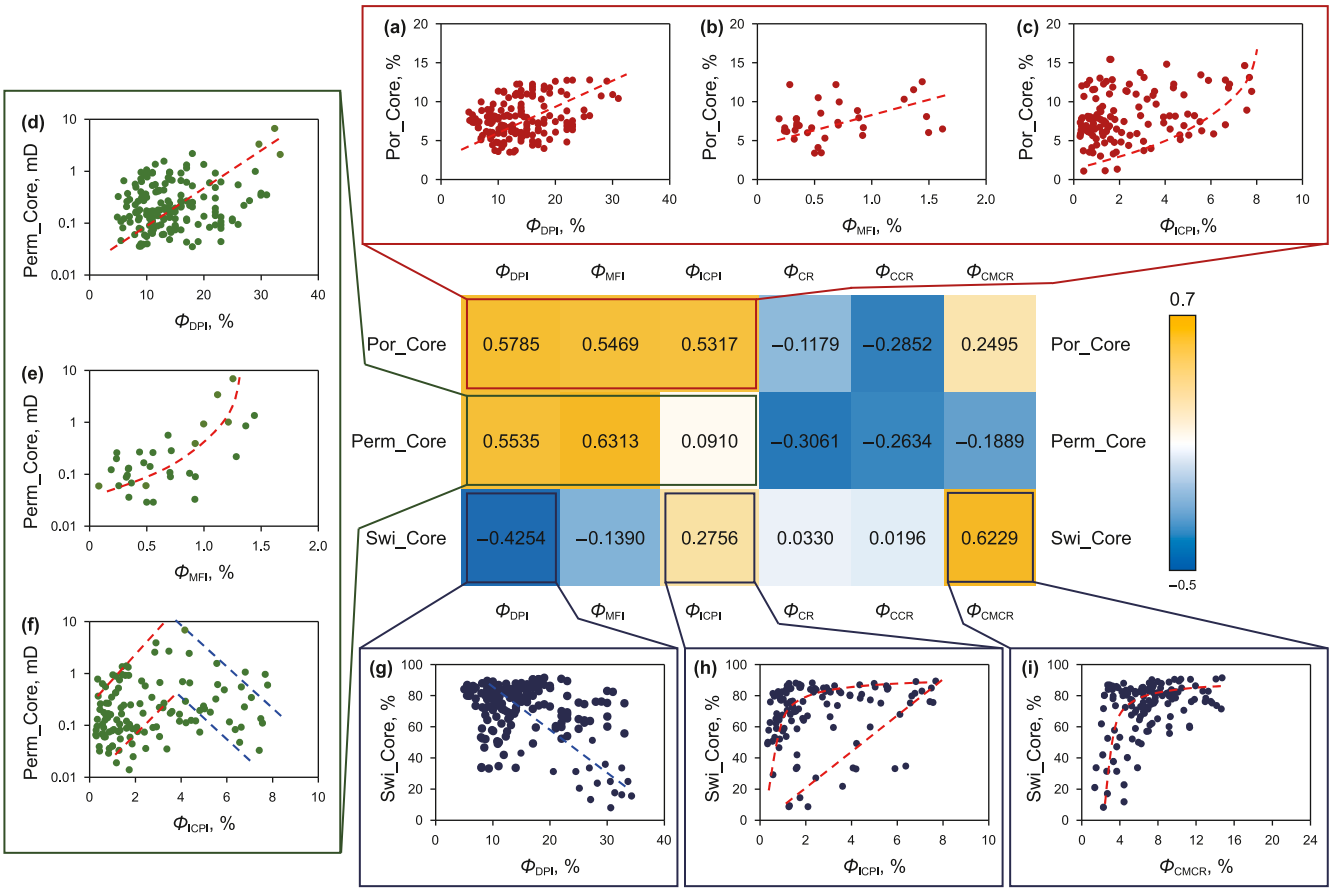

Fig. 25. Heatmap of correlation coefficients for Φ_{DPI}, Φ_{MFI}, Φ_{ICPI}, Φ_{CR}, Φ_{CCR}, and Φ_{CMCR} with Por_Core, Perm_Core, and Swi_Core. **(a)** The correlation plot of Φ_{DPI} with Por_Core. **(b)** The correlation plot of Φ_{MFI} with Por_Core. **(c)** The correlation plot of Φ_{ICPI} with Perm_Core. **(d)** The correlation plot of Φ_{DPI} with Perm_Core. **(e)** The correlation plot of Φ_{MFI} with Perm_Core. **(f)** The correlation plot of Φ_{ICPI} with Perm_Core. **(g)** The correlation plot of Φ_{DPI} with Swi_Core. **(h)** The correlation plot of Φ_{ICPI} with Swi_Core. **(i)** The correlation plot of Φ_{CMCR} with Swi_Core.

and 8(a)), resulting in a decrease in permeability. Φ_{ICPI} has two forms of positive correlation with Swi_Core (Fig. 25(h)). The positive correlation is because the development of intercrystalline pores of clay mineral cement also represents the development of clay minerals, and clay minerals have adsorptivity. The existence of two forms may be due to the differences in the types and occurrences of clay minerals (Zhou et al., 2021). The development of intercrystalline pores of loose "booklet-shaped" kaolinite with relatively weak adsorptivity (Fig. 7(c)) contributes to the improvement of Swi_Core mainly due to its adsorptivity, showing a linear correlation; the development of intercrystalline pores of honeycomb-shaped mixed illite/smectite with relatively strong adsorptivity contributes to the improvement of Swi_Core not only due to its adsorptivity, but also due to the occurrence of the honeycomb shape (Fig. 7(f)), which strongly divides the pore throats, increases the complexity of the pore throats, and thus improves the adsorptivity of the pore throats to formation water (Molenaar and Felder, 2018; Wang et al., 2025).

In summary, dissolved pores formed by dissolution and microfractures formed by fracturing are absolutely constructive diagenesis, and intercrystalline pores of clay mineral cement are relatively constructive diagenesis.

b. Destructive diagenesis

According to the negative correlation between the diagenetic intensity, reservoir physical properties and fluid mobility, compaction (Φ_{CR}), carbonate mineral cementation (Φ_{CCR}) and clay mineral cementation (Φ_{CMCR}) are classified as destructive diagenesis. Φ_{CR} and Φ_{CCR} are negatively correlated with Por_Core and Perm_Core, and negatively correlated with Swi_Core (the heatmap in Fig. 25). This indicates that both compaction and carbonate mineral cementation are not conducive to the improvement of reservoir physical properties and fluid mobility, but the small correlation coefficient shows that their controlling effect is not strong. It should be noted that Φ_{CMCR} is positively correlated with Por_Core, negatively correlated with Perm_Core (the heatmap in Fig. 25), and logarithmically positively correlated with Swi_Core (Fig. 25(i)). The positive correlation between Φ_{CMCR} and Por_Core is due to the development of clay mineral cementation, which also represents the development of intercrystalline pores of clay minerals, and the development of intercrystalline pores of clay minerals contributes greatly to the improvement of reservoir porosity (Fig. 25(c)). The logarithmic positive correlation between Φ_{CMCR} and Swi_Core may be because the intercrystalline pores of clay minerals such as "vermicular" kaolinite, sheet-like illite and fibrous illite are poorly developed. Their strong adsorptivity and the ability of "vermicular", sheet-like and fibrous occurrences to divide pore throats are relatively strong. Therefore, they still have a high irreducible water saturation at a low content (Zhang et al., 2020).

5.3.2. The control of sedimentary heterogeneity on reservoir quality

According to the analyses in Section 4.8, Section 5.2 and Section 5.3.2, sedimentary heterogeneity controls the heterogeneous

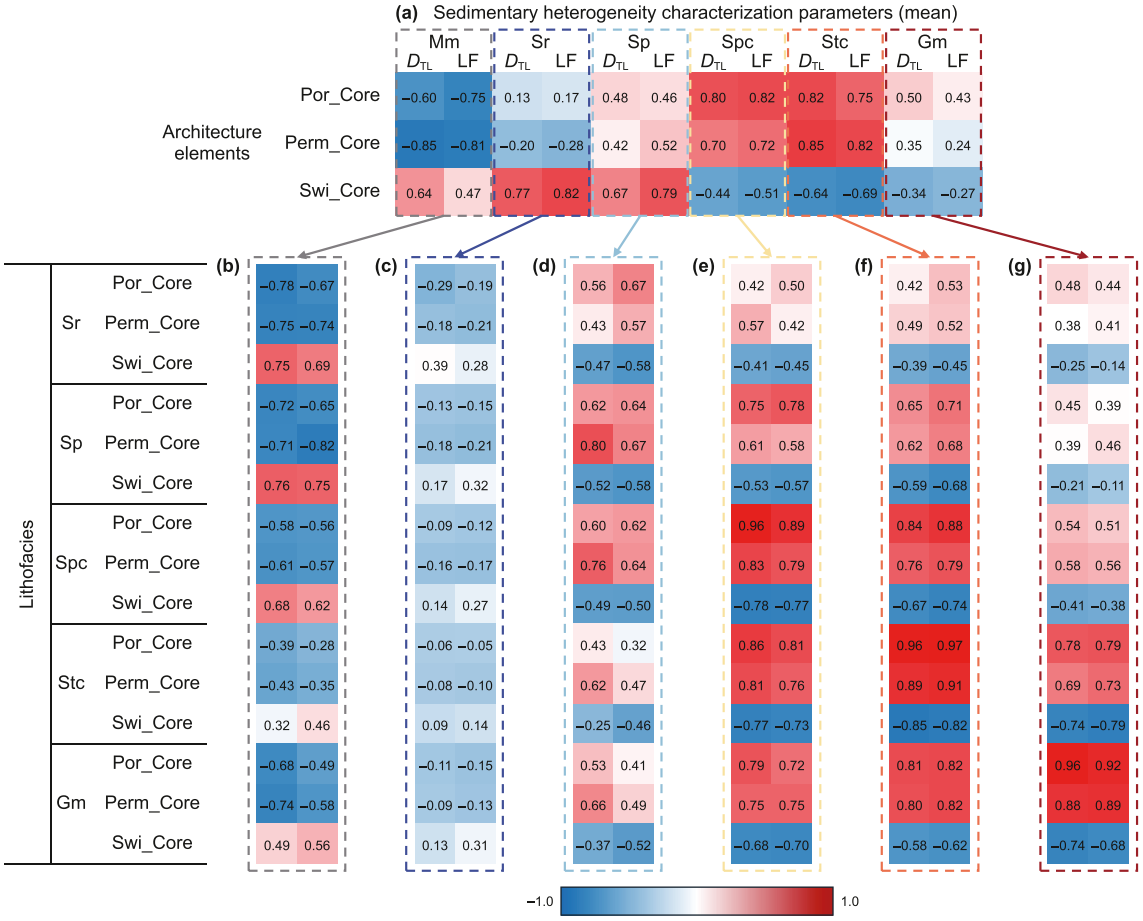

Fig. 26. Heatmap of the correlation coefficients between the mean values of D_{TL} and LF for each lithofacies and the mean values of Por_Core, Perm_Core, and Swi_Core of each architectural element and lithofacies. **(a)** Heatmap of the correlation coefficients between the mean values of D_{TL} and LF for each lithofacies and the mean values of Por_Core, Perm_Core, and Swi_Core for each architectural element. **(b)**–**(g)** are heatmaps of the correlation coefficients between the mean values of D_{TL} and LF for different lithofacies and the mean values of Por_Core, Perm_Core, and Swi_Core for each sandstone lithofacies. **(b)** Mm; **(c)** Sr; **(d)** Sp; **(e)** Spc; **(f)** Stc; **(g)** Gm.

diagenetic pattern of the architectural elements of the sandbody, and diagenesis has different control effects on the reservoir quality. Based on the above analyses, this study further establishes the following correlations with lithofacies and architectural elements as units respectively: a. The correlation between the sedimentary heterogeneity characterization parameters of lithofacies and the reservoir quality parameters of the overall architectural elements (Fig. 26(a), the relationship between the mean values of the total lithofacies density and lithofacies frequency of each lithofacies and the mean values of Por_Core, Perm_Core, and Swi_Core of the architectural elements to which they belong; b. The correlation between the sedimentary heterogeneity characterization parameters of lithofacies and the reservoir quality parameters of the corresponding lithofacies (Fig. 26(b)–(g), the relationship between the mean values of the total lithofacies density and lithofacies frequency of each lithofacies and the mean values of Por_Core, Perm_Core, and Swi_Core of the corresponding lithofacies). The specific correlation characteristics and genesis are as follows:

The mean D_{TL} and mean LF of Stc and Spc are positively correlated with the mean Por_Core and Perm_Core of the architectural elements and various sandstone lithofacies with a high coefficient (Fig. 26(a), (e), and (f)), and negatively correlated with the mean Swi_Core of the architectural elements and various sandstone lithofacies with a high coefficient (Fig. 26(a), (e), and (f)). This indicates that the development of Stc and Spc not only helps to improve the reservoir quality of the overall architectural elements, but also promotes the improvement of the reservoir quality of other lithofacies. The reason is that the reservoir quality of Stc and Spc is relatively good (Figs. 13–15), constructive diagenesis is well-developed (Figs. 16–20), the diagenetic facies are mostly DFdm and DFcmip, and they have relatively good pore-throat spaces (Figs. 11 and 12). Moreover, the development of dissolved pores and microfractures during the diagenetic evolution process (Fig. 21) provides favorable conditions for the injection of organic acids and natural gas into other lithofacies (Guo et al., 2024; Shi et al., 2017).

The correlation coefficients of the mean D_{TL} and mean LF of Gm with the mean Por_Core, Perm_Core, and Swi_Core of Stc and Spc are high (Fig. 26(g)), and they are positively correlated with the mean Por_Core and Perm_Core of the architectural elements and other sandstone lithofacies with a relatively low coefficient (Fig. 26(a), (g)), and negatively correlated with the mean Swi_Core of the architectural elements and other sandstone lithofacies with a relatively low coefficient (Fig. 26(a), (g)). This indicates that the development of Gm significantly contributes to the improvement of the reservoir quality of Stc and Spc, but contributes insufficiently to the improvement of the reservoir quality of the architectural elements and other lithofacies. The reason is that both the constructive diagenesis (dissolved pores formed by dissolution) and destructive diagenesis (carbonate mineral cementation) of Gm are well-developed (Figs. 16–20), and the diagenetic facies are mostly DFdm and DFcc. During the diagenetic evolution process, the dissolved pores of Gm are developed (Fig. 21), providing relatively favorable conditions for the injection of organic acids and natural gas into the adjacent Stc and Spc, but contributing less

to the lithofacies at a relatively long distance (Guo et al., 2024; Xie et al., 2021). In addition, due to its physical properties and fluid mobility being worse than those of Stc and Spc (Figs. 13–15), its contribution to the improvement of the overall reservoir quality of the architectural elements is not as good as that of Stc and Spc.

The mean D_{TL} and mean LF of Sp are positively correlated with the mean Por_Core, Perm_Core, and Swi_Core of the architectural elements with a relatively low coefficient (Fig. 26(a), (d)), but the correlation coefficient with Swi_Core is relatively high. The reason is that the reservoir quality of Sp is relatively poor (Figs. 13–15), and the irreducible water content is relatively high (Fig. 15). The high irreducible water content will increase the irreducible water saturation of the overall architectural elements, but the poor physical properties of the reservoir contribute very limitedly to the improvement of the overall physical properties of the architectural elements. The mean D_{TL} and mean *LF* of Sp are positively correlated with the mean Por_Core and Perm_Core of various sandstone lithofacies with a relatively low coefficient, and negatively correlated with the mean Swi_Core of various sandstone lithofacies with a relatively low coefficient (Fig. 26(a) and (d)), which indicates that the development of Sp can promote the improvement of the reservoir quality of other lithofacies to a certain extent. The reason is that both the constructive diagenesis (intercrystalline pores of clay mineral cement) and destructive diagenesis (clay mineral cementation) of Sp are well-developed (Figs. 16–20). During the diagenetic evolution process, Sp serves as the main site for the precipitation of diagenetic ions and the cementation of clay minerals after being displaced by natural gas. The diagenetic facies are mainly DFcmc, supplemented by DFcmip. The high content of clay minerals means that organic acids and natural gas flow well and are enriched in other lithofacies.

The mean D_{TL} and mean LF of Sr are positively correlated with the mean Por_Core of the architectural elements with a low coefficient, negatively correlated with the mean Perm_Core with a low coefficient, and positively correlated with the mean Swi_Core with a high coefficient (Fig. 26(a)). This indicates that the development of Sr is beneficial for improving the porosity of the reservoirs of the architectural elements, but is not conducive to the improvement of the permeability of the reservoirs of the architectural elements, and significantly limits the fluid mobility of the architectural elements. The reason is that the reservoir quality of Sr is relatively poor (Figs. 13–15), and the content of irreducible water is high (Fig. 15), and excessive development will reduce the overall reservoir quality of the architectural elements. In addition, the mean D_{TL} and mean LF of Sr are negatively correlated with the mean Por_Core and Perm_Core of various sandstone lithofacies with a low coefficient (Fig. 26(c)), and positively correlated with the mean Swi_Core of various sandstone lithofacies with a low coefficient (Fig. 26(c)), which indicates that the development of Sr is also not conducive to the improvement of the reservoir quality of other lithofacies. The reason is that the physical properties of the reservoirs of Sr are poor. The diagenetic facies are mainly DFcc and DFcmc, supplemented by DFc. Destructive diagenesis (carbonate mineral cementation, clay mineral cementation, and compaction) is well-developed (Figs. 16–20). Dissolved pores and

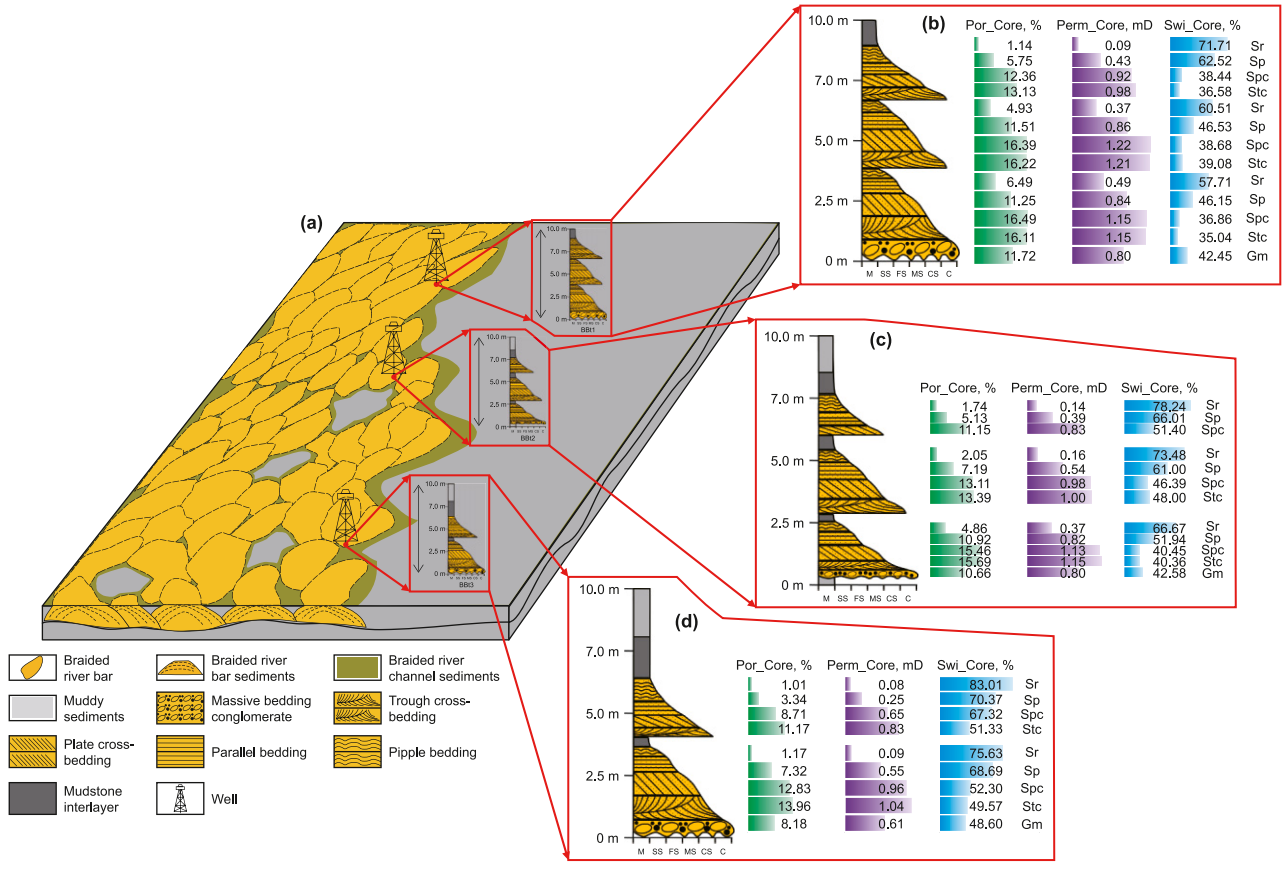

Fig. 27. The sedimentary pattern of braided river and the distribution pattern of the heterogeneous reservoir quality of architectural elements. **(a)** The sedimentary pattern of braided river. **(b)** The distribution pattern of the heterogeneous reservoir quality of BBt1. **(c)** The distribution pattern of the heterogeneous reservoir quality of BBt2. **(d)** The distribution pattern of the heterogeneous reservoir quality of BBt3.

microfractures are poorly developed during the diagenetic evolution process (Fig. 21), and it mostly develops into physical property interlayers, which play a shielding role in the injection of organic acids and natural gas (Shang et al., 2019; Xie et al., 2024). Therefore, its development is not conducive to the improvement of the reservoir quality of other lithofacies.

The mean D_{TL} and mean LF of Mm are negatively correlated with the mean Por_Core and Perm_Core of the architectural elements and various sandstone lithofacies with a high coefficient, and positively correlated with the mean Swi_Core of the architectural elements and various sandstone lithofacies with a high coefficient (Fig. 26(a) and (b)). This indicates that the development of Mm is extremely unfavorable for the improvement of the reservoir quality of the architectural elements and other sandstone lithofacies. The reason is that Mm is a lithologic interlayer, which has an extremely strong shielding effect on the injection of organic acids and natural gas into other sandstone lithofacies, thus hindering the development of constructive diagenesis of the overall architectural elements and other sandstone lithofacies. Moreover, the diagenetic fluid in the adjacent lithofacies is likely to be enriched, leading to the well-developed destructive diagenesis ("vermicular", sheet-like and fibrous clay mineral cementation). In addition, the pure mudstone with a certain thickness also transports CO_3^{2-} to the adjacent sandstone lithofacies, resulting in the well-developed destructive diagenesis (carbonate mineral cementation) of the adjacent sandstone lithofacies (Abbasi et al., 2022; DeReuil and Birgenheier, 2019; Li et al., 2023).

In conclusion, sedimentary heterogeneity not only affects whether the overall architectural elements can become high-quality reservoirs, but also controls whether the internal lithofacies can develop into high-quality reservoirs. When the sedimentary heterogeneity of the architectural elements is weak, the total lithofacies density and lithofacies frequency of the sandstone lithofacies (such as Stc, Spc, Gm and Sp) are high (Table 8), which is beneficial for the improvement of the reservoir quality of the architectural elements, and also promotes the improvement of the reservoir quality of the internal lithofacies. Conversely, when the sedimentary heterogeneity is strong, the total lithofacies density and lithofacies frequency of the silty-muddy sediments (such as Sr and Mm) are high (Table 8), which is not conducive to the improvement of the reservoir quality of the architectural elements, and is also not conducive to the improvement of the reservoir quality of the internal lithofacies.

5.3.3. *The heterogeneous distribution pattern of the reservoir quality of the architectural elements*

Based on the control of sedimentary and diagenetic heterogeneities on reservoir quality, and combined with the diagenetic heterogeneities of the sandbody architectures of braided river and meandering river, this study further establishes the distribution patterns of heterogeneous reservoir quality of different architectural elements.

a. The heterogeneous distribution pattern of the reservoir quality of the architectural elements of the braided river

Under the control of the dissolved pores formed by dissolution and the microfractures formed by fracturing on the reservoir porosity and permeability (Fig. 25(a), (e)), and restricted by the development patterns of the dissolved pores formed by dissolution and the microfractures formed by fracturing in the heterogeneous diagenetic patterns of BBt1, BBt2 and BBt3, the Por_Core and Perm_Core exhibit a positive rhythm pattern of gradual decrease with the decrease of the lithofacies grain size (Fig. 27(b)–(d)) (except for Gm, as its reservoir physical properties are slightly lower than those of Stc). Under the control of the intercrystalline pores of clay mineral cement and the clay mineral cementation on the irreducible water saturation of the reservoir

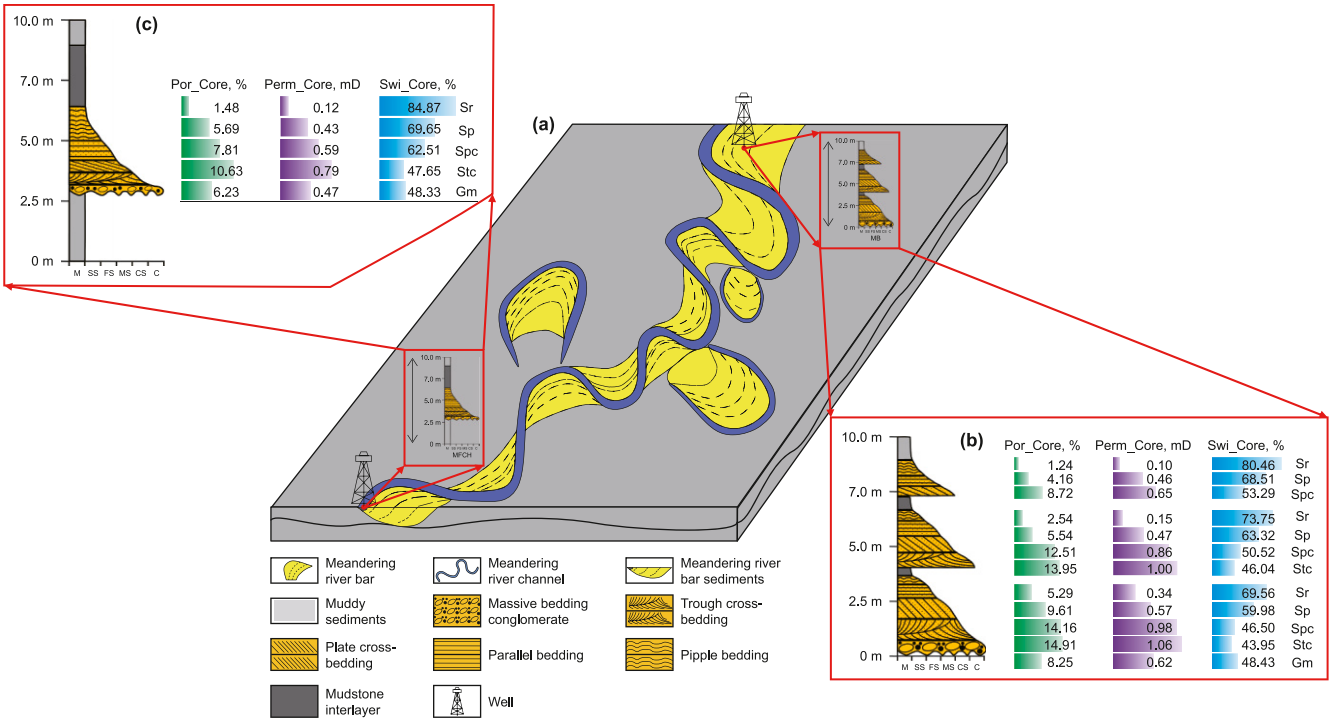

Fig. 28. The sedimentary pattern of meandering river and the distribution pattern of the heterogeneous reservoir quality of architectural elements. **(a)** The sedimentary pattern of meandering river. **(b)** The distribution pattern of the heterogeneous reservoir quality of MB. **(c)** The distribution pattern of the heterogeneous reservoir quality of MFCH.

(Fig. 25(h) and (i)), and restricted by the development patterns of the intercrystalline pores of clay mineral cement and the clay mineral cementation in the heterogeneous diagenetic patterns of BBt1, BBt2 and BBt3, the irreducible water saturation of the reservoir (Swi_Core) exhibits a reverse rhythm pattern of gradual increase with the decrease of the lithofacies grain size (Fig. 27(b)–(d)).

b. The heterogeneous distribution pattern of the reservoir quality of the architectural elements of the meandering river

The heterogeneous distribution of the reservoir quality of the architectural elements of the meandering river is quite similar to that of the braided river. Under the control of the dissolved pores formed by dissolution and the microfractures formed by fracturing on the reservoir porosity and permeability (Fig. 25(a), (e)), and restricted by the development patterns of diagenesis such as the dissolved pores formed by dissolution, the microfractures formed by fracturing, the intercrystalline pores of clay mineral cement, and the clay mineral cementation in the heterogeneous diagenetic patterns of MB and MFCH, the Por_Core and Perm_Core exhibit a positive rhythm pattern (Fig. 28(b) and (c)) (except for Gm, as its reservoir physical properties are slightly lower than those of Stc); the irreducible water saturation of the reservoir (Swi_Core) exhibits a reverse rhythm pattern (Fig. 28(b) and (c)). Slightly differently, under the control of the development of pure mudstone interlayers within the architectural elements and the development of thick mudstone at the top and bottom, stronger carbonate mineral cementation makes the lithofacies near the pure mudstone interlayers in MB have relatively poorer reservoir quality, making MFCH show the worst reservoir quality as a whole.

6. Conclusion

This study established the heterogeneous diagenetic patterns of sandbody architectural elements (constrained by sedimentary heterogeneity) in the Shanxi Formation of the northern Sulige Gas Field, clarified their origins, and revealed the distribution of heterogeneous reservoir quality. Conclusions are as follows.

(1) The Shanxi Formation in the study area mainly develops six lithofacies (Gm, Stc, Spc, Sp, Sr, and Mm), three braided river sandbody architectural elements (BBt1, BBt2, and BBt3), and two meandering river sandbody architectural elements (MB and MFCH). Among them, BBt1 exhibits weak and sand-dominated sedimentary heterogeneity; BBt2 and MB show moderate sedimentary heterogeneity; BBt3 has strong sedimentary heterogeneity; and MFCH displays weak and mud-dominated sedimentary heterogeneity.

(2) The Shanxi Formation in the study area mainly undergoes five diagenetic types: compaction, fracturing, cementation, dissolution, and metasomatism. Based on diagenetic evolution sequence, present-day reservoir characteristics, relative intensities of diagenetic processes and their impacts on reservoirs, five diagenetic facies are identified: strong compaction (DFc), strong dissolution + microfracture development (DFdm), clay mineral intercrystalline pore-dominated (DFcmip), strong carbonate cementation (DFcc), and strong clay mineral cementation (DFcmc). Under sedimentary heterogeneity control, sandbody architectural elements in the Shanxi Formation show heterogeneous diagenetic patterns. DFc primarily occurs in siltstone lithofacies of sand-dominated, weakly sedimentary heterogeneous architectural elements; DFdm is mainly in coarser-grained sandstones of sand-dominated architectural elements with low sedimentary heterogeneity; DFcmip is primarily located near interbeds within all architectural elements; DFcc predominates in thick mudstones at the top/bottom of architectural elements, and at contacts with pure mudstone interbeds; DFcmc concentrates in medium-heterogeneity architectural elements near pure mudstone interbeds and at contacts with silty mudstone interbeds.

(3) Under sedimentary and diagenetic heterogeneity control, architectural elements' reservoir quality also shows heterogeneous distribution. Among them, porosity (Por_Core) and permeability (Perm_Core) exhibit a positive rhythmic gradual decrease as lithofacies grain size reduces—except Gm, with physical properties slightly lower than Stc. Irreducible water saturation (Swi_Core) shows a reverse rhythmic gradual increase as grain size decreases.

In summary, exploring the coupling of sedimentary, diagenetic, and reservoir quality heterogeneities in fluvial tight sandstone reservoirs holds theoretical and practical value for understanding reservoir quality heterogeneity distributions and guiding exploration-development strategies, while this study's findings on diagenetic fluid and gas migration—shaped by lithofacies and interlayer spatial distributions within sandbody architecture—provide insights for fluid flow laws and numerical simulation of such reservoirs. Last but not least, factors controlling sedimentation and diagenesis—such as fluvial provenance systems, tectonic evolution, and paleoenvironmental climate—vary across different basins. In future research, collecting extensive relevant data from other basins and conducting studies based on the methods and frameworks of this research will help obtain more accurate, comprehensive, and generalizable conclusions.

CRediT authorship contribution statement

Pan-Ke Sun: Writing – review & editing, Writing – original draft, Validation, Methodology, Conceptualization. **Shi-Yi Jiang:** Writing – review & editing, Writing – original draft, Supervision, Methodology, Conceptualization. **Rui-Feng Yan:** Validation, Supervision, Resources, Investigation, Data curation. **Li Liu:** Visualization, Supervision, Investigation, Formal analysis. **Gang Tian:** Visualization, Validation, Supervision, Investigation. **Zeng Sheng:** Software, Investigation, Data curation. **Bin Li:** Validation, Investigation, Conceptualization. **Rui-Feng Zhou:** Methodology, Investigation. **Si-Cheng Zhu:** Methodology, Investigation. **Lin Zhang:** Resources, Project administration, Funding acquisition, Data curation.

Conflict of interest

All authors disclosed no relevant relationships.

Acknowledgement

This research is supported by the National Natural Science Foundation of China (No. 42572150). The authors are grateful to the staffs from Western Drilling Engineering Co., Ltd., CNPC, for their kind assistance in the collection of core samples and other data. We also appreciate Professor Zhe-Jun Pan from Northeast Petroleum University for his valuable guidance during the manuscript revision, as well as the editors and reviewers for their insightful comments on revising and improving the manuscript, which have greatly enhanced the quality of the paper.

References

Abbasi, I.A., Özcan, E., El-Ghali, M.A.K., Hersi, O.-S., Al Harthy, A., Ali, A., 2022. Mixed deltaic and carbonate deposition in a tectonically restricted basin: An example from the lower and middle members of the Eocene Musawa Formation, Abat Basin, south-eastern Oman Mountains. Geol. J. 57 (10), 4242–4261. https://doi.org/10.1002/gj.4542.

Ahmadi, Y., Mehrabi, H., Hasani, M., Ranjbaran, M., 2025. Depositional and diagenetic heterogeneities in sequence stratigraphic framework of a mixed carbonate-siliciclastic reservoir: A case study from Oligocene–Miocene Asmari Formation in the Persian Gulf. J. Asian Earth Sci. 277, 106392. https://doi.org/10.1016/j.jseaes.2024.106392.

Alameen, M.B., Elraies, K.A., Mohyaldinn, M., Almansour, A., Gmail, A.M., Hagar, H., 2024. Reducing the sand production from semi-consolidated sandstone formation by mitigating the Silica dissolution factor during water breakthrough. International Petroleum Technology Conference. https://doi.org/10.2523/IPTC-23402-EA.

Antonellini, M., Del Sole, L., Mollema, P.N., 2025. Effects of outcrop-scale structural and diagenetic heterogeneities on flow and mass transport in a porous sandstone aquifer. Mar. Petrol. Geol. 177, 107406. https://doi.org/10.1016/j.marpetgeo.2025.107406.

Beard, D.C., Weyl, P.K., 1973. Influence of texture on porosity and permeability of unconsolidated sand. AAPG Bull. 57 (2), 349–369. https://doi.org/10.1306/819A4272-16C5-11D7-8645000102C1865D.

Bello, A.M., Usman, M.B., Amao, A.O., Al-Ramadan, K., Al-Hashem, M., Kachalla, A., Abubakar, U., Salisu, A.M., Mukkafa, S., Kwami, I.A., Aro, O.E., Butt, M.N., Maigari, A.S., Yusuf, A., Chiroma, L.U., Akinsanpe, O.T., 2024. Diagenesis and reservoir quality evolution of estuarine sandstones: Insights from the Cenomanian-Turonian Yolde formation, northern Benue trough, NE Nigeria. Mar. Petrol. Geol. 169, 107073. https://doi.org/10.1016/j.marpetgeo.2024.107073.

Burger, K., Zhou, Y.P., Ren, Y.L., 2002. Petrography and geochemistry of tonsteins from the 4th member of the Upper Triassic Xujiahe Formation in southern Sichuan Province, China. Int. J. Coal Geol. 49 (1), 1–17. https://doi.org/10.1016/S0166-5162(01)00053-2. Article Pii s0166-5162(01)00053-2.

Busch, B., Böcker, J., Hilgers, C., 2024. Improved reservoir quality assessment by evaluating illite grain coatings, quartz cementation, and compaction – case study from the Buntsandstein, Upper Rhine Graben, Germany. Geoenergy Sci. Eng. 241, 213141. https://doi.org/10.1016/j.geoen.2024.213141.

Colombera, L., Mountney, N.P., 2019. The lithofacies organization of fluvial channel deposits: A meta-analysis of modern rivers. Sediment. Geol. 383, 16–40. https://doi.org/10.1016/j.sedgeo.2019.01.011.

DeReuil, A.A., Birgenheier, L.P., 2019. Sediment dispersal and organic carbon preservation in a dynamic mudstone-dominated system, Juana Lopez member, Mancos Shale. Sedimentology 66 (3), 1002–1041. https://doi.org/10.1111/sed.12532.

El-Gendy, N.H., Radwan, A.E., Waziry, M.A., Dodd, T.J.H., Kh Barakat, M., 2022. An integrated sedimentological, rock typing, image logs, and artificial neural networks analysis for reservoir quality assessment of the heterogeneous fluvial-deltaic Messinian Abu Madi reservoirs, Salma field, onshore East Nile Delta, Egypt. Mar. Petrol. Geol. 145, 105910. https://doi.org/10.1016/j.marpetgeo.2022.105910.

Fallah-Bagtash, R., Bayet-Goll, A., Omidpour, A., Kakemem, U., 2025. Reservoir quality drivers in the Oligo-Miocene Asmari Formation, Dezful Embayment, Iran: Facies, diagenesis, and tectonic controls. Mar. Petrol. Geol. 173, 107279. https://doi.org/10.1016/j.marpetgeo.2024.107279.

Folk, R.L., Ward, W.C., 1957. Brazos River bar [Texas]; a study in the significance of grain size parameters. J. Sediment. Res. 27 (1), 3–26. https://doi.org/10.1306/74D70646-2B21-11D7-8648000102C1865D.

Guo, H., Xia, W., Shan, X., Xi, K., Peng, B., Yang, X., Zou, Z., Yuan, W., 2024. Diagenetic genesis and evolution of coal-bearing tight sandstone reservoir in the Yangxia Formation, Northern kuqa Depression, Tarim Basin. ACS Omega 9 (16), 18314–18326. https://doi.org/10.1021/acsomega.3c10100.

Hagar, H.S., Forooezsh, J., Zivar, D., Kumar, S., Abdulelah, H., Dzulkarnain, I.B., 2020. Simulation of hydrogen sulfide generation. In: Oil and Gas Geological Formations 2020 International Conference on Computational Intelligence (ICCI), Bandar Seri Iskandar, Malaysia.

Hagar, H.S., Foroozesh, J., Kumar, S., Zivar, D., Banan, N., Dzulkarnain, I., 2022. Microbial H_2S generation in hydrocarbon reservoirs: Analysis of mechanisms and recent remediation technologies. J. Nat. Gas Sci. Eng. 106, 104729. https://doi.org/10.1016/j.jngse.2022.104729.

Haile, B.G., Hellevang, H., Aagaard, P., Jahren, J., 2015. Experimental nucleation and growth of smectite and chlorite coatings on clean feldspar and quartz grain surfaces. Mar. Petrol. Geol. 68, 664–674. https://doi.org/10.1016/j.marpetgeo.2015.02.006.

He, W.W., Hajash, A., Sparks, D., 2002. A model for porosity evolution during creep compaction of sandstones. Earth Planet Sci. Lett. 197 (3–4), 237–244. https://doi.org/10.1016/S0012-821X(02)00490-9.

Heidsiek, M., Butscher, C., Blum, P., Fischer, C., 2020. Small-scale diagenetic facies heterogeneity controls porosity and permeability pattern in reservoir sandstones. Environ. Earth Sci. 79 (18), 425. https://doi.org/10.1007/s12665-020-09168-z.

Henares, S., Caracciolo, L., Viseras, C., Fernández, J., Yeste, L.M., 2016. Diagenetic constraints on heterogeneous reservoir quality assessment: A Triassic outcrop analog of meandering fluvial reservoirs. AAPG Bull. 100 (9), 1377–1398. https://doi.org/10.1306/04011615103.

Janssen, M., Caracciolo, L., Bonnell, L.M., Lander, R.H., Munnecke, A., Beltran-Trivino, A., Muto, F., Stollhofen, H., 2023. Climatic, depositional and environmental controls on early carbonate cementation in fluvial and shallow marine sandstones. Mar. Petrol. Geol. 156. https://doi.org/10.1016/j.marpetgeo.2023.106433. Article 106433.

Jiang, F., Jia, C., Pang, X., Jiang, L., Zhang, C., Ma, X., Qi, Z., Chen, J., Pang, H., Hu, T., Chen, D., 2023. Upper Paleozoic total petroleum system and geological model of natural gas enrichment in Ordos Basin, NW China. Petrol. Explor. Dev. 50 (2), 281–292. https://doi.org/10.1016/S1876-3804(23)60387-8.

Jiang, S., Sun, P., Lyu, F., Zhu, S., Zhou, R., Li, B., He, T., Lin, Y., Gao, Y., Song, W., Xu, H., 2024. Machine learning (ML) for fluvial lithofacies identification from well logs: A hybrid classification model integrating lithofacies characteristics, logging data distributions, and ML models applicability. Geoenergy Sci. Eng. 233, 212587. https://doi.org/10.1016/j.geoen.2023.212587.

Jiu, B., Huang, W.H., Li, Y., He, M.Q., 2021. Influence of clay minerals and cementation on pore throat of tight sandstone gas reservoir in the eastern Ordos Basin, China. J. Nat. Gas Sci. Eng. 87, 103762. https://doi.org/10.1016/j.jngse.2020.103762.

Kadkhodaie-Ilkhchi, R., Kadkhodaie, A., Rezaee, R., Mehdipour, V., 2019. Unraveling the reservoir heterogeneity of the tight gas sandstones using the porosity conditioned facies modeling in the Whicher Range field, Perth Basin, Western Australia. J. Petrol. Sci. Eng. 176, 97–115. https://doi.org/10.1016/j.petrol.2019.01.020.

Leila, M., El-Khoriby, E., Ahmed, M.A., Saied, O., El Adl, H., 2024. Depositional facies controls on reservoir rock typing and heterogeneity: Devonian siliciclastic succession, south central Ghadames Basin, Libya. Mar. Petrol. Geol. 163, 106770. https://doi.org/10.1016/j.marpetgeo.2024.106770.

Leila, M., Moscariello, A., Segvic, B., 2019. Depositional facies controls on the diagenesis and reservoir quality of the Messinian Qawasim and Abu Madi formations, onshore Nile Delta, Egypt. Geol. J. 54 (3), 1797–1813. https://doi.org/10.1002/gj.3269.

Li, H., Zhu, H., Du, X., Yang, X., 2023. Secondary porosity generation in sandstones constrained by the fault movement, fluid flow, and mudstone–sandstone interactions, offshore Bohai Bay Basin, China. AAPG Bull. 107 (5), 785–821. https://doi.org/10.1306/09232220024.

Li, M., Guo, Y.H., Wang, H.C., Li, Z.F., Hu, Y.B., 2020. Effects of mineral composition on the fracture propagation of tight sandstones in the Zizhou area, east Ordos Basin, China. J. Nat. Gas Sci. Eng. 78, 103334. https://doi.org/10.1016/j.jngse.2020.103334.

Li, Y., Fan, A., Yang, R., Sun, Y., Lenhardt, N., 2021. Sedimentary facies control on sandstone reservoir properties: A case study from the permian Shanxi Formation in the southern Ordos Basin, central China. Mar. Petrol. Geol. 129, 105083. https://doi.org/10.1016/j.marpetgeo.2021.105083.

Li, Y., Yang, J.H., Pan, Z.J., Meng, S.Z., Wang, K., Niu, X.L., 2019. Unconventional natural gas accumulations in stacked deposits: A discussion of upper Paleozoic coal-bearing strata in the East Margin of the ordos Basin, China. Acta Geologica Sinica - English Edition 93 (1), 111–129. https://doi.org/10.1111/1755-6724.13767.

Mahgoub, M.I., Abdullatif, O.M., 2020. Facies, petrography, reservoir heterogeneity and quality of the late Carboniferous-Permian Juwayl Member, Wajid Sandstone, SW Saudi Arabia. Mar. Petrol. Geol. 120, 104521. https://doi.org/10.1016/j.marpetgeo.2020.104521.

Marghani, M.M.A., Zairi, M., Radwan, A.E., 2023. Facies analysis, diagenesis, and petrophysical controls on the reservoir quality of the low porosity fluvial sandstone of the Nubian formation, east Sirt Basin, Libya: Insights into the role of fractures in fluid migration, fluid flow, and enhancing the permeability of low porous reservoirs. Mar. Petrol. Geol. 147, 105986. https://doi.org/10.1016/j.marpetgeo.2022.105986.

Meng, W., Sui, F., Zhang, T., Hao, X., Yuan, W., Jiang, Y., Zhang, S., Ma, L., Qin, F., Xiong, W., Tianxia, 2023. Thermodynamic mechanism and its geological significance in the transformation of albite under inorganic acid environments based on the total dissolution model. Geoenergy Sci. Eng. 221, 111295. https://doi.org/10.1016/j.petrol.2022.111295.

Miall, A.D., 1985. Architectural-element analysis: a new method of facies analysis applied to fluvial deposits. Earth Sci. Rev. 22 (4), 261–308. https://doi.org/10.1016/0012-8252(85)90001-7.

Molenaar, N., Felder, M., 2018. Clay cutans and the origin of illite RIM cement: an example from the siliciclastic ROTLIEGEND sandstone in the Dutch southern PERMIAN basin. J. Sediment. Res. 88 (5), 641–658. https://doi.org/10.2110/jsr.2018.33.

Morad, S., Al-Ramadan, K., Ketzer, J.M., De Ros, L.F., 2010. The impact of diagenesis on the heterogeneity of sandstone reservoirs: A review of the role of depositional facies and sequence stratigraphy. AAPG Bull. 94 (8), 1267–1309. https://doi.org/10.1306/04211009178.

Moraes, M.A.S.S.Z., 1991. Multiscale diagenetic heterogeneity and its influence on reservoir properties of fluvial, deltaic and turbiditic sandstone reservoirs, potiguar and Recôncavo Rift Basins. University of Wyoming, Brazil. Dissertation/Thesis.

Ocheli, A., Omoko, E.N., Aigbadon, G.O., Ogbe, O.B., 2025. Grain size distributions and petrographic analyses of the outcropped Eocene-Miocene sedimentary successions, southern Nigeria: Depositional environments and petroleum reservoir quality predictions. Results in Earth Sciences 3, 100068. https://doi.org/10.1016/j.rines.2025.100068.

Ortiz-Orduz, A., Ríos-Reyes, C.A., Vargas-Escudero, M.A., García-González, M., 2021. Impact of diagenesis on the reservoir rock quality of the Cachiri group tight sandstones in Cesar sub basin (Colombia): A case of study from ANH-CR-MONTECARLO 1X well. J. Nat. Gas Sci. Eng. 95, 104138. https://doi.org/10.1016/j.jngse.2021.104138.

Patrick, L., Monthioux, M., Meunier, J.-D., 1984. Importance of the oxidation/maturation pair in the evolution of humic coals. Org. Geochem. 7 (3), 249–260. https://doi.org/10.1016/0146-6380(84)90121-9.

Qin, S., Wang, R., Shi, W., Liu, K., Zhang, W., Xu, X., Qi, R., Yi, Z., 2022. Diverse effects of intragranular fractures on reservoir properties, diagenesis, and gas migration: insight from Permian tight sandstone in the Hangjinqi area, north Ordos Basin. Mar. Petrol. Geol. 137, 105526. https://doi.org/10.1016/j.marpetgeo.2022.105526.

Qin, Y., Liu, C., Huang, L., Wang, J., Zhao, J., Shao, D., Yang, L., Zhao, X., Khalaf, E., Zhang, S., Du, N., 2024. Characteristics of the low-pressure spatial and temporal distributions of oil- and gas-bearing layers in the Ordos Basin, China. Int. J. Coal Geol. 285, 104476. https://doi.org/10.1016/j.coal.2024.104476.

Rubinstein, N., Fazio, A.M., Scasso, R.A., Carey, S., 2013. Association of phosphate with rhyolite glass in marine Neogene tuffs from Patagonia, Argentina. Sedimentology 60 (4), 1007–1016. https://doi.org/10.1111/sed.12005.

Sahoo, H., Gani, M.R., Hampson, G.J., Gani, N.D., Ranson, A., 2016. Facies- to sandbody-scale heterogeneity in a tight-gas fluvial reservoir analog: Blackhawk formation, Wasatch Plateau, Utah, USA. Mar. Petrol. Geol. 78, 48–69. https://doi.org/10.1016/j.marpetgeo.2016.02.005.

Scherer, M., 1987. Parameters influencing porosity in sandstones: a model for sandstone porosity prediction. AAPG Bull. 71 (5), 485–491. https://doi.org/10.1306/94886ED9-1704-11D7-8645000102C1865D.

Shang, X., Duan, T., Hou, J., Li, Y., 2019. Spatial configuration of sand and mud in the lacustrine nearshore sand bar deposits and its geological implications. Petrol. Explor. Dev. 46 (5), 954–968. https://doi.org/10.1016/S1876-3804(19)60252-1.

Shao, X.H., Pang, X.Q., Jiang, F.J., Li, L.L., Huyan, Y.Y., Zheng, D.Y., 2019. Diagenetic characteristics and reservoir quality in tight gas sandstones: A case study of the Shanxi formation in the north-eastern Ordos Basin, China. Geol. J. 54 (6), 3257–3271. https://doi.org/10.1002/gj.3326.

Shi, H., Luo, X.R., Lei, G.L., Zhang, L.Q., Zhang, L.K., Lei, Y.H., 2017. Diagenesis and fluid flow variability of structural heterogeneity units in tight sandstone carrier beds of dibei, Eastern kuqa Depression. Geofluids 2017 (1), 6593913. https://doi.org/10.1155/2017/6593913.

Shi, Y., Liu, Z., Wang, S., Wu, J., Liu, X., Hu, Y., Chen, S., Feng, G., Wang, B., Wang, H., 2024. Genetic mechanism and main controlling factors of high-quality clastic rock reservoirs in deep and ultradeep layers: A case study of Oligocene Linhe Formation in Linhe Depression, Hetao Basin, NW China. Petrol. Explor. Dev. 51 (3), 548–562. https://doi.org/10.1016/S1876-3804(24)60487-8.

Su, N.N., Song, F., Qiu, L.W., Zhang, W., 2021. Diagenetic evolution and densification mechanism of the Upper Paleozoic tight sandstones in the Ordos Basin, Northern China. J. Asian Earth Sci. 205, 104613. https://doi.org/10.1016/j.jseaes.2020.104613.

Sun, F.Y., Cao, G.S., Xing, Z., Yu, S.J., Fang, B.B., 2021. Characteristics and evaluation of the Upper Paleozoic source rocks in the Southern North China Basin. Open Geosci. 13 (1), 294–309. https://doi.org/10.1515/geo-2020-0221.

Sun, P.K., Jiang, S.Y., Zhang, L., Jia, L.B., Rao, H.W., Fang, H.J., Yi, Z., He, T.H., Zhu, S.C., Bao, L.Y., 2022. Impacts of sedimentation and diagenesis on deeply buried reservoir quality of a rift Basin: A case study of Wenchang Formation in the Lufeng Depression, Pearl River mouth Basin, China. Geofluids 2022, 8625005. https://doi.org/10.1155/2022/8625005.

Wang, J., Jiang, F., Hu, Q., Zhang, C., Yang, X., Mo, W., Wang, X., Qi, Z., 2023. A quantitative model and controlling factors of secondary pore development for tight sandstone reservoirs in the carboniferous Benxi Formation, Ordos Basin, China. Mar. Petrol. Geol. 148, 106034. https://doi.org/10.1016/j.marpetgeo.2022.106034.

Wang, X., Zeng, J., Liu, B., Zhao, W., Shi, K., Jia, K., 2025. Insights into the wetting mechanisms in low-permeability sandstone reservoirs and its evolution processes: The Shahejie Formation in the Dongying Depression, Bohai Bay Basin. Mar. Petrol. Geol. 171, 107179. https://doi.org/10.1016/j.marpetgeo.2024.107179.

Weber, J., Ricken, W., 2005. Quartz cementation and related sedimentary architecture of the Triassic Solling Formation, Reinhardswald Basin, Germany. Sediment. Geol. 175 (1), 459–477. https://doi.org/10.1016/j.sedgeo.2004.12.019.

Wendao, Q., Taiju, Y., Changmin, Z., Guowei, H., Miao, H., Min, X., Xiujin, Y., Lan, Y., 2019. Geology prediction techniques for reservoir Evolution simulation. Geotectonics 53 (3), 399–418. https://doi.org/10.1134/S0016852119030099.

Xie, H., Zhou, D., Shi, H., Kong, D., Li, Y., Li, F., Cao, J., 2021. Lithospheric stretching-style variations and anomalous post-rift subsidence in the deep water sub-basins of the Pearl River Mouth Basin, northern South China Sea. Mar. Petrol. Geol. 131, 105140. https://doi.org/10.1016/j.marpetgeo.2021.105140.

Xie, J., Hou, B., He, M., Liu, X., Wei, J., 2024. Fracture-controlled fracturing mechanism and penetration discrimination criteria for thin sand-mud interbedded reservoirs in Sulige gas field, Ordos Basin, China. Petrol. Explor. Dev. 51 (5), 1327–1339. https://doi.org/10.1016/S1876-3804(25)60544-1.

Yang, R., Fan, A., Han, Z., Wang, X., 2012. Diagenesis and porosity evolution of sandstone reservoirs in the East II part of Sulige gas field, Ordos Basin. Int. J. Min. Sci. Technol. 22 (3), 311–316. https://doi.org/10.1016/j.ijmst.2012.04.005.

Yu, Z.C., Wang, Z.Z., Adenutsi, C.D., 2023. Genesis of authigenic clay minerals and their impacts on reservoir quality in tight conglomerate reservoirs of the Triassic Baikouquan formation in the Mahu Sag, Junggar Basin, Western China. Mar. Petrol. Geol. 148, 106041. https://doi.org/10.1016/j.marpetgeo.2022.106041.

Zhang, L.C., Jiang, S., Xiao, D.S., Lu, S.F., Zhang, R., Chen, G.H., Qin, Y.L., Sun, Y.H., 2020. Controls on pore structures and permeability of tight gas reservoirs in the Xujiaweizi Rift, Northern Songliao Basin. Energies 13 (19), 5184. https://doi.org/10.3390/en13195184.

Zhang, T., Wu, J.J., Fei, H.Y., 2019. Characteristics and controlling factors of the Lower-Middle Jurassic sandstone reservoirs in Amu Darya right bank area, Turkmenistan. Arabian J. Geosci. 12 (9), 293. https://doi.org/10.1007/s12517-019-4387-z.

Zhang, Y., Tian, J.C., Zhang, X., Li, J., Liang, Q.S., Zheng, X.Y., 2022. Diagenesis evolution and pore types in tight sandstone of Shanxi Formation Reservoir in Hangjinqi area, ordos Basin, Northern China. Energies 15 (2), 470. https://doi.org/10.3390/en15020470.

Zhou, Q.S., Li, C., Chen, G.J., Lyu, C.F., Qu, X.F., Ma, X.F., Li, C.Z., Lei, Q.H., Xie, Q.C., 2021. The formation mechanism of authigenic chlorite in tight sandstone and its effect on tight oil adsorption during hydrocarbon filling. Oil & Gas Science and Technology - Revue d'IFP Energies nouvelles 76, 39. https://doi.org/10.2516/ogst/2021015.

Zhu, Y.H., Zhao, Z.G., Li, X., Liu, C., Yu, S.S., Lu, Y.Y., Du, X.J., 2024. Influence of feldspar dissolution on the pore structure and characteristics of a tight sandstone reservoir: A case study from the Northeast Margin of Ordos Basin, China. Geofluids 2024, 9069384. https://doi.org/10.1155/2024/9069384.

Zhu, Y.L., Vieth-Hillebrand, A., Wilke, F.D.H., Horsfield, B., 2015. Characterization of water-soluble organic compounds released from black shales and coals. Int. J. Coal Geol. 150, 265–275. https://doi.org/10.1016/j.coal.2015.09.009.